

2018-01-01

Design And Experimental Study Of A High Pressure And Supercritical Methane-Oxygen Burner

A S M Arifur Rahim Chowdhury
University of Texas at El Paso, chowdhuryarifur@gmail.com

Follow this and additional works at: https://digitalcommons.utep.edu/open_etd



Part of the [Mechanical Engineering Commons](#)

Recommended Citation

Chowdhury, A S M Arifur Rahim, "Design And Experimental Study Of A High Pressure And Supercritical Methane-Oxygen Burner" (2018). *Open Access Theses & Dissertations*. 1410.
https://digitalcommons.utep.edu/open_etd/1410

This is brought to you for free and open access by DigitalCommons@UTEP. It has been accepted for inclusion in Open Access Theses & Dissertations by an authorized administrator of DigitalCommons@UTEP. For more information, please contact lweber@utep.edu.

DESIGN AND EXPERIMENTAL STUDY OF A HIGH PRESSURE AND SUPERCRITICAL METHANE-OXYGEN BURNER

A S M ARIFUR RAHIM CHOWDHURY

Doctoral Program in Mechanical Engineering

APPROVED:

Norman D. Love, Ph.D., Chair

Ahsan Choudhuri, Ph.D., Co- Chair

Evgeny Shafirovich, Ph.D.

Jose L. Banuelos, Ph.D.

Charles Ambler, Ph.D.
Dean of the Graduate School

Copyright ©

by

A S M Arifur Rahim Chowdhury

2018

Dedication

I would like to dedicate to my mother who inspired me at every aspect of my life. I would like to dedicate to my beloved wife who was with me throughout the whole journey. I would like to dedicate to my elder brother for paving the path. I would like to dedicate to my all family members: Sadia, Rafat, Samia and Rahat. I would like to dedicate to Imran, Shovon, Shauki for all the joyous moments and Shaown Vaia, Taifur Mama and Shemme Apu for being good influence. I would like to dedicate to Al-Amin, Abid, Amir and Khalamoni. Finally, I would like to dedicate to my father who taught me how to be a good person above all.

I would like to extend my deepest appreciation to Dr. Norman Love for his mentorship and advice; and Dr. Ahsan Choudhuri for his guidance throughout my academic career.

I would not be here without any of you.

Nanu: I got it

DESIGN AND EXPERIMENTAL STUDY OF A HIGH PRESSURE AND
SUPERCRITICAL METHANE-OXYGEN BURNER

by

A S M ARIFUR RAHIM CHOWDHURY, BSME, MSME

DISSERTATION

Presented to the Faculty of the Graduate School of

The University of Texas at El Paso

in Partial Fulfillment

of the Requirements

for the Degree of

DOCTOR OF PHILOSOPHY

Department of Mechanical Engineering

THE UNIVERSITY OF TEXAS AT EL PASO

May 2018

Acknowledgements

I would like to acknowledge the support of the NASA MIRO Center for Space Exploration and Technology Research. This research is supported by the US Department of Energy, under award DoE Award Number: DE-FE-0029113 (Program Manager: Parrish Galusky) and Air Liquide. However, any opinions, findings, conclusions, or recommendations expressed herein are those of the authors and do not necessarily reflect the view of the Department of Energy and Air Liquide.

Abstract

Directly heated supercritical oxy-fuel power cycles have potential to offer a higher thermal efficiency and lower pollutant emissions compared to existing power cycles. Recent thermodynamic analysis of the cycle performed by several groups including the UTEP-Air Liquide research team show that combustion in the vicinity of 300 bar pressure and 1000-1400 K temperature allows for relatively high system efficiencies while operating within the limit of practical combustor materials. However, the realization of directly heated supercritical power cycle requires combustion systems be designed to operate in supercritical conditions and at temperature far below the blowout limit of conventional flames (above 1500 K), where not only the thermodynamic properties but also the combustion properties and kinetics are unexplored. To minimize these knowledge gaps, some intermediate pressure ranges (up to 20 bar) are experimented and modeled using a CFD simulation tool. The knowledge obtained from the high pressure test will assist in understanding the combustion chamber pressurization mechanism, ignition and flame behavior at the elevated pressure. This is a systematic first step in testing at higher pressures of 100 and 300 bar pressures.

The primary objective of this dissertation is to perform qualitative analysis on oxy-methane combustion at high pressure (< 20 bar) and compare to CFD model for future scale up to supercritical condition. For modeling of the system, a commercial computational fluid dynamics simulation tool, ANSYS Fluent, is used. The inlet conditions for the CFD analysis are obtained from the experiments. The geometry used for the study is same as the test apparatus and operates at the same power ratings. The expertise gained from this experimental study is important to accurately and safely design combustors at elevated pressures up to 300bar. A high pressure methane-oxygen fuel burner and combustor have been developed to accommodate oxy-combustion environment. A detailed CFD analysis is conducted to understand the flame length and cooling phenomenon inside the combustor first at pressures up to 20 bar to compare to experiments then at supercritical pressure. The first part of the dissertation compares CFD results

with high pressure burner experiments at pressures up to 20 bar. The test is conducted for 30 s within 150 kW – 250 kW thermal power inputs. Afterwards, based on the simulation results a cooling system is proposed for steady state high pressure combustion experiments. It is observed from the experimental study that the proposed pressurization mechanism able to pressurize the vessel up to 20 bar. It is also determined that the current combustor can operate up to 20 bar for short term. The steady state CFD simulation demonstrates that a cooling system must be incorporated for continuous operation. Additionally, the study focuses on the ignition delay due to added diluent during the combustion process. It is observed that as the carbon dioxide recirculation ratio increases the ignition delay time increases. Later part of the dissertation provides a preliminary guideline for developing a laboratory scale supercritical oxy combustor. The employment of supercritical fluid in gas turbine is fairly a new concept. Hence, there are many questions that need to be answered. During this dissertation study an investigation is performed to understand the impact of equation of state in the supercritical combustion simulation. Finally, a CFD model for developing supercritical oxy-methane burner and the combustor, incorporating real gas model, is presented. Although Lee-Kesler equation of state provides better accuracy than Peng Robinson, due to the computational time Peng Robinson equation of state is used for the simulation. It is found that existing knowledge is not enough to simulate combustion at supercritical phase. Detailed combustion chemistry at the supercritical condition must be developed and should be incorporated to accurately replicate the combustion phenomenon.

Table of Contents

Acknowledgements.....	v
Abstract.....	vi
Table of Contents.....	viii
List of Tables	x
List of Figures	xi
Chapter 1: Introduction and Background.....	1
1.1 High Pressure Combustion (< 20 bar)	2
1.1.1 Experiments	2
1.1.2 Computational modeling studies.....	6
1.2 Supercritical Combustion.....	11
1.2.1 Indirectly heated supercritical power cycle	11
1.2.2 Directly heated supercritical power cycle.....	12
1.3 Project Objective.....	15
1.4 Practical Relevance	16
1.5 Commercial Potential.....	18
Chapter 2: Design Methodology.....	20
2.1 Burner Design Methodology.....	20
2.2 Igniter Design Methodology	23
2.3 End Cap Design Methodology.....	25
2.4 Combustor Cooling System Design.....	26
2.5 Combustor Parts Dimensions.....	27
2.6 Numerical Investigation Methodology	33
2.6.1 Burner CFD Analysis.....	34
Chapter 3: Experimental Methodology.....	39
3.1 Feed System	39
3.2 Data Acquisition and Control System.....	46
3.3 The Combustor Test Bed	50
Chapter 4: Results and Discussion.....	52
4.1 Experimental Results	52

4.2	CFD Analysis.....	61
4.3	Combustor Cooling System	79
Chapter 5: Supercritical Combustor Development		87
5.1	Cycle Analysis	87
5.2	Comparison of Equation of States for Supercritical Fluid Analysis.....	91
5.3	CFD Analysis.....	96
Chapter 6: Summary and Future Work.....		102
References.....		106
Appendix.....		110
Vita		152

List of Tables

Table 1 Summary of CFD strategies [10]	8
Table 2 Main burner maximum operating condition	21
Table 3 Igniter operating condition.....	24
Table 4 Cross- sectional area inlet and exit port.....	34
Table 5 CFD boundary conditions (High pressure test replication)	37
Table 6 Part type and data collection rate.....	41
Table 7 Feed system parts specifications.....	44
Table 8 Gas tank regulators specifications	45
Table 9 LabView back panel connection interfaces (a) flowmeter, (b) pressure interface, (c) thermocouple and (d) solenoid valve.....	48
Table 10 Test cases	53
Table 11 Fluent input parameters at the inlets	63
Table 12 Fluent input parameters at the wall.....	64
Table 13 Fluent input parameters at the outlet.....	64
Table 14 Exit area and exit diameter estimation from analytical solution	65
Table 15 Carbon dioxide mass flowrates for different cases	86
Table 16 Power consumption distribution for different CO ₂ recirculation configurations when combined with a liquid methane and oxygen feed system	89
Table 17 Power production for the two different CO ₂ recirculation configurations assuming a liquid methane and oxygen delivery system.....	89
Table 18 Constants for the BWR-Lee-Kesler equation	93
Table 19 Boundary condition (Supercritical combustion simulation).....	97
Table 20 Critical properties of fluids	99
Table 20 Boundary condition (Preliminary CFD analysis-High pressure test)	110
Table 21 Boundary Conditions (Comparison of EOS).....	137
Table 22 Inlet flowrates	138

List of Figures

Figure 1 (a) High pressure test rig configuration, (b) Stream wise profiles of the computed wall temperatures (solid lines) and mean gas temperatures (dashed lines) [4].	3
Figure 2 Schematic of the duel chamber apparatus, holes are aligned (right) [5].	4
Figure 3 (a) Experimental apparatus for OH and CH simultaneous emission imaging, (b) Schematic representation of cryogenic flames, (A) subcritical oxygen, gaseous methane, (B) Transcritical oxygen, gaseous methane, (C) Transcritical oxygen, transcritical methane [6].	5
Figure 4 (a) cutaway view of the high-pressure chamber at UTIAS, University of Toronto: (1) Optical access ports; (2) Quartz windows; (3) Burner assembly (4) Chimney assembly; (5) Upper flange housing the exhaust, safety valves, and pressure transducer; (6) Lo Lower flange housing air, fuel pipes and wiring; (7) Combustion chamber, (b) A schematic of the high-pressure combustion experimental layout [7]	6
Figure 5 Simulation of flow past circular cylinder, $Re = 50,000$ [10]	8
Figure 6 (a) Heat flux predictions from respective calculations compared with corresponding experimental data. (b) Expense increment [10]	9
Figure 7 Indirectly heated supercritical power cycle	12
Figure 8 Directly heated supercritical power cycle	13
Figure 9 (a) Cross section of test combustor, (b) 30MPa combustion test system, (c) Test article installed on test stand, and (d) Test stand at time of ignition	14
Figure 10 (a) Time trend of pressure and exit temperature, (b) Time trend of mass flow.	15
Figure 11 US Energy consumption scenario [24]	17
Figure 12 Main burner	22
Figure 13 Main burner recess length	23
Figure 14 Igniter	24
Figure 15 1/4-32 spark plug	25
Figure 16 Combustor end cap	26
Figure 17 CO ₂ cooling manifold	27
Figure 18 Combustor (exploded view)	28
Figure 19 Combustor front cap (a) front cap body, (b) diluent inlet plate and (c) perforated plate	30
Figure 20 Combustor body	30
Figure 21 Combustor metal window cover (a) metal window and (b) window attachment plate	31
Figure 22 Combustor end cap (a) part 1, (b) part 2 and (c) part 3	33
Figure 23 Combustor in 2D domain	34
Figure 24 Mesh (High pressure test replication)	35
Figure 25 Piping and Instrumentation diagram	41
Figure 26 (a) Valve train on the trailer (b) Valve train close to the main burner gas tank facility and (c) test setup	46
Figure 27 DAQ and control system	47
Figure 28 LabView Interface	47
Figure 29 Combustor test bed	51
Figure 30 Pressure profile with respect to time-case 1	54
Figure 31 Main burner ignition-case 1	55
Figure 32 Flame images at different time frame during the test- case 1	56
Figure 33 Volumetric flowrates with respect to time- case 1	57

Figure 34 Exhaust gas composition at equilibrium condition- case 1	57
Figure 35 Pressure profile with respect to time - (a) case 2, (b) case 3	59
Figure 36 Volumetric flowrates with respect to time - (a) case 2, (b) case 3	61
Figure 37 Exit diameter vs. chamber pressure comparison between the analytical solution and CFD estimation	66
Figure 38 CFD results for case 1 (a) Mach number at the exit, (b) velocity number at the exit, (c) pressure contour inside the combustor and (d) temperature contour inside the combustor.....	71
Figure 39 CFD results for case 2 (a) Mach number at the exit, (b) velocity number at the exit, (c) pressure contour inside the combustor and (d) temperature contour inside the combustor.....	74
Figure 40 CFD results for case 3 (a) Mach number at the exit, (b) velocity number at the exit, (c) pressure contour inside the combustor and (d) temperature contour inside the combustor.....	77
Figure 41 Temperature profile near the wall ($R = 0.138$ m).....	78
Figure 42 Schematic of a pressure vessel and the direction of all the stresses in front and side view.....	79
Figure 43 Young's Modulus of SS410 for a range of temperatures	81
Figure 44 Total stress and Yield Strength vs the temperature	81
Figure 45 Effect of CO ₂ recirculation ratios on adiabatic flame temperature (a) case 1, (b) case 2 and (c) case 3	84
Figure 46 Effect of CO ₂ recirculation ratios on ignition (a) case 1, (b) case 2 and (c) case 3.....	85
Figure 47 CO ₂ cooling system manifold.....	86
Figure 48 ASPEN HYSYS® layout of the liquid feed methane and oxygen feed system supercritical combustor, (a) showing liquid CO ₂ recirculation, (b) showing gaseous CO ₂ recirculation	90
Figure 49 Thermodynamic properties availability (NIST database)	92
Figure 50 Mesh (Supercritical combustion simulation).....	97
Figure 51 Temperature with respect to axial distance: (a) 100 bar case and (b) 300 bar case	100
Figure 52 Compressibility factor with respect to axial distance: (a) 100 bar case and (b) 300 bar case.....	101
Figure 53 Density and velocity profile at the inlet of the combustor	113
Figure 54 Pressure inside the combustor	114
Figure 55 Temperature profile inside the combustor.....	115
Figure 56 Exit velocity.....	116
Figure 57 Methane mass fraction.....	116
Figure 58 Carbon dioxide mass fraction.....	117
Figure 59 Streamline inside the combustor	118
Figure 60 (a) Proposed oxy-methane supercritical combustor, (b) One-eighth of the proposed combustor.....	141
Figure 61 (a) CFD simulation fluid domain, (b) Inlet of the combustion chamber, (c) Cross-section view of the fluid domain, (d) Detailed view of the inlet cross-section	142
Figure 62 Mesh (Fluid domain)	143
Figure 63 Density distribution at the inlet of the combustion chamber (a) Ideal gas, (b) Peng Robinson, (c) Lee Kesler	144
Figure 64 Compressibility factor at the inlet of the combustor (a) Peng Robinson EOS (b) Lee Kesler EOS.....	145
Figure 65 Temperature distribution inside the combustor (a) Ideal gas, (b) Peng Robinson, and (c) Lee Kesler.....	146

Figure 66 Flow path at the inlet of the combustor (a) 50%-50% split, (b) 30%-70% split, and (c) 10%-90% split.....	147
--	-----

Chapter 1: Introduction and Background

Oxy-combustion is a combustion technique that facilitates capturing as high as 100% carbon dioxide at the post combustion stage. Oxy-combustion also could increase the system efficiency due to the higher temperatures produced when burning with oxygen instead of air. Additionally, the employment supercritical (up to 300 bar) combustion can reduce the system foot print and the operational costs, compared to conventional power systems [1,2]. Motivated by the advantages of supercritical phase oxy-combustion, the purpose of this dissertation is to develop a high pressure (up to 20 bar) methane-oxygen burner and combustor for steady operation. The knowledge obtained from this study will be used to a supercritical oxy-combustor.

The dissertation is divided into two sections. In the first section, a design approach is presented explaining the steps for fabricating a methane-oxygen burner and the modifications made to an existing combustor for < 20 bar steady state combustion testing. A thorough literature study is conducted to understand the existing high pressure combustor designs and the operating parameters. A shear-coaxial burner is designed using methane as the fuel and pure oxygen as the oxidizer. The burner designed during this study could also be used in pulverized coal combustor as the ignition source. Sarker et al. [3] developed an optically accessible high-pressure combustor which is originally designed for performing high pressure air-fuel combustion. The same combustor is used for this study. However, oxy combustion flame temperatures may reach up to 3500 K. Therefore, numerous modifications are made to fit the high temperature and high pressure oxy-combustion environment. The high pressure, < 20 bar, combustion experiments are conducted to test the burner operability, thermal and pressure endurance of the combustor, chamber pressurization technique and carbon dioxide cooling method.

In the second section, the experimental work presented in part 1 is extended to a model for a supercritical (100 bar and 300 bar) oxy-methane burner and combustor design. At first a cycle analysis is presented to demonstrate the superiority of supercritical gas turbine over existing gas turbines. Afterwards, a CFD analysis is conducted at 100 bar and 300 bar incorporating real gas

model. This part of the dissertation provides a preliminary guideline for developing a laboratory scale supercritical oxy combustor.

1.1 High Pressure Combustion (< 20 bar)

In last several decades high pressure combustion applications have been investigated extensively. The research works have been concentrated mostly towards characterizing combustion parameters and fluid behavior in a high pressure environment [1-9]. In last decade, many studies have been successfully conducted experimenting on high pressure/trans-critical combustion accommodating air-methane, oxy-methane and LOx-H₂ in different pressure environments [3-9]. Furthermore, many CFD tools have developed to analyze the combustion phenomenon at high temperature [10-17]. Usually, there are three different types of numerical solving methods that are used for simulating combustion: (i) Reynolds-Averaged Navier-Stokes (RANS), (ii) Large Eddy Simulations (LES), and (iii) Direct Numerical Simulations (DNS) [10]. Even though LES and DNS have better computational accuracy in terms of scale of space and time over RANS, due to computational simplicity, RANS is widely practiced [10]. In this section, a thorough literature review is conducted to understand the experimental methodologies and the progression of numerical solving methods.

1.1.1 Experiments

Carroni et al. [4] conducted high pressure experiments and have modeled air-methane catalytic combustion for power generation applications. While testing, the authors used parameters that can be found in many operating gas turbines. The tests in the study are conducted up to a 15 bar (1.5 MPa) pressure with a maximum thermal input of 300 kW. The experimental setup is shown in Figure 1(a). The experiment is conducted in a sub-scale test-rig, which comprises a metallic honeycomb structure with coated channels. The setup consists of four different parts (Air Preheaters, Fuel Injection, Mixing Section, Combustor module) along with an optical access section. Three 30 kW electric heaters are used to preheat air up to the desired temperature of 650 °C. The authors claim that a 30 cm long series of static mixtures ensures air and fuel mixing. In

order to achieve near adiabatic environment, the test section and burnout section are insulated with the ceramic insulation. Furthermore, the system pressure and velocity are regulated via a throttle to ensure that the flow is always choked. This arrangement facilitates simplifying the relationship between velocity, pressure and mass flow. The Reynolds number is kept within 1100 to 3800 during the experiment. Part of this study investigates the wall temperature of the combustor at the high pressure, which can be seen in Figure 1(b). Figure 1(b) shows that the wall temperature is the maximum at the highest pressure (15 bar), almost 1100 K, while the adiabatic flame temperature can be reached up to 1600 K. The dependency of pressure, channel length and hydraulic diameter on catalytic activity is also calculated during the experiment. .

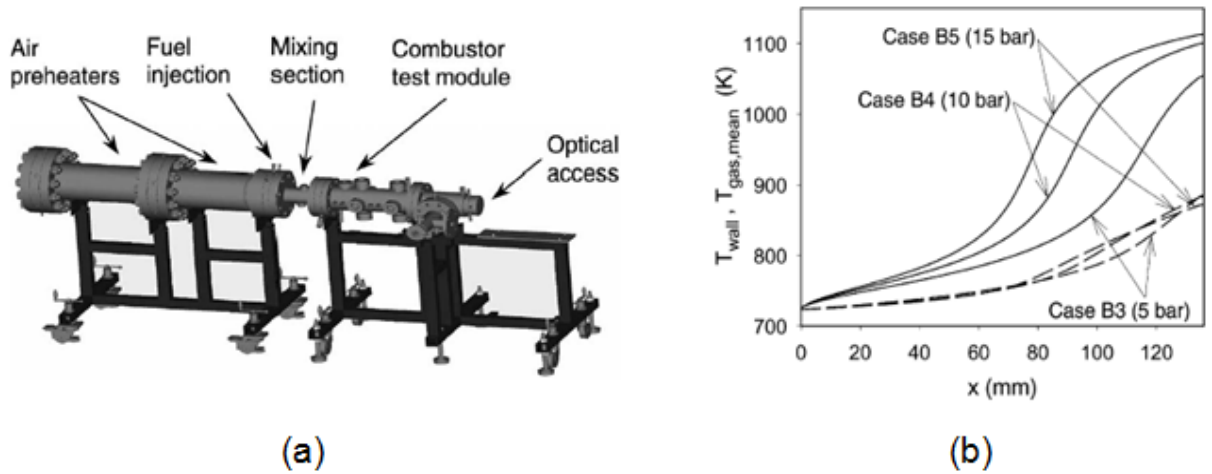


Figure 1 (a) High pressure test rig configuration, (b) Stream wise profiles of the computed wall temperatures (solid lines) and mean gas temperatures (dashed lines) [4].

Tse et al. [5] designed and built an optically accessible high-pressure combustion apparatus to observe the morphology and development of premixed reaction fronts at elevated pressure. The authors followed a chamber-in-chamber design approach to manufacture the combustor for constant pressure combustion experiments, Figure 2. The study has been conducted using methane, hydrogen and nitrogen flames. The experimental apparatus is suited for the study of laminar premixed flames, flame instabilities, turbulent flames, and detonations up to a 60 bar pressure. The

experimental data can be used for the development of comprehensive oxidation reaction mechanisms for air-fuel combustion flame at such high pressure. During the experiment, the inner vessel is initially filled with the combustible pre-mixer and the outer chamber is filled with an inert gas at a similar pressure. The quartz window is mounted at the start and end case of both combustors. A check valve is located in the system to prevent the chamber from over pressurizing. The volume ratio of the outer to inner vessel is about 25:1, thus the total pressure increase in the entire system due to combustion within the inner vessel is small, measured to be less than 3%. The ignition energy is delivered by a spark at the center of the inner vessel via electrodes extending from opposite locations of the lateral surface. The Schlieren/Shadowgraph technique is used to analyze the flame. A 70 bar, pressure transducer with a 0.1s response time is embedded inside the combustion chamber which reads the absolute pressure inside the chamber during the combustion process. To ensure the reliability of the apparatus, the stretched corrected laminar burning velocities as a function of equivalence ratio for hydrogen-air mixture at standard temperature and pressure are calculated and compared with the numerical simulation. The authors found that the flame speed given in literature matches well within the experimental uncertainties and are repeatable.

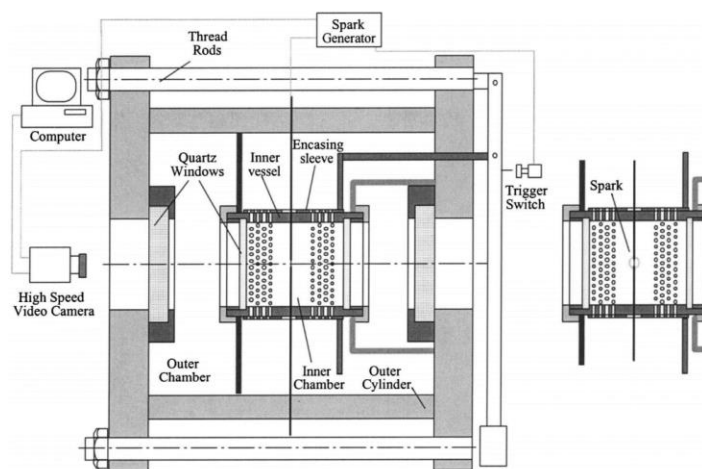


Figure 2 Schematic of the duel chamber apparatus, holes are aligned (right) [5].

Singla et al. [6] have studied the transcritical oxygen/transcritical or supercritical methane combustion. For the most part, in liquid propellant engines the reactants are injected at subcritical temperature into an environment in which the temperature and pressure exceed the thermodynamic critical conditions. In this experimental study, a similar concept has been used to conduct high pressure oxy-fuel combustion testing. The combustion chamber pressure has been kept between 4.5 to 6 MPa (45 bar to 60 bar) while the reactants are initially in a subcritical stage. Three different cases are investigated during this experimental study. In the first case both of the propellants are injected in a transcritical phase, the second and third case being such that the either one of the propellant (oxygen) are in subcritical/transcritical stage while the other one (methane) is at supercritical stage. The combustor is designed to have cross section of $50 \times 50 \text{ mm}^2$ with 75 mm long optical windows on its four sides. A converging-diverging nozzle is utilized to control the pressure inside the combustion chamber. The heat input is determined to be 0.55 MW for the investigation. The authors have investigated the flame structure, CH and OH emission at different operating points. Figure 3 (b) shows the flame structure at different operating conditions: (A) Subcritical oxygen, gaseous methane, (B) Transcritical oxygen, gaseous methane, (C) Transcritical oxygen, transcritical methane. The authors have found that during transcritical methane-oxygen injection the flame stabilizes in the near field region.

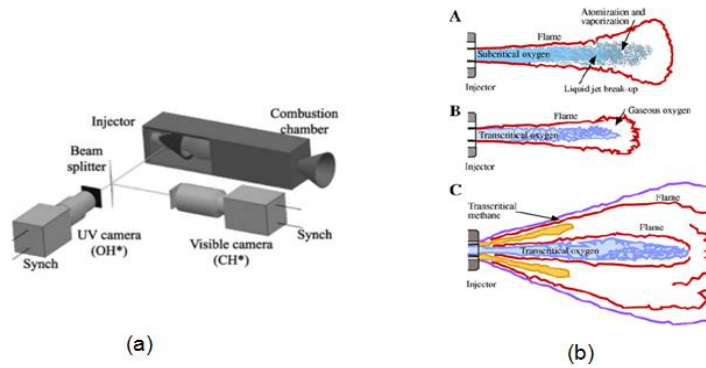


Figure 3 (a) Experimental apparatus for OH and CH simultaneous emission imaging, (b) Schematic representation of cryogenic flames, (A) subcritical oxygen, gaseous methane, (B) Transcritical oxygen, gaseous methane, (C) Transcritical oxygen, transcritical methane [6]

The combustor that is shown in Figure 4 (a) is developed by the University of Toronto, and the National Research Council of Canada collaboratively [7]. The combustor was initially designed to analyze the soot formation at elevated pressure. The injector has height of 0.6 m and the internal diameter of 0.24 m with the maximum operating pressure of 11 MPa (110 bar). The combustor accommodates several optical access points that facilitate analysis of the flame. The detailed schematic can be seen in Figure 4(b). The experimental results provide an extensive database that can be compared quantitatively to analyze the effect of pressure on soot formation for various fuels.

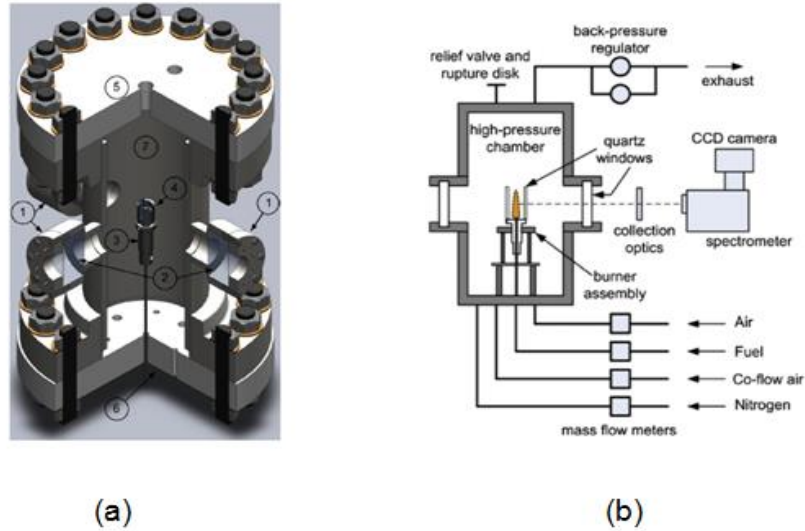


Figure 4 (a) cutaway view of the high-pressure chamber at UTIAS, University of Toronto: (1) Optical access ports; (2) Quartz windows; (3) Burner assembly (4) Chimney assembly; (5) Upper flange housing the exhaust, safety valves, and pressure transducer; (6) Lower flange housing air, fuel pipes and wiring; (7) Combustion chamber, (b) A schematic of the high-pressure combustion experimental layout [7]

1.1.2 Computational modeling studies

In this section a comparison among different numerical solution methods which can be useful for combustor design are presented. It is found from the literature that, due to the reasonable

computational cost and less computational time Reynolds-Averaged Navier-Stokes (RANS) is widely used over Large Eddy Simulations (LES), and and Direct Numerical Simulations (DNS) [10]. Spalart [10], Edge et al. [11], Ladeinde et al. [12], Zong et al. [13] and Sierra-Pallares et al. [14] have performed a comprehensive study on different numerical solving methods for analyzing fluid dynamics problems, supercritical/transcritical fluid injection characteristics and combustion.

Spalart [10] reviewed and discussed the strategies for turbulence modeling and simulations. The study compares the solution methods to those that are commonly employed in solving fluid dynamics problems: RANS, DNS, and LES. It is mentioned that, in recent times, intermediate solution methods such as ‘VLES (Very Large Eddy Simulation)’, ‘URANS (Unsteady Reynolds Average Navier Stokes)’, and ‘DES (Detached Eddy Simulation)’ are also being practiced, even though they are still under investigation. The study shows that the turbulence predictions in aerodynamics include two primary challenges which can be summarized as: (i) growth and separation of boundary layer and (ii) momentum transfer after separation. Although LES involves significant cost, this method addresses both of the challenges compared to the RANS method. A comparison between steady RANS, Unsteady RANS, LES (Coarse grid), and LES (fine grid) can be seen in Figure 5. The simulation was conducted at $Re=50,000$. The contour shows that LES method captures eddy formation downstream of the cylinder. It also varies between the grid types. However, the RANS technique is unable to simulate the eddy formation scenario after the cylinder. On the other hand, due to significant cost and computational time the DNS method is often ignored. A summary of solution methods, Reynolds number dependency, empiricism, and readiness level is shown in Table 1. It is shown that RANS and LES have weak dependency on Re , whereas the DNS approach has strong Re dependency. Moreover, in terms of empiricism, RANS and DES have strong empiricism over LES and DNS. With these being taken into account, Spalart [10] summarizes that despite the computational superiority of LES and DNS, due to computational simplicity and moderate solving time RANS solution method is widely used to simulate fluid dynamics problems.

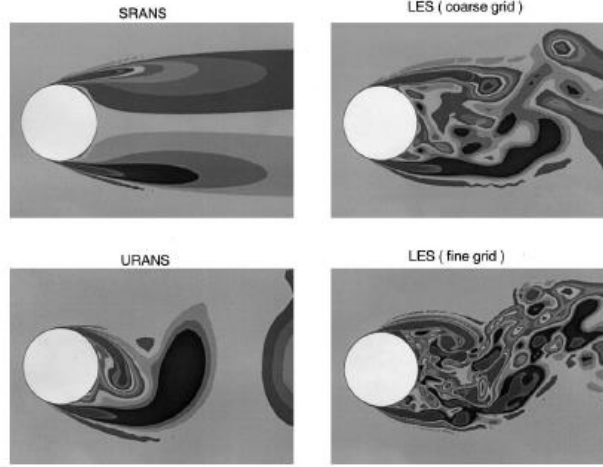


Figure 5 Simulation of flow past circular cylinder, $Re = 50,000$ [10]

Table 1 Summary of CFD strategies [10]

Name	Aim	Unsteady	Re-Dependency	3/2D	Empiricism	Grid	Steps	Ready
2D-URANS	Numerical	Yes	Weak	No	Strong	10^5	$10^{3.5}$	1980
3D-RANS	Numerical	No	Weak	No	Strong	10^7	10^3	1990
3D-URANS	Numerical	Yes	Weak	No	Strong	10^7	$10^{3.5}$	1995
DES	Hybrid	Yes	Weak	Yes	Strong	10^8	10^4	2000
LES	Hybrid	Yes	Weak	Yes	Weak	$10^{11.5}$	$10^{6.7}$	2045
QDNS	Physical	Yes	Strong	Yes	Weak	10^{15}	$10^{7.3}$	2070
DNS	Numerical	Yes	Strong	Yes	None	10^{16}	$10^{7.7}$	2080

Edge et al. [11] have compared LES with RANS models while analyzing air-coal and oxy-coal combustion. The authors have found that the LES can offer improvements over RANS in predicting recirculation zones and flame properties of the pulverized combustion. Veynante et al. [15] found that LES is a very powerful tool in predicting reacting flow fields even in complex geometries such as gas turbines. However, the authors explain that LES requires describing small scale effects and this approach is computationally expensive. Ladeinde et al. [12] performed a critical review of scramjet combustion simulations. The authors have found that the RANS approach dictates the turbulence modeling of the system, with only a few of LES model. Ladeinde et al. [12] have also stated that almost all the numerical procedures are based on low-order schemes, and the combustion models that have been used for realistic simulations solve the species

evolution equations with assumed PDF closures, even though there seems to be a growing use of the flamelet methods.

Rocket engines have the legacy of operating at high pressure conditions. A group of researchers from NASA Marshall Space Center, Georgia Technology University, Purdue University, Sandia National Laboratory, and The Pennsylvania State University have conducted a study on validating high-fidelity CFD simulations for rocket injector designs [17]. The main purpose of the study is to compare and understand the predictive capabilities and computational requirements of a range of CFD methodologies on a set of single element LOx/H₂ injector model problems. The injector is designed to operate at a 50 bar pressure. The study is performed utilizing five different solution approaches from LES and RANS methods. It is found that the LES approach demonstrates the best match with the experimental wall heat flux data, Figure 6(a). However, it is also observed that, the convergence of the data doesn't improve with the computational tool fidelity increment. The authors organized the solution

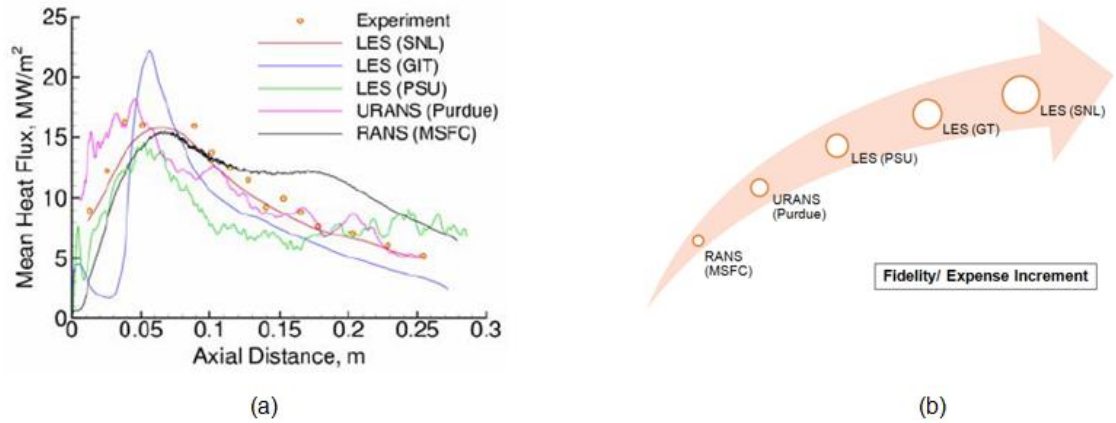


Figure 6 (a) Heat flux predictions from respective calculations compared with corresponding experimental data. (b) Expense increment [10]

approaches from the high fidelity/expense to low fidelity/expense as LES (SNL), LES (GIT), LES (PSU), URANS (Purdue), and RANS (MSFC), Figure 6(b). The ultimate goal for this study was to select an appropriate simulation fidelity level for injector design based on transparent comparison of demonstrated computational performance in terms of accuracy and cost. The

authors have concluded that the selection of solution approach highly depends on the expected accuracy and calculation time. Zong et al. [13] numerically studied the cryogenic fluid injection and mixing under supercritical conditions. The authors have investigated the dynamics of a nitrogen fluid jet over a broad range of ambient pressures. The Large-Eddy Simulation technique is adapted to model the turbulence of the flow. It is explored that a string of strong density-gradient regimes are developed surrounding the jet, which exerts a stabilizing effect on the flow development. Also, the spatial growth rate of the surface instability wave increases as the pressure increases. The study shows that the jet dynamics are mostly dictated by the local thermodynamic state through its influence on the fluid thermophysical properties. Sierra-Pallares et al. [14] performed a numerical study of supercritical and transcritical injection using different turbulent Prandtl numbers. The maximum operating pressure for this analysis is set to be 60 bar. The authors use the RANS approach to analyze the supercritical/transcritical fluid injection phenomenon. It is already known that the flow and mixing of fluids under transcritical/supercritical conditions are largely dependent on the fundamentals of conservation equations for mass, momentum, species and energy. The authors suggest that, to deal with turbulent flow a suitable averaging method must be used. For this particular study, the density averaging technique is used. The $k-\epsilon$ model is applied to simulate the turbulence of the flow. Supercritical fluid follows real gas law. Therefore, a proper equation of state must be implemented to approximate the parameters at supercritical region. Sierra-Pallares et al. [14] used the REFPROP library which is integrated with the ANSYS. This library determines the thermodynamic properties based on multi parameter equation of state that represents nearly all selected experimental data within their estimated accuracy within the exception of heat capacities and speed of sound close to the critical points. It is mentioned in the paper that the typical accuracies for density, vapor pressure and heat capacities are 0.05%, 0.02%, and 0.05%, respectively. The study reveals that the constant Prandtl number at 0.5 predicts better the flow structure in comparison with the experimental data.

1.2 Supercritical Combustion

The employment of supercritical working fluids for power generation is becoming popular as it promises more efficient power production compared to existing systems. This technique assumes that the working fluids are operated above their critical points, where significant density is observed for a fluid with near gaseous physical properties. Due to large density change at the turbine stage, these types of systems have the potential to deliver higher net work in a smaller space compared to conventional working fluid driven systems. The supercritical fluid can be employed in two different methods for extracting power: (i) indirectly Heated, and (ii) Directly Heated.

1.2.1 Indirectly heated supercritical power cycle

In an indirectly heated cycle, the working fluids do not come in direct contact with the heat source. The configuration of an indirectly heated supercritical power cycle is shown in Figure 7. A hot fluid leaves the primary heat source, such as a nuclear reactor or concentrated solar panel, passes through a heat exchanger and heats up the working fluid until it reaches a supercritical state. Once it reaches supercritical phase, the working fluid then flows through a turbine and generates power. In an indirectly heated system, supercritical pressures need to be reached for the working fluid. For CO₂ this value is approximately 74 bar. So far the application of supercritical carbon dioxide in indirectly heated cycles and the economic impact in power generation has been widely studied. This kind of system has high potential of recovering low-grade waste heat due to the better glide matching between heat source and working fluid in the heat recovery vapor generator [18]. Although not the focus of this dissertation, it is useful to consider the applications of the indirectly heated power cycle since much more literature is available on this topic. Ohji [19] found that the implementation of supercritical CO₂ in the steam turbine reduces carbon dioxide pollutant emission by 10% and operational costs by 20% compared to existing systems. The authors also show that the thermal efficiency of the steam turbine is improved by 14% when the existing oil-fired unit is replaced with the ultra-supercritical CO₂ unit. Ma et al. [20] presents the use of

supercritical CO₂ in a concentrated solar power plant (CSP). The authors find that the implementation of a recompression supercritical CO₂ Brayton cycle in the CSP has potential to achieve equivalent or higher thermal efficiencies than the supercritical or superheated steam turbine. Oh et al. [21] conducted an analysis on improving efficiency of the very high temperature nuclear reactor (VHTR) incorporating supercritical CO₂ in the power cycle. The research team developed a supercritical CO₂ Brayton cycle for the indirectly heated supercritical CO₂ power cycle [21].

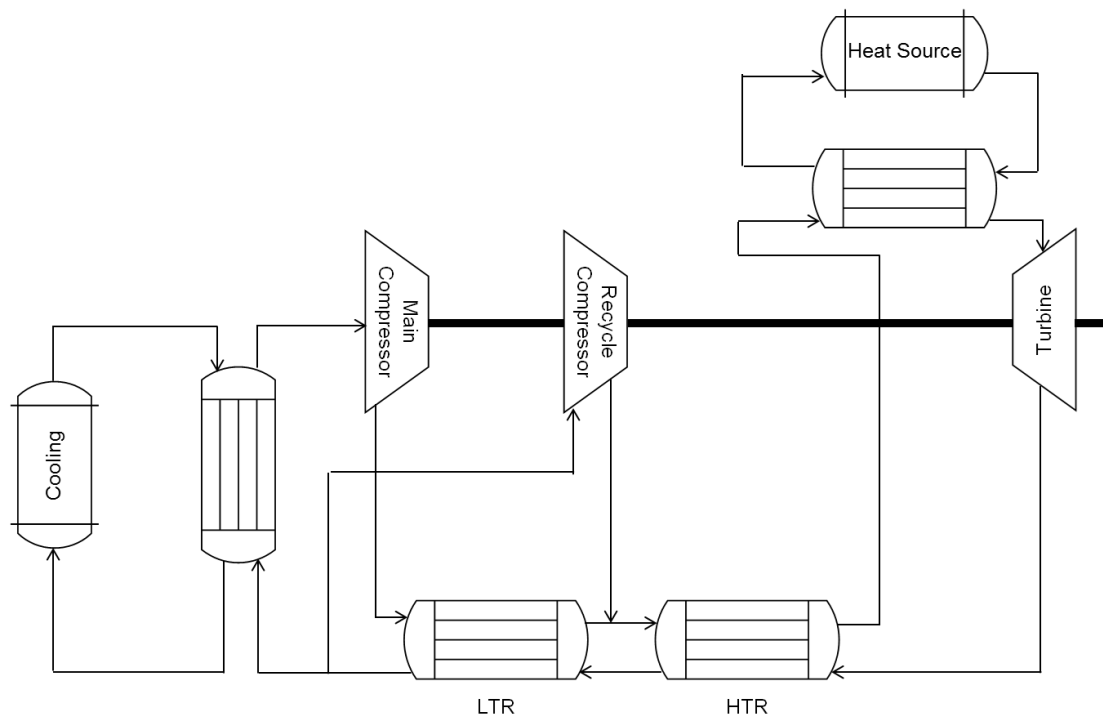


Figure 7 Indirectly heated supercritical power cycle

1.2.2 Directly heated supercritical power cycle

The configuration of a directly heated system is shown in Figure 8. In a directly heated cycle the combustion process directly heats up the turbine working fluid. The fuel and oxidizer are pressurized to supercritical stage utilizing a compression system. Afterwards, the fuel and oxidizer are combusted at a pressure ranging from 250 bar to 300 bar and delivered to the turbine for the

power generation. This high pressure is used since directly heated systems supposed to have all of the combustion products, H_2O and CO_2 , at a supercritical state. McClung et al. [1] are one of the few investigators who focuses on directly heated supercritical gas turbines. The authors investigated both cryogenic pressurized oxy combustion

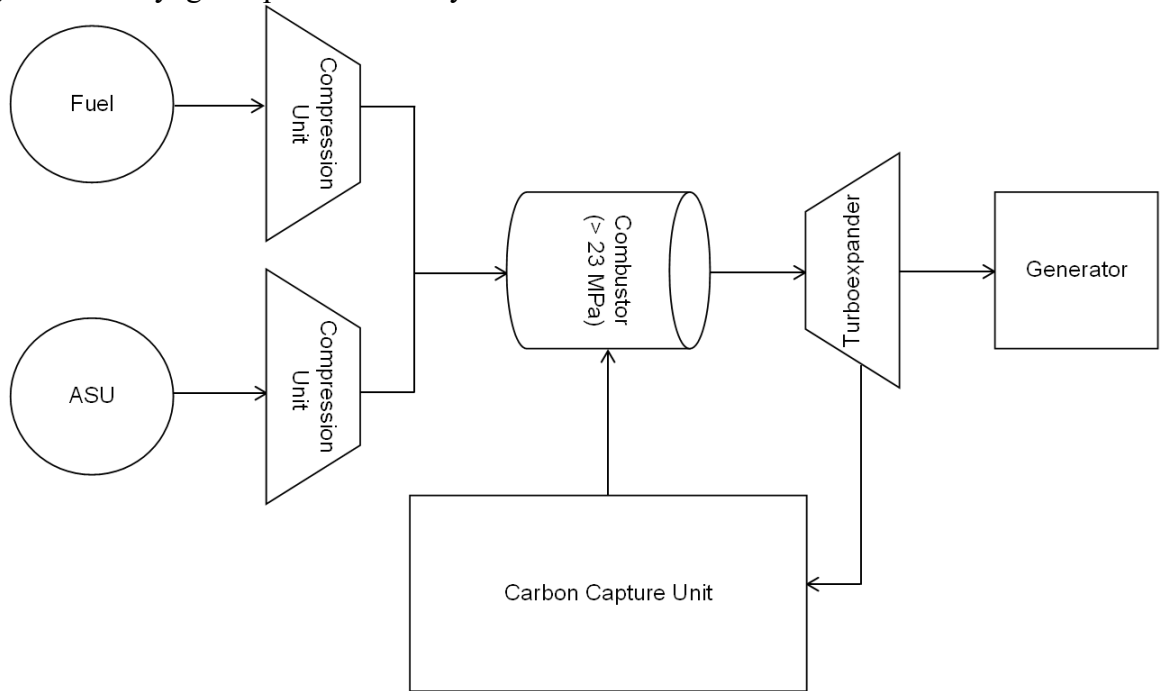


Figure 8 Directly heated supercritical power cycle

cycle (CPOC) and advanced supercritical oxy-combustion recompression Brayton cycle. According to McClung et al. [1], directly fired supercritical oxy-combustion cycles using the recompression closed Brayton cycle has potential to achieve a 64% thermal efficiency and 52% net plant efficiency. The combustion chamber pressure for the system analyzed is 290 bar and the turbine inlet temperature is 1493K. Chowdhury et al. [22] conducted a similar cycle analysis. It is observed that 60 % thermal efficiency can be achieved while supercritical oxy-methane combustion is employed in CPOC cycle for power generation. The cycle analysis is conducted at 300 bar pressure. Iwai [23] et al. discusses the development approach of the directly heated supercritical oxy-fuel combustor. The Allam cycle approach is obtained to design such a system

[23]. The authors mention that the plant implementation success much depends on the stable and efficient combustion at 300 bar. The similar kind of pressure range can be observed in rocket engine. However, the operation duration may vary due to different application purposes. The team investigates the effect of equivalence ratio, the combustor exit temperature, and the

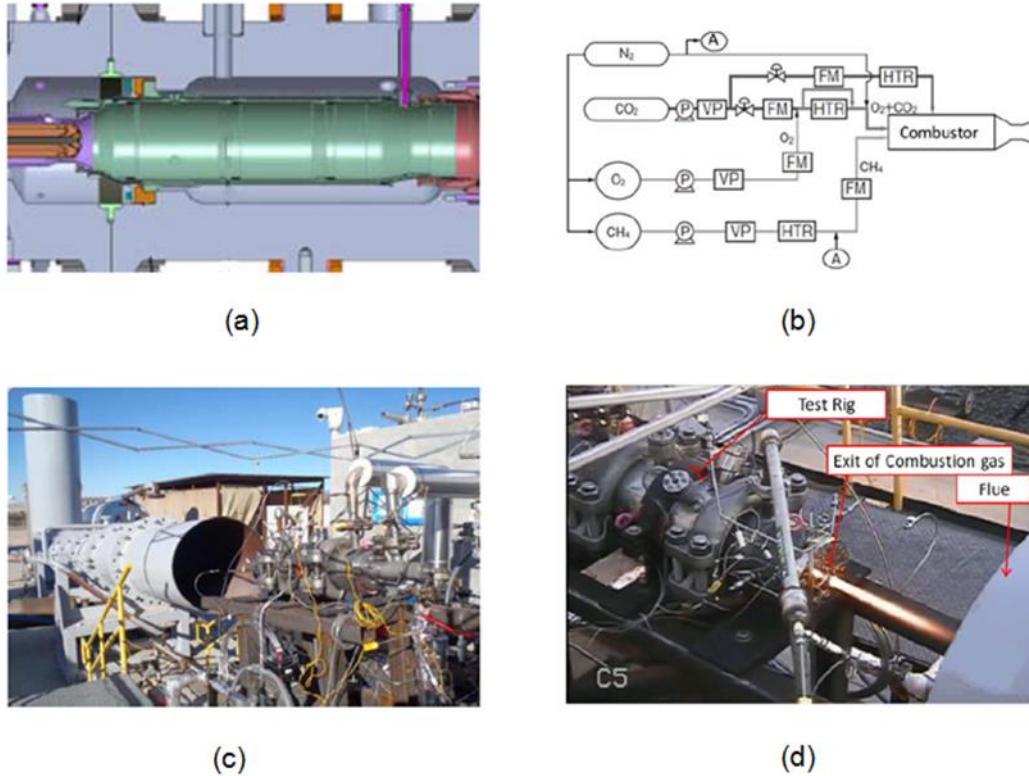


Figure 9 (a) Cross section of test combustor, (b) 30MPa combustion test system, (c) Test article installed on test stand, and (d) Test stand at time of ignition

pressure up to 300 bar for oxy-fuel combustion. The authors conclude that the combustor showed good operability over a wide range of equivalence ratio and O₂-CO₂ oxidizer percentages [23].

In recent time Toshiba Corporation collaborate with NET Power LLC, Chicago Bridge & Iron Company and Exelon Corporation in order to develop a combustor for supercritical CO₂ cycle [23]. The investigators have been chosen Allam cycle approach to design such a combustor. This particular cycle is designed to operate at 300 bar pressure while combusting oxy-fuel reactant with the combination of CO₂ diluents. The combustor is shown in Figure 9(a). This combustor has inner diameter of 83 mm, and the length of 409 mm. The oxygen enters into the combustion chamber

after passing through a swirl vane which creates a stability vortex similar to the conventional gas turbine. Afterwards, the mixture is ignited using Triethylaluminum/ Triethylborane compound which can be found in rocket engine combustor. The investigators have taken step increment approach to reach 30 MPa (300 bar) pressure. Thus, the ignition occurs at 1 MPa (10 bar) pressure, afterward, the pressure increases to 5 MPa (50 bar), 10 MPa (100 bar), 20 MPa (200 bar), and finally 30 MPa (300 bar). The luminosity of the flame is attributed by the Triethylaluminum/ Triethylborane. The total experiment is conducted for almost 260 s while 300 bar pressure was maintained for 80 s. The findings from this experiment are shown in Figure 10. The combustion temperature is measured 1300 °C at 30 MPa (300 bar) pressure while the mass flow ratio of oxygen, fuel, cooling for CO₂, and CO₂ for oxidizer is measured to be 0.2, 0.45, 0.5, and 0.87, respectively.

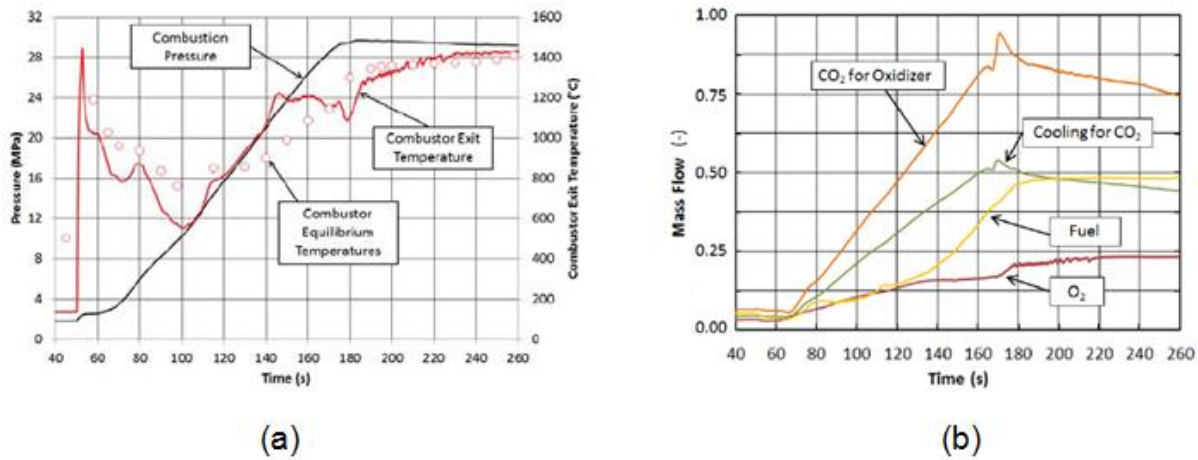


Figure 10 (a) Time trend of pressure and exit temperature, (b) Time trend of mass flow.

1.3 Project Objective

Even though directly heated supercritical oxy-fuel power generation possesses immense potential, this technology is still in the development stage. There are very few experimental works available in literature that have been conducted to explore and understand the flame characteristics.

The components to construct such a system still need to be developed. Furthermore, the behavior of supercritical fluids at high temperature is still unknown. Hence, theory and experimentation is not matured and precise computational modeling for the system is not available.

Motivated by the advantages of directly heated supercritical power cycle, the primary objective of this dissertation is to perform qualitative analysis on oxy-methane combustion at high pressure (< 20 bar) and compare to CFD model for future scale up to supercritical condition. For this purpose, a high pressure methane-oxygen fuel burner and combustor have been developed to accommodate oxy-combustion environment. A detailed CFD analysis is conducted to understand the flame length and cooling phenomenon inside the combustor first at pressures up to 20 bar to compare to experimentations then at supercritical pressure. The first part of the dissertation compares CFD results with high pressure burner experimentations at pressures up to 20 bar. The test was conducted for 30 s within 150 kW – 200 kW thermal power inputs. The inlet parameters for the CFD analysis are obtained from the test conditions. Afterwards, based on the CFD temperature profile a cooling system is proposed for steady state high pressure combustion experimentations. Furthermore, the study will also focus on the ignition delay due to added diluent during the combustion process. Using this CFD model, the supercritical oxy-methane burner and the combustor is proposed in this dissertation. Furthermore, an additional study is conducted to understand the impact of equation of state in the supercritical combustion simulation. A detailed CFD model for developing supercritical oxy-methane burner and the combustor is also presented. This analysis provides a preliminary guideline for developing a laboratory scale supercritical oxy combustor.

1.4 Practical Relevance

Conventional fossil fuel combustion processes use air as an oxidizer and produce a diluted CO_2 stream in their flue gases. This is due to the high N_2 concentration present in the stream from air, making the capturing process relatively expensive in terms of direct cost and efficiency penalty. When pure oxygen used as an oxidizer instead of air, primarily CO_2 and H_2O are produced

lending itself to have the carbon captured. The current study has been proposed oxy-fuel combustion instead of conventional air-combustion.

Furthermore, according to the United States Energy Information Administration (EIA), the majority of US energy was produced by coal and natural gas burning in 2016 [24]. The thermal efficiency of the conventional coal and natural gas-powered gas turbines falls between $\approx 30\%$ - 50% [25-32]. Due to the low efficiency of power plants, the system requires a huge amount of fuel burning for comparatively less energy production. These processes cause a large amount of greenhouse gas emissions. Generally,

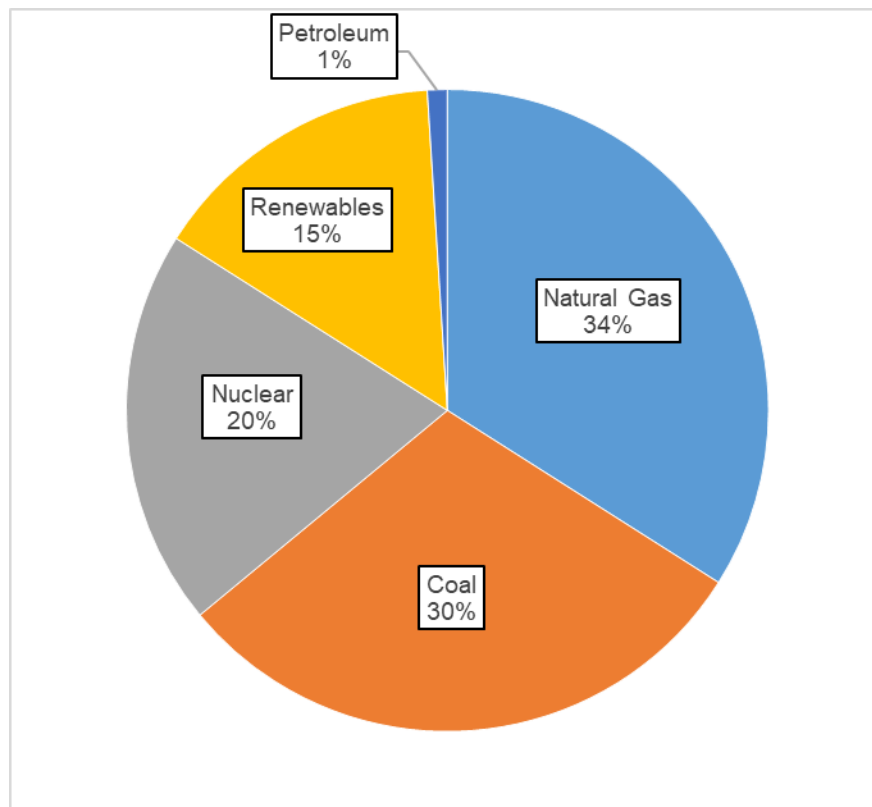


Figure 11 US Energy consumption scenario [24]

the conventional gas turbines generally operate at 30-50 bar pressure range depending on fuel and oxidizer inlet conditions [31]. On the other hand, the directly heated oxy-fuel supercritical gas turbines operate at 300 bar pressure. According to the NETL theoretical analysis, these types of

gas turbines offer more than 50 % thermal efficiency. Supercritical plants also provide the option of using methane and syngas as fuel [1,22]. Additionally, in the conventional gas turbine the combustion products come out as gaseous phase. In contrary, in the supercritical gas turbines the combustion process produces supercritical fluid, which is almost 3-5 times dense than conventional gas turbines. This will reduce the components size as well as the operational cost [1,2].

This dissertation study attempts to address some of the technological challenges during oxy combustion process. To begin with pure oxygen combustion results in elevated temperature which requires CO₂ dilution to cool down the flame. This may affect on the fuel burning rate and combustion efficiency [7-9]. It can also introduce ignition delay during the burning process. During this dissertation study oxy-methane combustion test was conducted up to 20 bar and the test conditions were replicated using the CFD. A comprehensive numerical study is performed to understand the oxy-methane combustion characteristics at high pressure (< 20 bar) using ANSYS Fluent and CHEMKIN PRO software package. The knowledge obtained from this study can be beneficial for the development of the high pressure and supercritical oxy-methane burner for steady state operation in future.

1.5 Commercial Potential

The outcome of this dissertation study can be useful to develop next generation gas turbines and coal combustors. The high pressure burner and the cooling system can be implemented into existing gas turbines without significant modifications. This will facilitate in achieving high efficiency power cycles without significant additional investments. Furthermore, the cooling system concept proposed in this study can mitigate the existing oxy-combustion high temperature problems. The burner can also be implemented into a coal combustor or furnace. The burners and igniters presented in this dissertation can also be used to ignite the pulverized coal mixture and can contribute to the overall power output. The igniter, in particular, is unique to fossil fuel energy systems and can be implemented into coal combustors at high pressures to ignite the coal mixtures.

During this dissertation study, a burner and a combustor is also developed for supercritical combustion conditions, which is useful for the directly heated supercritical power cycle component development.

Chapter 2: Design Methodology

The design methodology of a methane-oxygen burner, igniter, end cap and combustor wall cooling system are discussed in this chapter. The shear coaxial injection method is opted for the burner design. The shear-coaxial injector utilizes the shear forces between the fuel and oxidizer to disintegrate into ligaments and to mix [33]. The shear forces are driven by the momentum flux difference between two streams. A RCS rocket thruster is used as an ignition source. CFD analysis is conducted on the burner to understand the flame length, flame temperature and near wall temperature profile. Based on the analysis several modifications are proposed to make the combustor suitable for oxy-combustion experimentation.

2.1 Burner Design Methodology

The shear co-axial injector is intended to operate up to 250 kW and 20 bar pressure. Methane is used as the fuel along with pure oxygen as the oxidizer. The oxygen port is designed such a way that carbon dioxide can be diluted if required. The mass flowrate for the methane and oxygen are calculated from the power input using Equation 1 and 2 at stoichiometric condition. The lower heating value (LHV) characterizes the heat of combustion of the fuel [34,35]. The lower heating value of methane is 50,000 kJ/kg [34,35]. At stoichiometric condition the O/F ($O_{\text{xygen}}/F_{\text{uel}}$) ratio is 4.

$$\dot{m}_{\text{methane}} = \frac{\text{Firing Input}}{\text{LHV}} \quad (1)$$

$$\dot{m}_{\text{oxygen}} = \dot{m}_{\text{methane}} \times (O/F)_{\text{st.}} \quad (2)$$

The shear co-axial injector utilizes the shear force differential between the fuel and oxidizer to mix [33]. The shear forces are initiated by the momentum flux difference between two streams. Therefore, when designing a shear-coaxial injector, two non-dimensional parameters velocity ratio (VR) and momentum flux ratio (J) are thoroughly observed. The formula for velocity ratio and momentum flux ratio is shown Equation 3 and 4 [33].

$$VR = \frac{v_{\text{methane}}}{v_{\text{oxygen}}} \quad (3)$$

$$J = \frac{(\rho \cdot v^2)_{\text{methane}}}{(\rho \cdot v^2)_{\text{oxygen}}} \quad (4)$$

The pressure drop across the injector are calculated using the energy equation, Equation 5.

$$\frac{P_1}{\rho} + \frac{1}{2}v_1^2 + gz_1 = \frac{P_2}{\rho} + \frac{1}{2}v_2^2 + gz_2 + h_{\text{loss}} \quad (5)$$

The total head loss consists of major and minor losses. The major losses occur due to fluid friction, on the other hand, minor losses occur mostly due to the valves, tees, bends, contractions, expansions etc. The formula for major is shown in Equation 6.

$$h_{\text{major}} = f \times \left(\frac{L}{D_h} \times \frac{v^2}{2g} \right) \quad (6)$$

The major loss is a function of friction coefficient, characteristic length, hydraulic diameter and velocity. Then friction coefficient depends on the turbulence of the of the flow. The turbulence of a flow is determined by Reynold's number. The Reynolds number is a ratio between the inertial force and viscous force. It be calculated using Equation 7 [36].

$$Re = \frac{\rho v D_h}{\mu} \quad (7)$$

In Equation 7, ' ρ ' is density, ' v ' is velocity, ' D_h ' is hydraulic diameter and ' μ ' is dynamic viscosity. For turbulent flow the friction coefficient can be evaluated using the simplified Colebrook equation which is provided by Haaland, Equation 8 [36].

$$f = -1.8 \log \left[\frac{6.9}{Re} + \left(\frac{\epsilon/D_h}{3.7} \right)^{1.11} \right] \quad (8)$$

The Equation 8 is a function of Reynolds number (Re), surface roughness (ϵ) and hydraulic diameter (D_h). The friction coefficient obtained from Equation 8 is applicable for new pipes. The coefficient may increase by a number of 5 to 10 for old pipes.

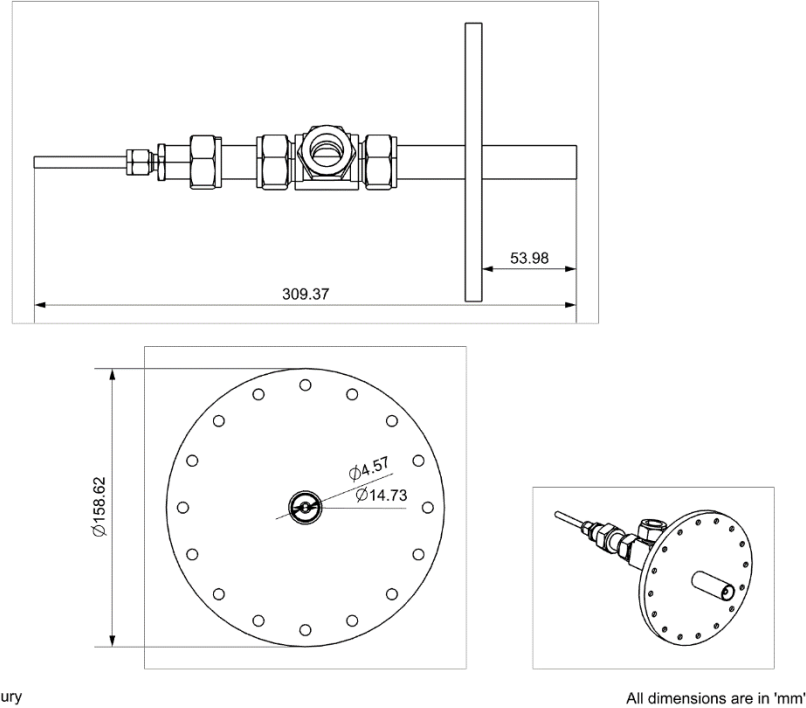
The design specifications for the methane-oxygen burner can be summarized as followings:

- Firing Input: up to 250 kW
- Combustion method: Oxy-methane
- Operating Pressure: up to 20 bar

The image of the burner can be seen in Figure 12. The burner is designed such a way that it can be operated at different firing inputs up to 250 kW. The maximum operating conditions for the burner can be found in Table 2.

Table 2 Main burner maximum operating condition

Power Input (kW)	250
Operating Pressure (bar)	20
Operating Temperature (K)	1000
Momentum flux ratio	2-20
Power Input (kW)	200
Operating Pressure (bar)	20



Author: Arifur Chowdhury

All dimensions are in 'mm'

Figure 12 Main burner

It is found from the literature that recessing the high velocity jet port with respect to the injection plane may enhance the combustion performance [33]. Kendrick et al. [39] found that a recess of $1d_i$ (where ' d_i ' represents high velocity jet diameter) in LOx/H₂ combustion increases the flame expansion rate and width of the flame volume. Tripathi et al. [40] investigated that the increment of momentum flux ratio or recess length enhances the jet breakup. The authors also have found that the effect of recess length is higher when the momentum flux ratio is small. However, it is demonstrated that increasing the recess length above $1.5d_i$ does not further improve the combustion performance [40]. Although, Wheeler and Kirby[41] have found that a recess length

close to $1.3d_i$ in LOx/CH₄ combustion still demonstrate a further enhancement in term of combustion efficiency. For the proposed injector the recess length of $1d_i$ is used, Figure 13.

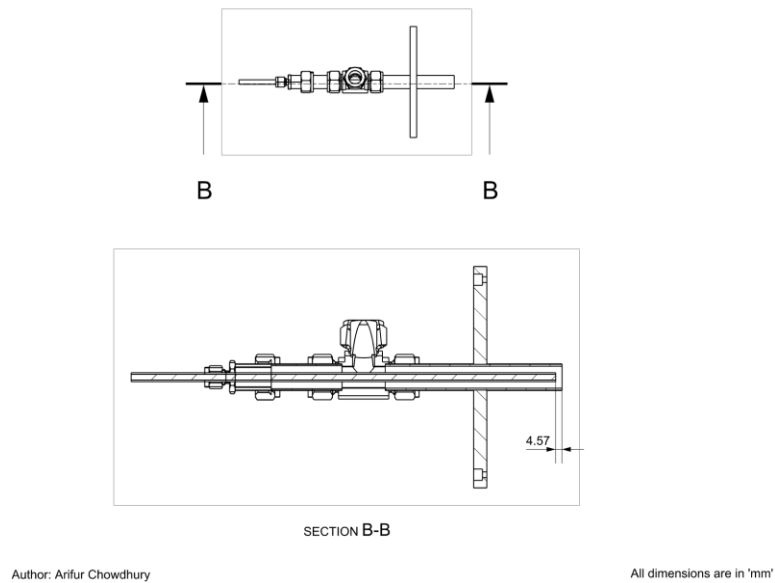


Figure 13 Main burner recess length

2.2 Igniter Design Methodology

The injector will be ignited using a pilot flame. The pilot flame manifolds are situated at the two sides of the combustor, Figure 14. The igniter design is opted from Sanchez et al. [42]. The spark igniter is designed to operate using oxygen and methane. The ignition system uses an internal swirl injection where the mixing of the working fluids is directed by the momentum of interacting streams. Oxidizer flows through an axial inlet and is impacted by four tangential fuel inlets that create a swirl that mixes the propellants prior to ignition. The igniter manifold can be seen in Figure 14.

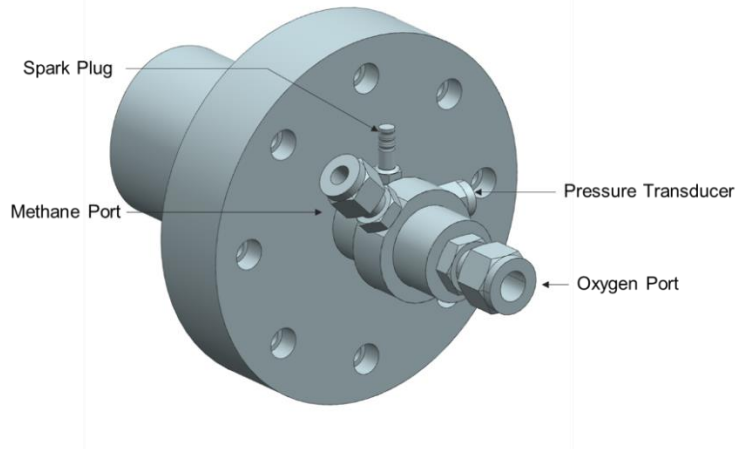


Figure 14 Igniter

Two igniters are mounted radially at the combustor body. The main burner fuel and oxidizer mixer hits the ignition flame at the perpendicular direction. The igniter system has two standard fluid interfaces, methane and oxygen. The oxygen gas is injected through the center of the igniter whereas the methane gas mixes vertically. The inlet connections for the igniter burner fuel and oxidizer is 1/4-inches (6.35 mm) and 3/8-inches (9.525 mm) tubing respectively. The inlet pressures of the fuel and oxidizer those the unit has been tested is 8 – 13 bar gas operation. The unit has been tested with D series Cryogen Solenoid valves connected with 1/4" (6.35 mm) inch tubing. These valves have a maximum operating pressure of 26 bar. The igniter is designed to be installed into a 0.532-inches (13.5 mm) diameter hole so that the flame exit is flush with the combustion device inner wall. A circular boss is fabricated with a matching thickness to install the 1.5-inches (38.1 mm) -long tube of the igniter into the combustion device. It is necessary to close the igniter inlet valves when the combustor chamber pressure exceeds the inlet pressure to the igniter valve to prevent back flow into the igniter. The igniter operational burn time is 3 to 5 seconds. The operating conditions for the igniter can be found in Table 3.

Table 3 Igniter operating condition

Inlet Igniter Port Pressures (bar)	8 – 13
------------------------------------	--------

Combustion Chamber Pressure (bar)	5- 10
Mixture Ratio	1-3
Maximum burn time (seconds)	5
Igniter Body Temperature (K)	150 - 800

A standard 1/4-32 spark plug (PART #: EVOG10350) is the ignition source for the torch igniter. The voltage output of the spark plug when connected to a 5V 2.4A power source with a signal generation. Otherwise, the ignition source is a standard 1/4–32 spark plug connected to a 12 W power source with a signal generation of 150 Hz. The produced excitation voltage is 12 kV.



Figure 15 1/4-32 spark plug

2.3 End Cap Design Methodology

The existing combustor has an exit diameter of 11-inch (280 mm). However, to pressurize the combustor up to 20 bar the exit area must be reduced. The combustor is intended to pressurize by manipulating the exit area. The exit of the combustor has a converging nozzle. At ideal condition the critical pressure ratio for hot combustion gas product is 0.58 [41]. The critical pressure ratio can be calculated equation 9,

$$\text{Critical Pressure Ratio} = \frac{P^*}{P_0} \quad (9)$$

Where, ‘P*’ is the exit pressure and ‘P₀’ is the chamber pressure. During the test the combustion products are released to the atmosphere, 1 bar. Therefore, if the chamber pressure raises above 1.9 bar the flow at the exhaust will be choked. It is known that at choked condition the velocity of exhaust flow is Mach 1. The throat area is calculated using Equation 10.

$$\dot{m} = \frac{A^* P_t}{\sqrt{A_t}} \sqrt{\left(\frac{\gamma}{R}\right) \left(\frac{\gamma+1}{2}\right)^{\frac{-\gamma+1}{2(\gamma-1)}}} \quad (10)$$

The combustor end cap is designed such a way that the exit area can be manipulated to vary the chamber pressure. The combustor end cap consists of three flanges, Figure 16. The first flange is attached with the combustor main body and the second flange is bolted with the first flange. The diameter reduction from first and second flanges are 7-inches (178 mm) and 3-inches (76 mm), respectively. The third flange is attached with the second flange. The third flange is equipped to attach a small exit diameter adapter to pressurize the combustor.

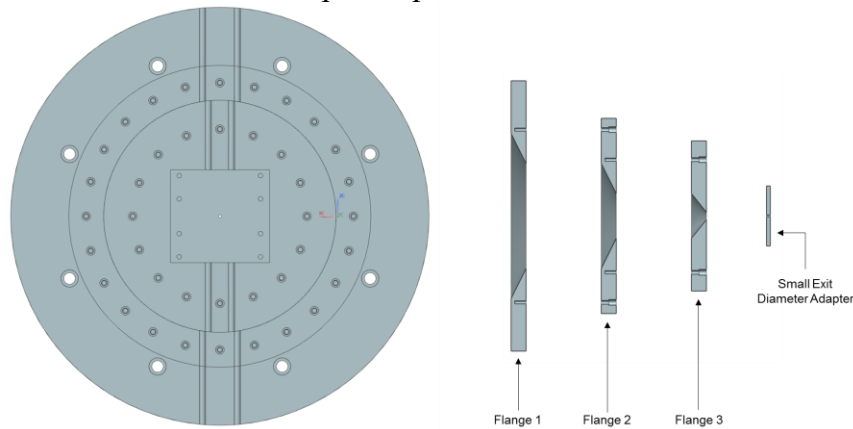


Figure 16 Combustor end cap

2.4 Combustor Cooling System Design

When methane and oxygen combust, the residuals, assuming complete combustion, are water and carbon dioxide. Garlborg and Bentzen [21], Richards et al. [44], Hainsworth et al. [45] have summarized that carbon dioxide can be an effective diluent for reducing the combustion temperature to material operation limit. In a typical oxy-combustion power generation system, the water is condensed and the CO_2 is recirculated into the combustion chamber [44-45]. For this reason, CO_2 is selected to be used for cooling since it could be obtained from the combustion flue gases. To meet the cooling system requirements, the design shown in Figure 17 are proposed. This apparatus will inject a high velocity ring of room temperature CO_2 along the inner walls of the combustor. In this configuration, CO_2 will act as a protective layer, keeping the walls at a low temperature and protect them from the high temperature steam that may lead to accelerated corrosion.

As seen in Figure 17, the CO₂ face plate will be removable. This modular design will enable a quick change of plates for different configurations without having to disassemble all the combustor. The plate could be changed for another with less or more open area depending on the desired CO₂ velocity.

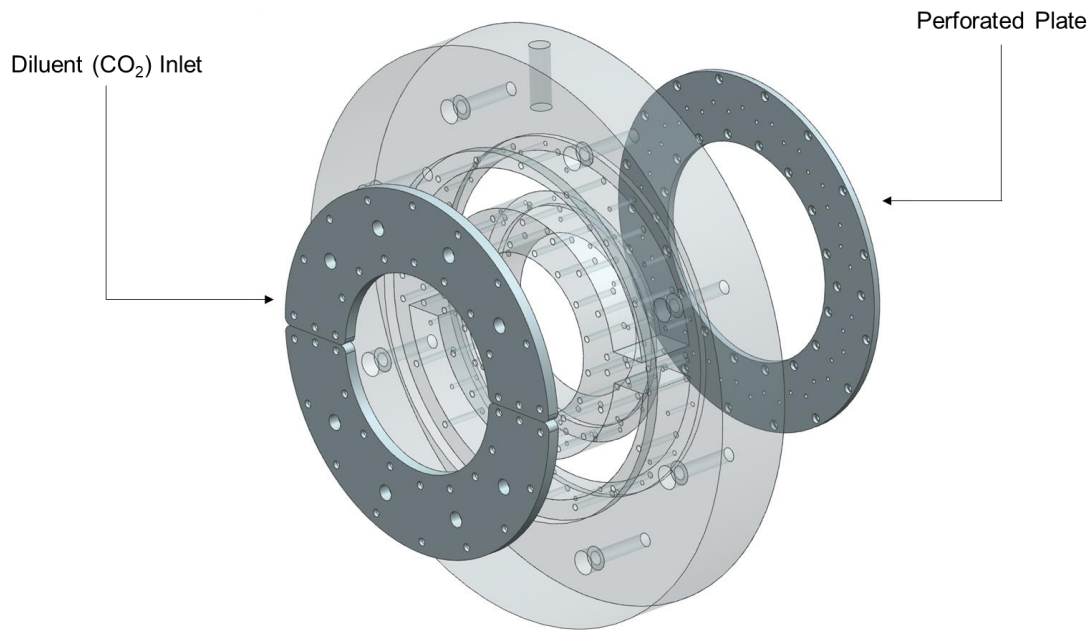


Figure 17 CO₂ cooling manifold

2.5 Combustor Parts Dimensions

In this section the dimensions are presented for the different parts of the combustor. The combustor parts are made out of stainless steel 410. There are four main combustor parts: (i) front cap, (ii) combustor body, (iii) metal window and (iv) end cap. The front cap consists of three parts: (i) front cap body, (ii) diluent (CO₂) inlet and (iii) perforated plate. The main burner is attached to the front cap through a center port. The combustor body is 648 mm long and has 280 mm inner diameter. The wall thickness of the combustor wall is 88 mm. The combustor body has six different ports which are used for optical access, igniter installation, and temperature and pressure

measurement devices installation purposes. The detailed dimensions of the combustor parts are shown from figure 19 to 22.

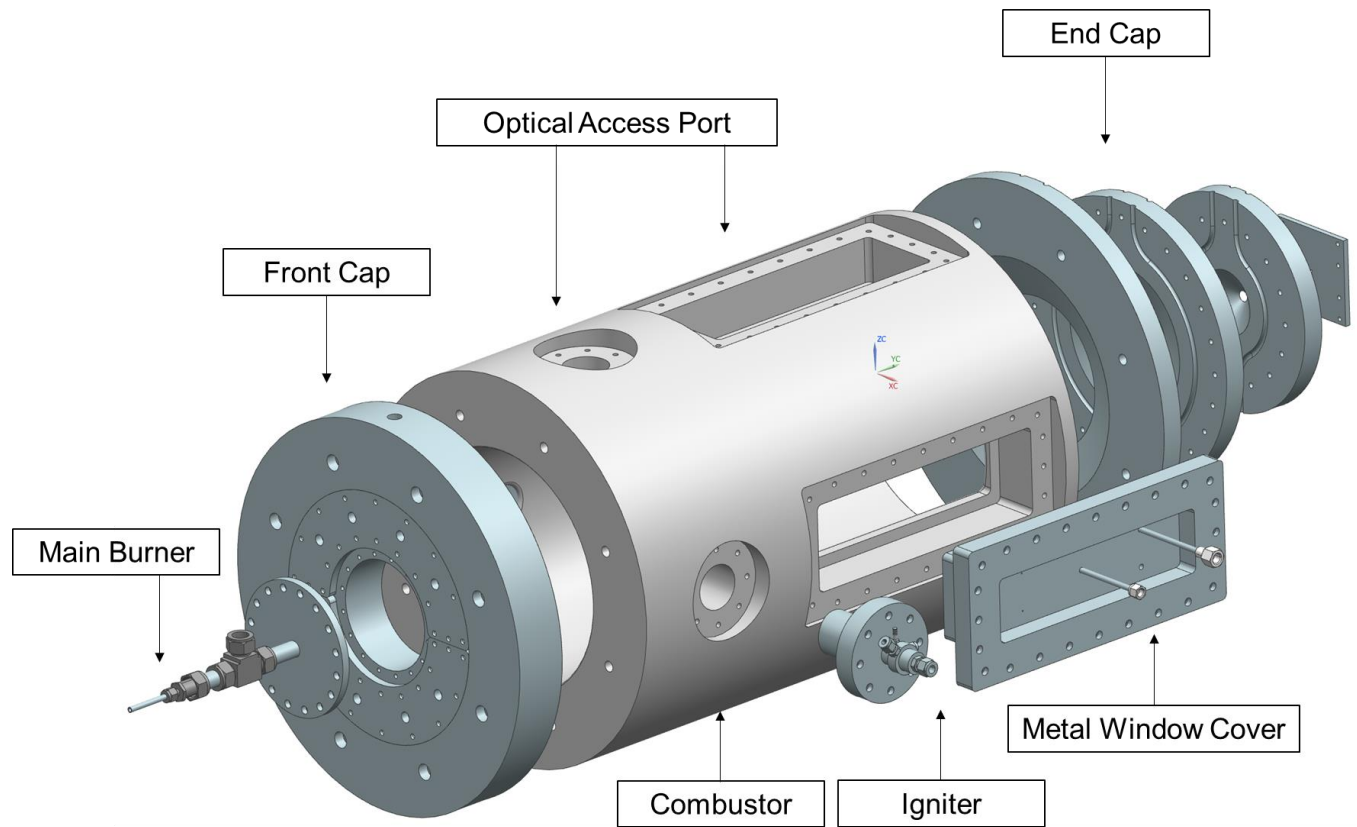


Figure 18 Combustor (exploded view)

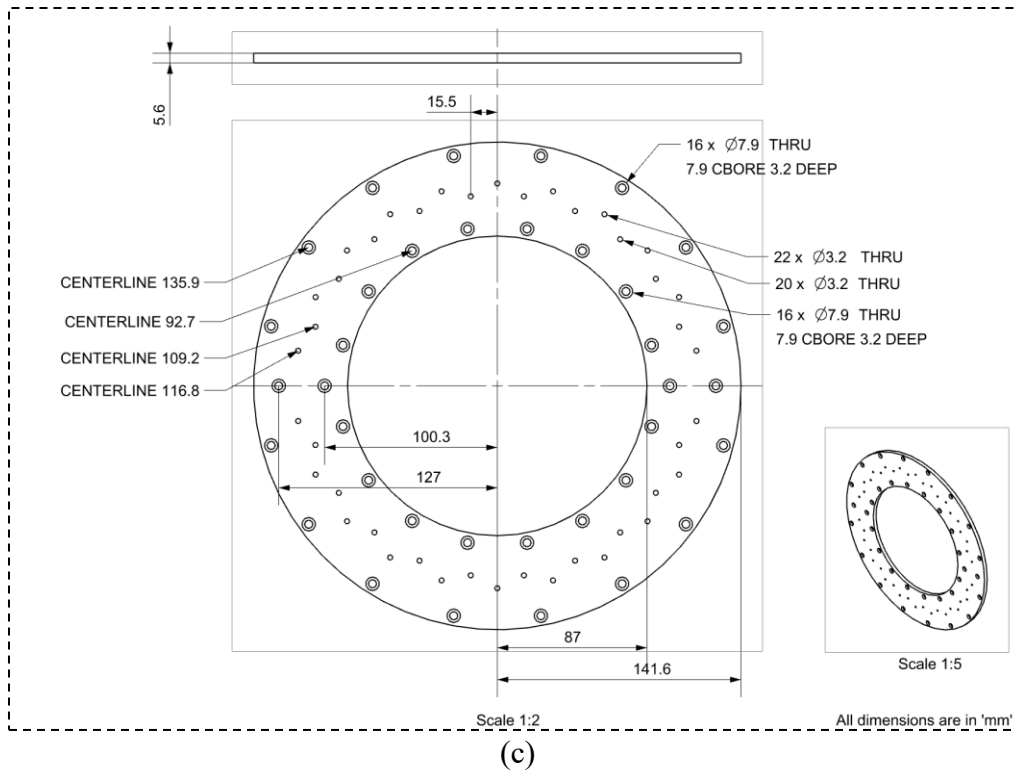


Figure 19 Combustor front cap (a) front cap body, (b) diluent inlet plate and (c) perforated plate

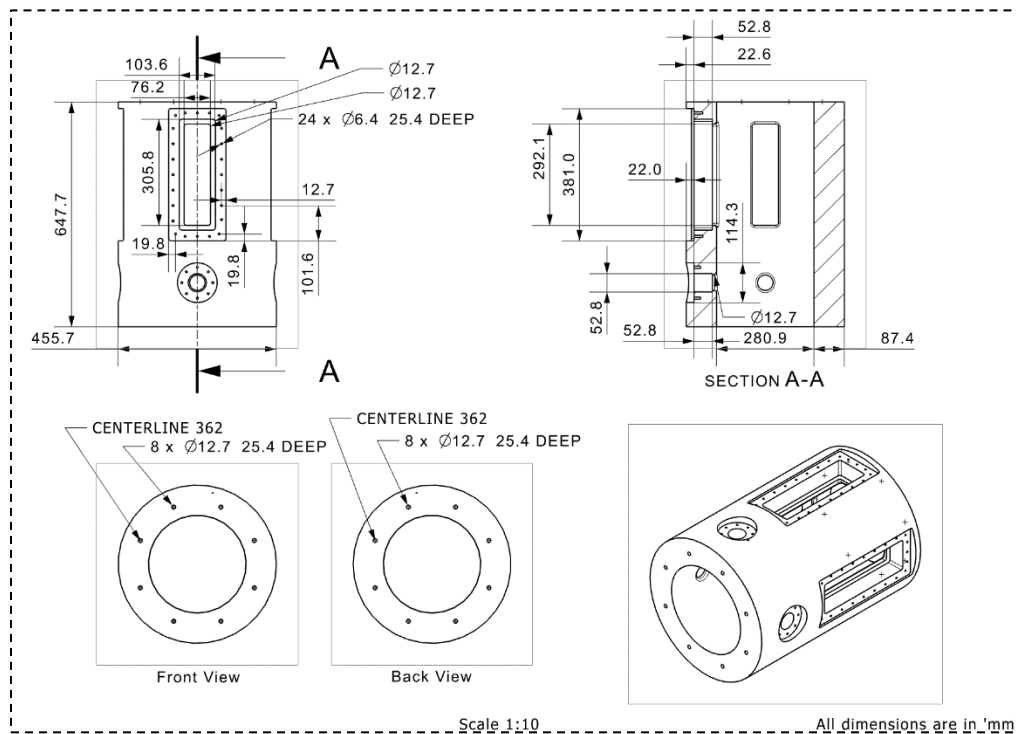
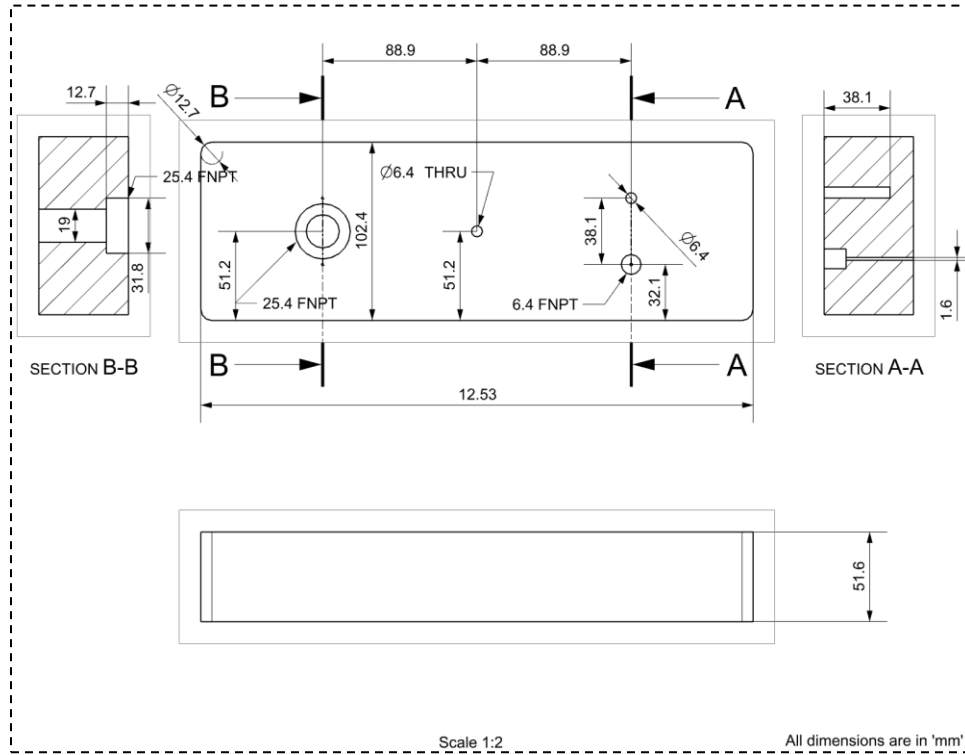
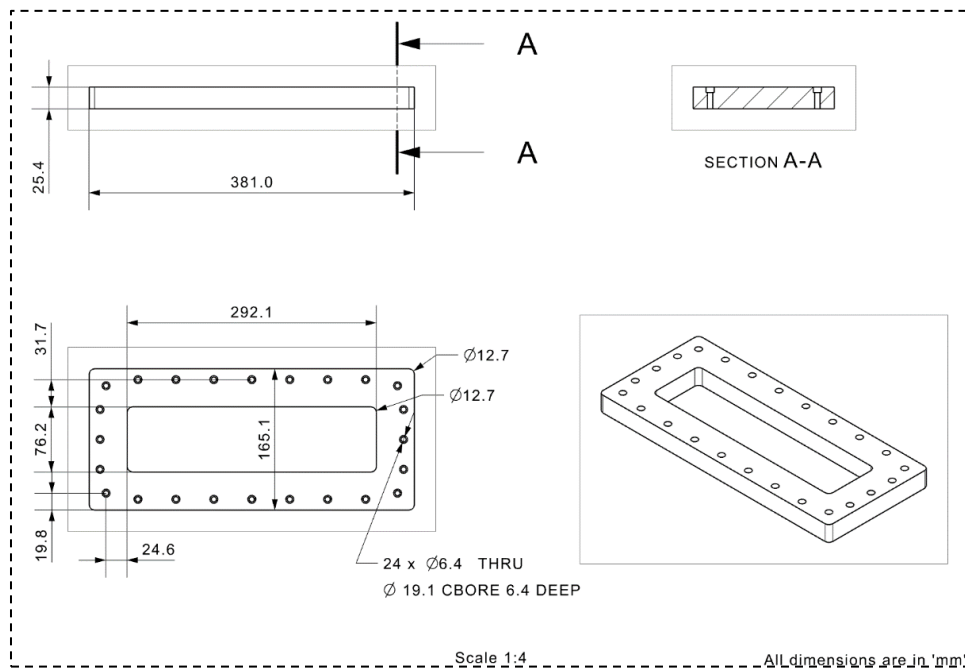


Figure 20 Combustor body

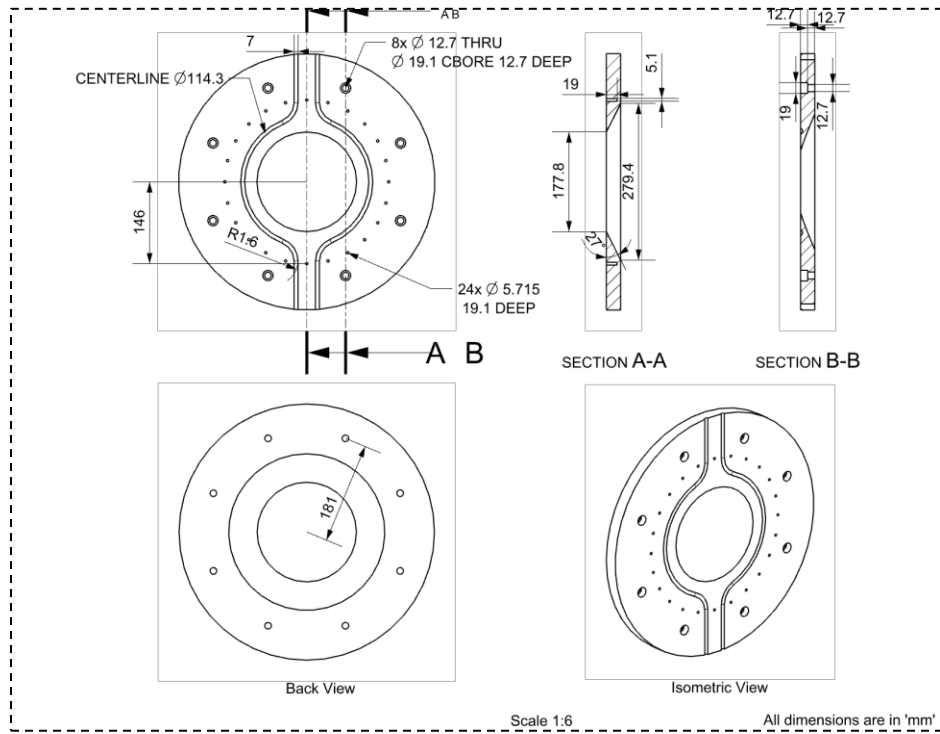


(a)

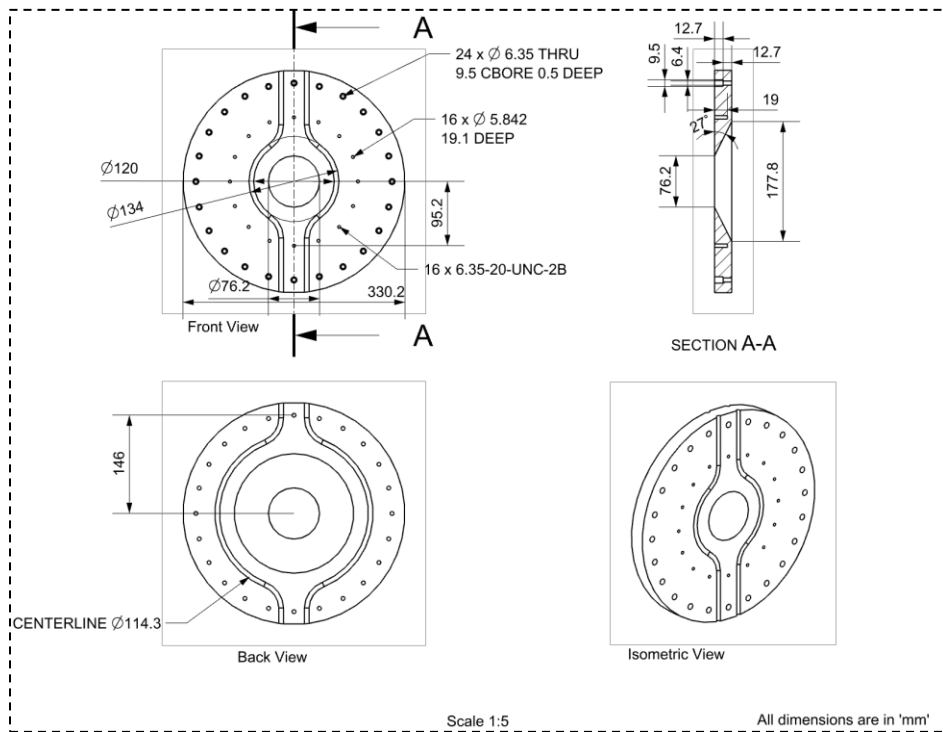


(b)

Figure 21 Combustor metal window cover (a) metal window and (b) window attachment plate



(a)



(b)

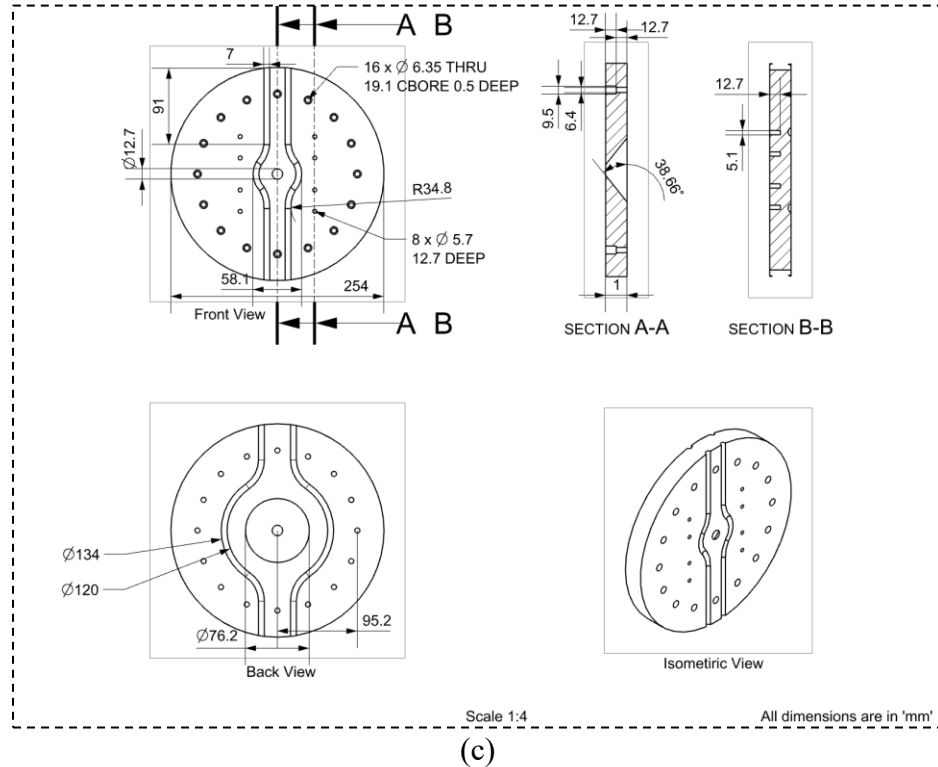


Figure 22 Combustor end cap (a) part 1, (b) part 2 and (c) part 3

2.6 Numerical Investigation Methodology

A numerical analysis is performed to observe the flame temperature, wall temperature, flame length and carbon dioxide cooling inside the combustor. The analysis is conducted using ANSYS Fluent commercial software. The simulation is performed in 2D domain instead of 3D. This reduces the computational time as well as computational complicity. The geometry and mesh are also generated using ANSYS software tool. The CFD analysis is performed in two steps. At first only the burner CFD investigation is performed. During the analysis the input parameters are obtained from the experimental study. Then a qualitative comparison is performed between the CFD results and the test data in terms of flame characteristics and exit diameter. Afterwards, based on the burner test results and CFD analysis the cooling system is designed. At the second step the

combustor CFD analysis is performed incorporating cooling system. The 2D geometry formation method, mesh and detailed numerical analysis approach is discussed in this chapter.

2.6.1 Burner CFD Analysis

2.6.1.1 Geometry and Mesh

The simulation is performed in 2D domain to reduce the computational time. Therefore, a simplified geometry is created to portrait the combustor into 2D. The combustor mainly consists of the burner, ignitor and end cap. The combustor has an inner radius of 0.14 m and 0.65 m long. While creating the 2D geometry, the dimensions are selected such a way that the cross-sectional areas of main burner, and exit nozzle remain constant as 3D. The equivalent areas for different ports are provided in Table 4.

Table 4 Cross- sectional area inlet and exit port

Port Type	Cross-Sectional Area (cm ²)
Main Burner (CH ₄)	1.64E-01
Main Burner (O ₂)	1.63E-00
Exit Diameter	4.72E-01

Furthermore, an additional fluid domain is added after the exit nozzle section. The pressure boundary condition is input at the end of the added fluid domain. In this way, the CFD simulation calculates the pressure inside the combustor based on the combustion product composition, gas temperature and exit area.

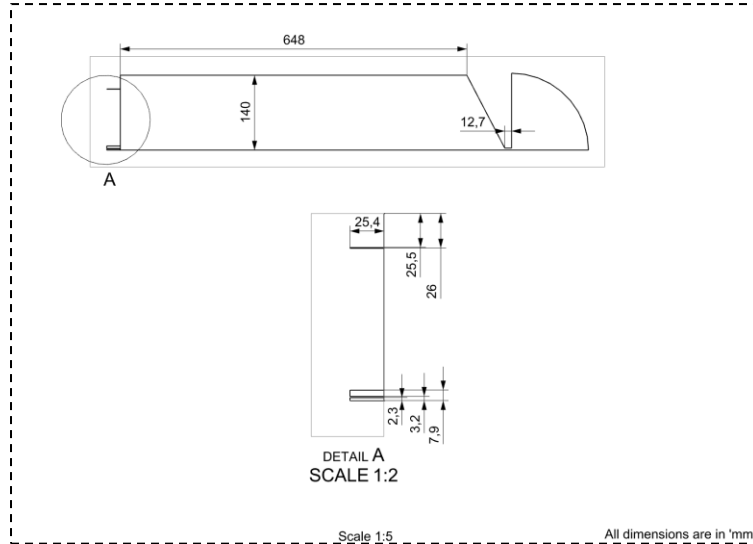


Figure 23 Combustor in 2D domain

The whole geometry is sliced into three sections to achieve better control over the mesh dimension selection. The 2D geometry can be seen in Figure 23. The structured mesh is generated using ANSYS mesh tool, Figure 24. The total number of elements and node are $\approx 446,000$ and $\approx 448,000$ respectively, Figure 24. The average orthogonal quality is 0.95 (the worst cells have an orthogonal quality closer to 0 and the best cells have an orthogonal quality closer to 1).

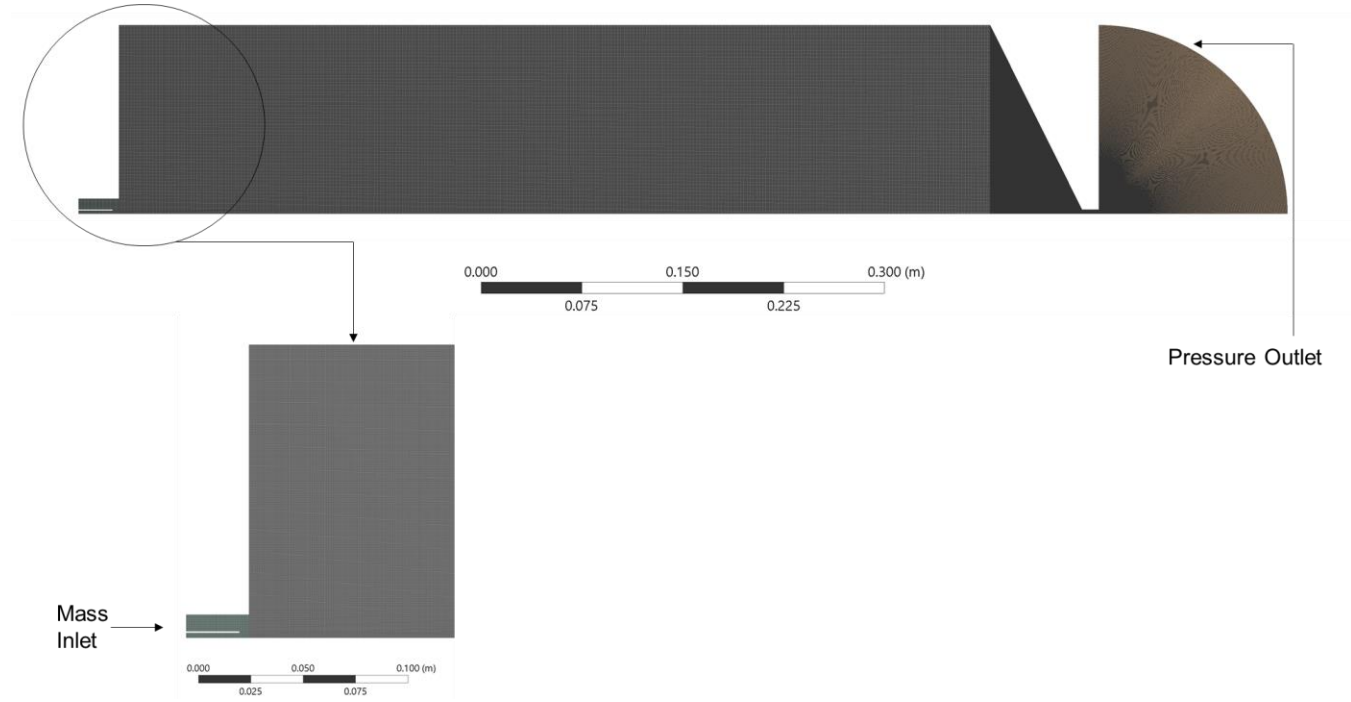


Figure 24 Mesh (High pressure test replication)

2.6.1.2 Governing Equations

ANSYS Fluent solves RANS (Reynolds Average Navier Stokes) equations to simulate the fluid flow. RANS models are the most economical approach when it comes to complex fluid flow problems [10]. In this technique, the Navier Stokes equation is evaluated based on average and fluctuation components of pressure and velocity. The conservation of mass or continuity equation can be written as:

$$\frac{\partial \rho}{\partial t} + \nabla \cdot (\rho \vec{v}) = 0 \quad (11)$$

The conservation of momentum in an inertial reference frame can be written as:

$$\frac{\partial}{\partial t} (\rho \vec{v}) + \nabla \cdot (\rho \vec{v} \vec{v}) = -\nabla p + \nabla \cdot (\bar{\tau}) + \rho \vec{g} + \vec{F} \quad (12)$$

where, p is the static pressure, $\bar{\tau}$ is the stress tensor respectively. The stress tensor $\bar{\tau}$ is described as:

$$\bar{\tau} = \mu [(\nabla \vec{v} + \nabla \vec{v}^T) - \frac{2}{3} \nabla \cdot \vec{v} I] \quad (13)$$

where μ is the molecular viscosity, I is the unit tensor. The equation for the conservation of energy is given as:

$$\frac{\partial}{\partial t} (\rho E) + \nabla \cdot (\vec{v}(\rho E + p)) = -\nabla \cdot (\sum_j H_j J_j) + S_h \quad (14)$$

In this Equation, source term S_h contains any defined volumetric heat sources.

2.6.1.3 Turbulence Model

Two-equation models are most commonly used for turbulence modeling in commercial CFD software. In this technique two transport equations are iteratively solved and the Reynolds Stresses are modeled using the Eddy Viscosity approach. Robustness, economic approach, and reasonable accuracy for a wide range of turbulent flows make these methods popular in industrial flow and heat transfer simulations [10]. In this particular study standard k- ϵ turbulence model is used.

Standard k- ϵ Model

The standard k- ϵ model is one of the most popular two equation turbulence models become a well-known turbulence modeling technique for practical engineering flow calculations since it was proposed by Launder and Spalding [43]. The standard k- ϵ model is a semi-empirical turbulence model based on the turbulent kinetic energy (k) and its dissipation rate (ϵ). While deriving the k- ϵ model, the flow is assumed fully turbulent, and the effects of molecular viscosity are neglected. Therefore, the standard k- ϵ model is only valid for fully turbulent flows. The turbulent kinetic energy (k) and its dissipation rate (ϵ) can be obtained from in Equation 15 and 16 transport equations.

$$\frac{\partial}{\partial t} (\rho k) + \frac{\partial}{\partial x_i} (\rho k u_i) = \frac{\partial}{\partial x_j} \left[\left(\mu + \frac{\mu_t}{\sigma_k} \right) \frac{\partial k}{\partial x_j} \right] + G_k + G_b - \rho E - Y_M + S_K \quad (15)$$

$$\frac{\partial}{\partial t} (\rho E) + \frac{\partial}{\partial x_i} (\rho E u_i) = \frac{\partial}{\partial x_j} \left[\left(\mu + \frac{\mu_t}{\sigma_\epsilon} \right) \frac{\partial E}{\partial x_j} \right] + C_{1\epsilon} \frac{\epsilon}{k} (G_k + C_{3\epsilon} G_b) + C_{2\epsilon} \rho \frac{\epsilon^2}{k} + S_\epsilon \quad (16)$$

where, G_k and G_b are the generation of turbulent kinetic energy because of the mean velocity gradients and buoyancy, respectively. $C_{1\epsilon}, C_{2\epsilon}$ and $C_{3\epsilon}$ are constants. σ_k and σ_ϵ are the turbulent Prandtl numbers for k and ϵ , respectively. The turbulent viscosity, μ_t , is determined by combining turbulent kinetic energy and its dissipation rate terms, which is described as follows:

$$\mu_t = \rho C_\mu \frac{k^2}{\epsilon} \quad (17)$$

The model constants $C_{1\epsilon}, C_{2\epsilon}, C_\mu, \sigma_k$ and σ_ϵ have the following values:

$$C_{1\epsilon} = 1.44, C_{2\epsilon} = 1.92, C_\mu = 0.09, \sigma_k = 1.0, \sigma_\epsilon = 1.3$$

2.6.1.4 Boundary Conditions

A steady state pressure based solver is used for the calculations. For simulating the combustion, the non-premixed combustion model is employed. The combustion products are evaluated via pdf table. The P-1 radiation model is incorporated with the model to simulate the radiation effect. The pressure is set to be 1 bar at the outlet of the added fluid domain, Figure 23. A summary of the computational model is shown in Table 5.

Table 5 CFD boundary conditions (High pressure test replication)

Section	Input
General	
Type	Pressure Based
Time	Steady State
Models	
Energy	On
Viscous Model	k- ϵ (Standard)
Radiation	P-1 (On)
Species	Non-Premixed Combustion
Boundary Conditions	
Method	Axisymmetric Boundary
Inlets	<ul style="list-style-type: none"> - Fuel (Methane) Inlet Temperature: 300 K - Oxidizer (Oxygen) Inlet Temperature: 300 K - Diluent (Carbon Dioxide) Inlet

Outlet Wall	Temperature: 300 K Pressure Outlet: 1 bar Combustor Wall: Convection Fluid Domain Wall: Temperature (300K)
Solution	
Method	- Scheme-Coupled - High Order Term Relaxation
Initialization	Hybrid

Chapter 3: Experimental Methodology

The experimental apparatus consists of three sub-systems: (I) the feed delivery system, (II) the data acquisition and control system and (III) the combustor test bed. The feed system is remotely controlled using a data acquisition (DAQ) system. The combustor is mobile and positioned on a trailer. These mobile facilities allow for the transporting of the test setup to a remote location during a test day for safety. For this reason, the DAQ system is also mobile. The following sections provide more details on each of the experimental test systems.

3.1 Feed System

The feed system consists of the gas tank K-bottles bank fitted with pressure regulators, needle valves, solenoid valves, manual ball valves, thermocouples, pressure transducers and flowmeters. The fuel, oxidizer and diluents are delivered from the K-bottles. The K-bottles are situated in two different locations. The K-bottles for the main burner is located 15 m away from the combustor. On the other hand, the K-bottles for the igniters are located adjacent to the combustor. The detailed view of the feed system can be found in Figure 25. The area bounded by the red rectangle is located 15 m away from the main test side. This is where the main burner gas tanks are situated. The gas tank regulators are selected based on the test conditions. The maximum operating pressure during the test will be 20 bar. Therefore, the tank regulators are selected such a way that they able to provide up to 35 bar delivery pressure. The needle valves are positioned immediately after the regulators. The placement of the needle valves facilitates controlling of the gas flow during the test if necessary. During the test, carbon dioxide is used as the diluent. Due to the pressure difference between the gas tanks and the feed delivery system carbon dioxide may condense while feed into the feed system from the gas tank. Therefore, a thermocouple is placed in the diluents line. The thermocouple will measure the gas temperature in the line. The normally closed solenoid valves are put in the line to remotely control the flow. The solenoid valves have the response time of 0.5 s for opening the valves. The manual ball valves are placed to manually control the gas flow. The abundance of manual ball valves and solenoid valves is because of

compartmentalization and safety. These valves also provide enhanced control during the operation of the system.

The methane and oxygen tank regulators have 6.35 mm compression outlet connections. The carbon dioxide tank regulator has 12.7 mm compression outlet connections. The 15 m tubing connecting the main burner methane, oxygen, carbon dioxide gas tanks and the trailer valve train is 25.4 mm tubing. An adapter is used to convert the 6.35 mm and 12.7 mm tubing to 25.4 mm tubing. Afterwards, different sizes adapters are used to feed fuel, oxidizer and diluents into the combustor. The inlet connections for the main burner fuel is 6.35 mm and oxidizer connection is 19.05 mm tubing. The inlet connections for the igniter burner fuel and oxidizer is 6.35 mm and 9.53 mm tubing, respectively. The cooling manifold has eight inlets. The inlet connections for the cooling system manifolds are 12.7 mm . The feed lines are leak checked using nitrogen gas. Detailed images of the feed system can be seen in Figure 26 a-c. Detailed instrumentation list and data collection rate can be found in Table 6.

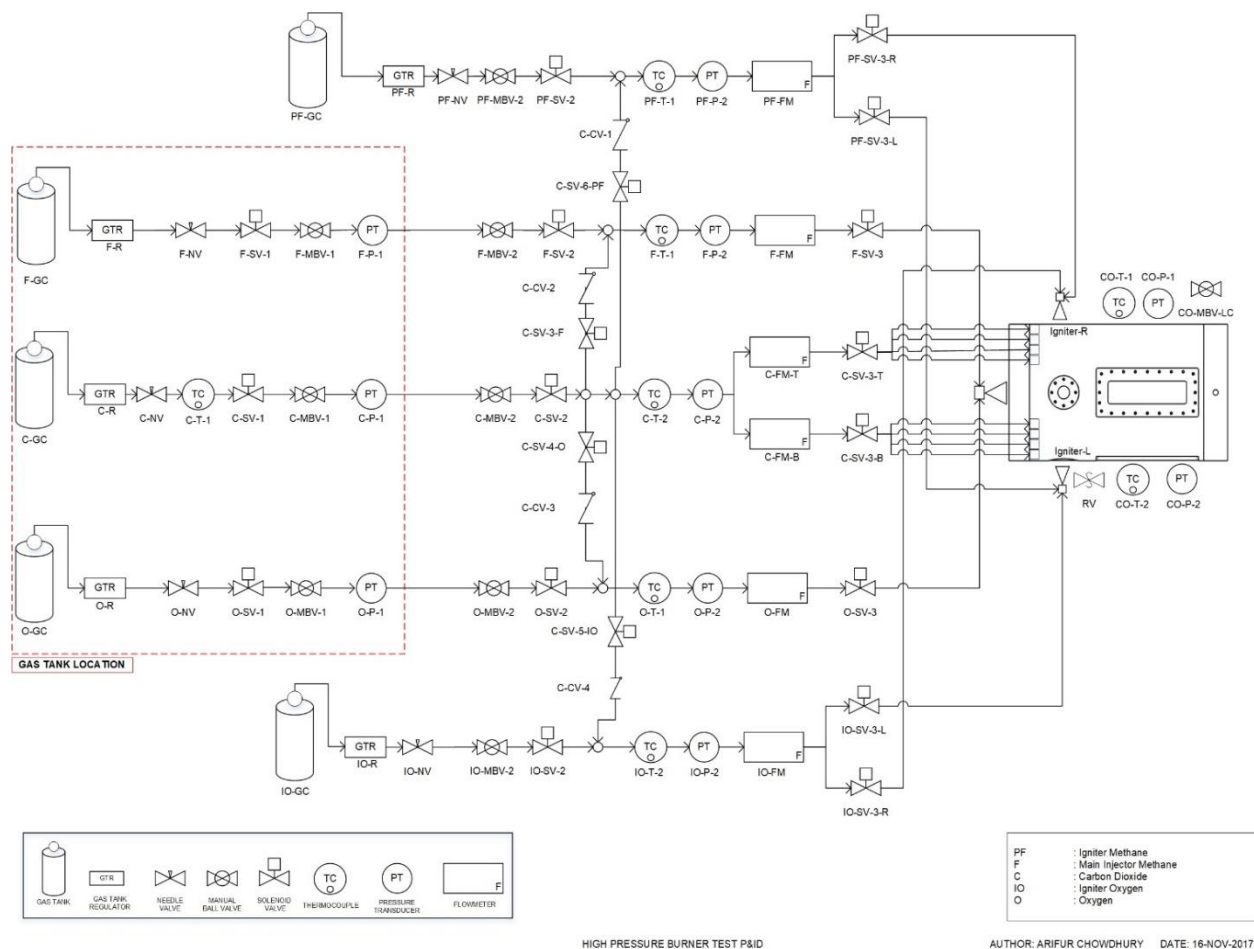


Figure 25 Piping and Instrumentation diagram

Table 6 Part type and data collection rate

Schematic Notation	Part Type	Data Collection Rate
Oxygen - Main Burner		
O-NV	Needle Valve	
O-SV-1	Solenoid Valve	
O-MBV-1	Ball Valve	
O-NV	Needle Valve	
O-P-1	Pressure Transducer	10 Hz
O-MBV-2	Ball Valve	
O-SV-2	Solenoid Valve	
O-T-1	Thermocouple	1 Hz
O-P-2	Pressure Transducer	10 Hz
O-FM-MI	Flowmeter	1 Hz
O-SV-3-MI	Solenoid Valve	
Carbon Dioxide		

C-NV	Needle Valve	
C-T-1	Thermocouple	1 Hz
C-SV-1	Solenoid Valve	
C-MBV-1	Ball Valve	
C-NV	Needle Valve	
C-P-1	Pressure Transducer	10 Hz
C-MBV-2	Ball Valve	
C-SV-2	Solenoid Valve	
C-SV-4-O	Solenoid Valve	
C-SC-6-PF	Solenoid Valve	
C-SV-5-IO	Solenoid Valve	
C-SV-3-F	Solenoid Valve	
C-T-2	Thermocouple	1 Hz
C-P-2	Pressure Transducer	10 Hz
C-FM-T-1	Flowmeter	1 Hz
C-FM-B-1	Flowmeter	1 Hz
C-SV-3-T	Solenoid Valve	
C-SV-3-B	Solenoid Valve	
Igniter - Methane		
PF-NV	Needle Valve	
PF-SV-1	Solenoid Valve	
PF-MBV-1	Ball Valve	
PF-NV	Needle Valve	
PF-P-1	Pressure Transducer	10 Hz
PF-MBV-2	Ball Valve	
PF-SV-2	Solenoid Valve	
PF-T-1	Thermocouple	1 Hz
PF-P-2	Pressure Transducer	10 Hz
PF-FM	Flowmeter	1 Hz
PF-SV-3-L	Solenoid Valve	
PF-SV-3-R	Solenoid Valve	
Igniter -Oxygen		
IO-NV	Needle Valve	
IO-SV-1	Solenoid Valve	
IO-MBV-1	Ball Valve	
PF-NV	Needle Valve	
IO-P-1	Pressure Transducer	10 Hz
IO-MBV-2	Ball Valve	
IO-SV-2	Solenoid Valve	
IO-T-1	Thermocouple	1 Hz
IO-P-2	Pressure Transducer	10 Hz

IO-FM	Flowmeter	1 Hz
IO-SV-3-L	Solenoid Valve	
IO-SV-3-R	Solenoid Valve	
Methane- Main Burner		
F-NV	Needle Valve	
F-SV-1	Solenoid Valve	
F-MBV-1	Ball Valve	
F-NV	Needle Valve	
F-P-1	Pressure Transducer	10 Hz
F-MBV-2	Ball Valve	
F-SV-2	Solenoid Valve	
F-T-1	Thermocouple	1 Hz
F-P-2	Pressure Transducer	10 Hz
F-FM-MI	Flowmeter	1 Hz
F-SV-3-MI	Solenoid Valve	
Combustor		
RV	Relief Valve	
CO-MBV-LC	Ball Valve	
CO-T-1	Thermocouple	1 Hz
CO-T-2	Thermocouple	1 Hz
CO-P-1	Pressure Transducer	10 Hz
CO-P-2	Pressure Transducer	10 Hz

Table 7 shows the ranges, vendors and model numbers of the parts.

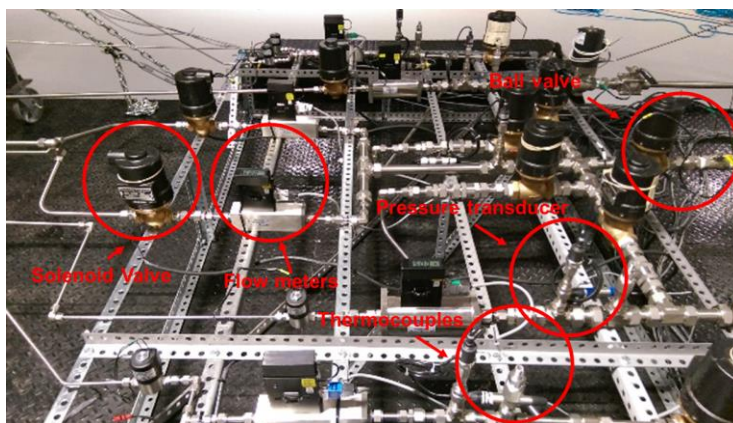
Table 7 Feed system parts specifications

Part Type	Part	Vendor	Part/ Model No.
Solenoid Valve	F-SV-1, F-SV-2, C-SV-1, C-SV-2	McMaster	4640K34
Solenoid Valve	O-SV-1, O-SV-2	Clark Cooper	EH70
Solenoid Valve	O-SV-3, C-SV-3-T, C-SV-3-B, C-SV-3-F, C-SV-4-O, C-SV-5-IO, C-SV-6-PF	McMaster	4640K18
Solenoid Valve	IO-SV-3-L, IO-SV-3-R, PF-SV-3-L, PF-SV-3-R, F-SV-3	Gemsensors	
Flowmeter	O-FM	Omega	FMA1700A/1800A
Flowmeter	F-FM, IO-FM	Omega	FMA1700A/1800A
Flowmeter	C-FM-B-1, C-FM-B-2, PF-FM	Omega	FMA1700A/1800A
Pressure Transducer	O-P-1, O-P-2, F-P-1, F-P-2, C-P-1, C-P-2, IO-P-2, PF-P-2	Grainger	G17M0215F2500
Relief Valve	RV	Grainger	541FEBKMAA0300
Thermocouple	CO-T-1, CO-T-2	Omega	M12JSS-1/8-U-6-B
Thermocouple	C-T-1, C-T-2, O-T-1, F-T-1, PF-T-1, IO-T-1	Omega	M12JSS-1/2-U-6-B
Ball Valve	IO-MBV-1, PF-MBV-1	Swagelok	SS-45S8
Ball Valve	O-MBV-1, O-MBV-2, F-MBV-1, F-MBV-2, C-MBV-1, C-MBV-2,	Swagelok	SS-AFSS16
Check Valve	C-CV-1, C-CV-2, C-CV-3, C-CV-4	Swagelok	SS-CHS16-1/3
Needle Valve	IO-NV, PF-NV	Swagelok	SS-18RS8
Needle Valve	C-NV	Swagelok	SS-12NBS12
Needle Valve	O-NV, F-NV	Swagelok	SS-12NBS16

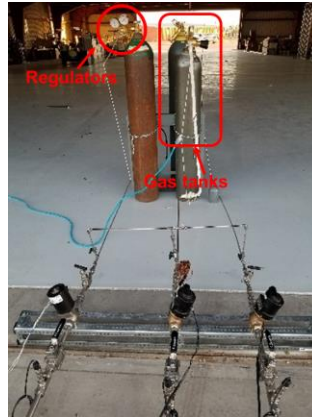
Table 8 shows the specifications of the gas tank regulators.

Table 8 Gas tank regulators specifications

Oxygen Gas Tank Regulator	
CGA	CGA 540
Outlet Connection	1/4" Swagelok®
Pressure Range	5-550 psig
Vendor	Victor
Model Number	Model SR600-550-540 Heavy Duty High Pressure Single Stage Regulator
Airgas Part	VIC0781-1610
Methane Gas Tank Regulator	
CGA	CGA-350
Outlet Connection	1/4" Swagelok®
Pressure Range	50 - 750 psig
Vendor	Victor
Model Number	Model SR4F-350 High Capacity High Pressure Piston Methane Or Hydrogen Calibration Single Stage Regulator
Carbon Dioxide Gas Tank Regulator	
CGA	CGA- 320
Outlet Connection	5/8" - 18 UNF (Female)
Pressure Range	50 - 750 psig
Vendor	Victor
Model Number	Model SR4F-320 High Capacity High Pressure Piston Carbon Dioxide Single Stage Regulator
Inert Gas Carbon Dioxide Gas Tank Regulator	
CGA	CGA-580
Outlet Connection	1/4" Swagelok®
Pressure Range	5 - 550 psig
Vendor	Victor
Model Number	Model SR600-550-580 Heavy Duty High Pressure Inert Gas Single Stage Regulator



(a)



(b)



(c)

Figure 26 (a) Valve train on the trailer (b) Valve train close to the main burner gas tank facility and (c) test setup

3.2 Data Acquisition and Control System

The solenoid valves are remotely operated using the DAQ. The thermocouples, pressure transducers and flowmeters also record data from the system during an experiment. The schematic for the DAQ system can be seen in Figure 27. The main test setup to DAQ station provides supervisory, control and signals for both direct and alternating current devices on the burner test and the burner test feed system. The test station houses an Ethernet network allowing DAQ systems

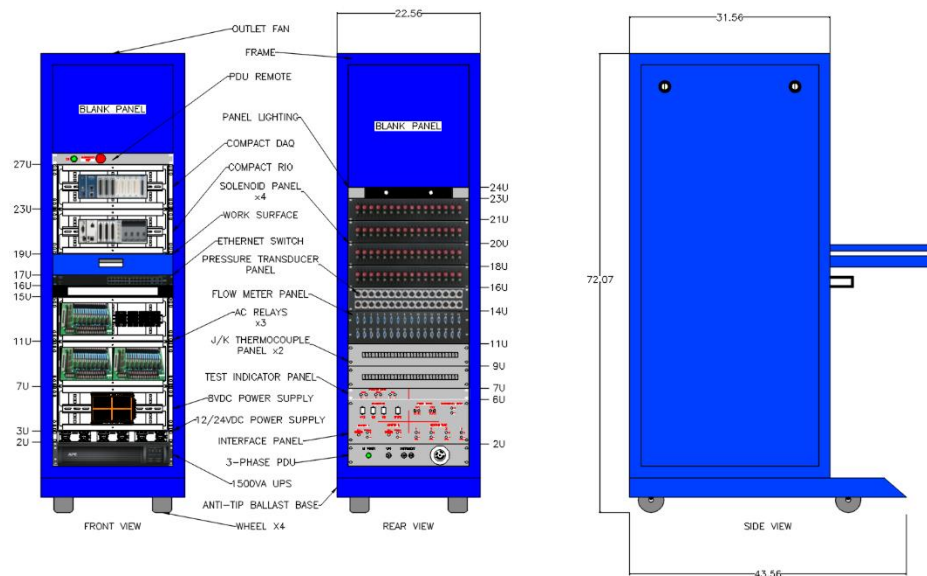


Figure 27 DAQ and control system



Figure 28 LabView Interface

to communicate to a remote computer or data center via fiber-optic link. Power for the test station and all instrumentations are provided by the test station via a three phase 120 VAC/60Hz, grounded power source. The test station has the capacity of controlling up to 64 solenoids and recording data from 32 pressure transducers, 32 flowmeters, and 60 thermocouples.

The LabView control interface is shown in Figure 28. The LabView window provides real time information about the line pressure, line temperature, flowrates, combustor pressure and combustor temperature. The solenoid valves can be manually operated using LabView. During the test, at the beginning the lines are pressurized by manually opening the solenoid valves. The combustor is equipped with two different igniters. Two of these igniters have separate spark plugs. The spark plugs can be operated using the program. The LabView is programmed such a way that the test can be conducted using pre-programmed auto sequence. It also allows to record the necessary data during the test. It is also equipped with ‘EMERGENCY STOP’. The ‘EMERGENCY STOP’ can be initiated due to any malfunctioning during the test. The ‘EMERGENCY STOP’ will also be automatically initiated if the combustor wall temperature reaches above 600K. Table 9 demonstrate the LabView back panel connections interfaces.

Table 9 LabView back panel connection interfaces (a) flowmeter, (b) pressure interface, (c) thermocouple and (d) solenoid valve

(a)		
LabVIEW Reference	Module Reference	Back Panel Reference
Main Burner - Oxygen		
O-FM-MI	cDAQ1Mod1/ai0	MFM-1
Main Burner - Fuel		
F-FM-MI	cDAQ1Mod1/ai1	MFM-2
Igniter-Methane		
PF-FM	cDAQ1Mod1/ai2	MFM-3
Igniter- Oxygen		
IO-FM	cDAQ1Mod1/ai3	MFM-4
Carbon Dioxide		
C-FM-T-1	cDAQ1Mod1/ai4	MFM-5
C-FM-T-2	cDAQ1Mod1/ai5	MFM-6
C-FM-B-1	cDAQ1Mod1/ai6	MFM-7
C-FM-B-2	cDAQ1Mod1/ai7	MFM-8

(b)

LabVIEW Reference	Module Reference	Back Panel Reference
Main Burner - Oxygen		
O-P-1	cDAQ1Mod3/ai0	A-1
O-P-2	cDAQ1Mod3/ai1	A-2
Main Burner - Fuel		
F-P-1	cDAQ1Mod3/ai2	A-3
F-P-2	cDAQ1Mod3/ai3	A-4
Igniter- Methane		
PF-P-1	cDAQ1Mod3/ai4	A-5
PF-P-2	cDAQ1Mod3/ai5	A-6
Igniter- Oxygen		
IO-P-1	cDAQ1Mod3/ai6	A-7
IO-P-2	cDAQ1Mod3/ai7	A-8
Carbon Dioxide		
C-P-1	cDAQ1Mod3/ai16	A-9
C-P-2	cDAQ1Mod3/ai17	A-10
Combustor		
CO-P-1	cDAQ1Mod3/ai18	A-11
CO-P-2	cDAQ1Mod3/ai19	A-12

(c)

LabVIEW Reference	Module Reference	Back Panel Reference
Main Burner - Oxygen		
O-T-1	cDAQ1Mod4/ai0	TC-K-1
Main Burner - Methane		
F-T-1	cDAQ1Mod4/ai1	TC-K-2
Igniter - Methane		
PF-T-1	cDAQ1Mod4/ai2	TC-K-3
Igniter- Oxygen		
IO-T-2	cDAQ1Mod4/ai3	TC-K-4
Carbon Dioxide		
C-T-1	cDAQ1Mod4/ai4	TC-K-5
C-T-2	cDAQ1Mod4/ai5	TC-K-6
Combustor		
CO-T-1	cDAQ1Mod4/ai6	TC-K-7
CO-T-2	cDAQ1Mod4/ai7	TC-K-8

(d)

LabVIEW Reference	cRIO Reference	Back Panel Reference
Main Burner- Oxygen		
O-SV-1	DIO 0	A-1
O-SV-2	DIO 1	A-2
O-SV-3-MI	DIO 2	A-3
Main Burner- Methane		
F-SV-1	DIO 3	A-4
F-SV-2	DIO 4	A-5
F-SV-3-MI	DIO 5	A-6
Igniter- Methane		
PF-SV-1	DIO 6	A-7
PF-SV-2	DIO 7	A-8
PF-SV-3-L	DIO 8	A-9
PF-SV-3-R	DIO 9	A-10
Igniter -Oxygen		
IO-SV-1	DIO 10	A-11
IO-SV-2	DIO 11	A-12
IO-SV-3-L	DIO 12	A-13
IO-SV-3-R	DIO 13	A-14
Carbon Dioxide		
C-SV-1	DIO 14	A-15
C-SV-2	DIO 15	A-16
C-SV-3-F	DIO 16	B-1
C-SV-3-T	DIO 17	B-2
C-SV-3B	DIO 18	B-3
C-SV-4-O	DIO 19	B-4
C-SV-5-IO	DIO 20	B-5
C-SV-6-PF	DIO 21	B-6

3.3 The Combustor Test Bed

The combustor is placed on a 5.5 m x 2 m trailer. The combustor stand is secured with the trailer using three metal chains. The igniter fuel and oxidizer gas tanks are also positioned on the trailer. The gas tanks are strapped with the tank stand. The tank stand is bolted with the trailer. The trailer is rested on four car jacks. Two of the jacks can carry 6 metric tons of weight and another two jacks can carry 4 metric tons. During the test the trailer is transported outside the facility building and placed 15 m away from the building.

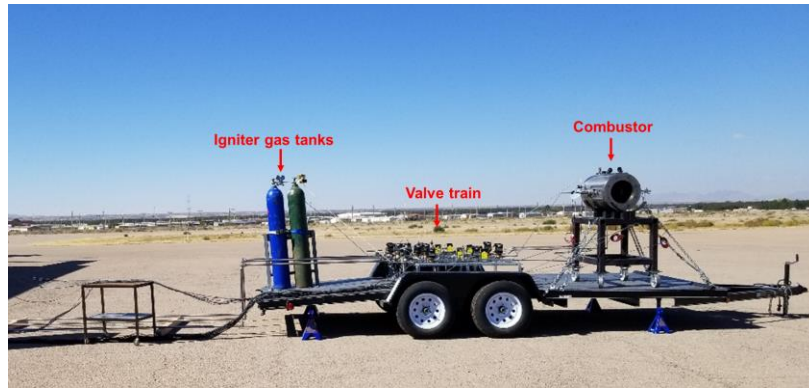


Figure 29 Combustor test bed

Chapter 4: Results and Discussion

In this section the test data and CFD results are presented and discussed. The ultimate goal of the project is to develop a laboratory scale 300 bar oxy-combustor for continuous operation. To understand the combustion chamber pressurization mechanism and flame behavior at high pressure, a combustor is designed to operate steady state up to 20 bar. This dissertation study presents the test data for transient tests up to 20 bar. The test parameters are used to perform CFD analysis which is essential for developing the combustor cooling system for steady state operation. The simulation is performed in 2D domain instead of 3D. This reduces the computational time as well as computational complicity. The geometry and mesh are also generated using ANSYS software tool. The 2D geometry formation method, mesh and detailed numerical analysis approach is discussed in chapter 2. Based on the CFD analysis a cooling system is proposed for the combustor. An analysis is performed using Chemkin Pro software package to understand the ignition delay due to the CO₂ dilution. Finally, a CFD analysis is conducted incorporating the CO₂ cooling system and results are presented. The cooling system proposed for the high pressure (up to 20 bar) combustor will be used for cooling the supercritical (up to 300 bar) oxy-methane combustor as well.

4.1 Experimental Results

The combustion test is conducted at different pressures up to 20 bar to understand the combustor operability. The test duration is 34s which includes 4s of igniter operation and 30s of main burner operation. The knowledge obtained from these tests are vital for designing a laboratory scale steady state high pressure (up to 20 bar) combustor and supercritical combustor (up to 300 bar). The pressurization process of a combustion chamber possesses immense challenge. The pressurization of a chamber mostly depends on the inlet mass flowrates, exit area and gas properties. The combustor is designed such a way that the inlet mass flowrates can be manipulated by regulating the tank regulators and the exit area can be manipulated by attaching different end cap adapters. For this particular study, the exit area is kept constant at 3.175 mm while the inlet

mass flowrates are varied by regulating the tank regulators. Initially the tank pressures are manually set at desired pressure. Afterwards, the test is conducted by initiating the auto-sequence controlled by DAQ system. Three test cases are presented in this dissertation study, Table 10. The chamber pressures for these cases are 7.5 bar-g, 10 bar-g and 12.5 bar-g. The corresponding line pressures, inlet pressures and mass flowrates are also shown in Table 10. The primary difference between the feed pressure and inlet pressure is that the feed pressure represents the initial pressure of the methane and oxygen line before the main burner is turned ON. On the other hand, the inlet pressure represents the line pressure when the chamber is pressurized.

Table 10 Test cases

		Case 1	Case 2	Case 3
Chamber Pressure (bar-g/ psi-g)		7.5/ 108	10/ 145	12.5/182
Feed Pressure (bar-g/ psi-g)	Methane	13.3/ 193	15.8/ 229	18.5/ 270
	Oxygen	9.9/144	12.6/ 183	16.9/ 245
Inlet Pressure (bar-g/ psi-g)	Methane	12.9/ 188	14.6/ 212	17.6/ 255
	Oxygen	7.7/ 112	10.1/ 146	13.9/ 200
Mass Flowrate (kg/s)	Methane	0.00345	0.00383	0.00440
	Oxygen	0.009398	0.01192	0.01718

Figure 30 represents pressure profile with respect to time for case 1. For the first case the chamber pressure is 7.5 bar-g. The methane and oxygen feed pressures are set 13.3 bar-g and 9.9 bar-g respectively at the beginning of the test. Although the feed pressures are manually set before the test the line pressure decreases during the main burner operation. The inlet pressure during the test depends on the chamber pressure. It can be seen from Figure 30 that even though the methane and oxygen line pressure are set to be 13.3 bar-g and 9.9 bar-g respectively; the line pressure decreases to 12.9 bar-g and 7.7 bar-g during the main burner operation. Another vital factor during the test is the ignition of the igniter and the main burner. It is found that if there is an ignition delay during igniter ignition then detonation occur. Similar phenomenon is observed for main burner

ignition. Detonation occur due to the ignition delay of the main burner. Therefore, the igniter operating conditions are iteratively selected through experimentation to prevent the detonation. It is found that igniters perform better at fuel lean and near stoichiometric conditions. Although during the first case the igniter is operated at fuel rich condition and no detonation occur. It can be seen from Figure 30 that there is no sudden pressure hike during the igniter and main burner ignition. That means there is no detonation during the test. It is mentioned earlier that the maximum test duration is 34s. This includes 4s of igniter operation and 30s of main burner operation. It can be seen from Figure 30 that the chamber pressure reaches up to 1.7 bar-g as soon as the igniter is ignited. After 2s the main burner is turned ON. There is 2s overlaps of the igniter and the main burner. After the ignition of main burner, the chamber pressure reaches to 6.2 bar-g within 2s.

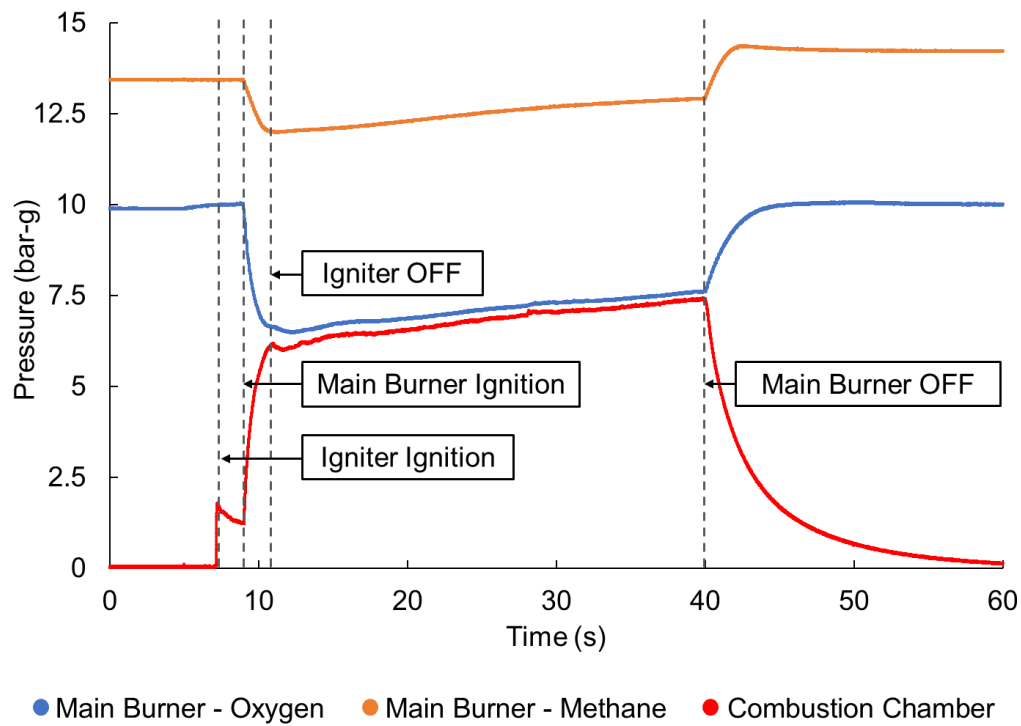


Figure 30 Pressure profile with respect to time-case 1

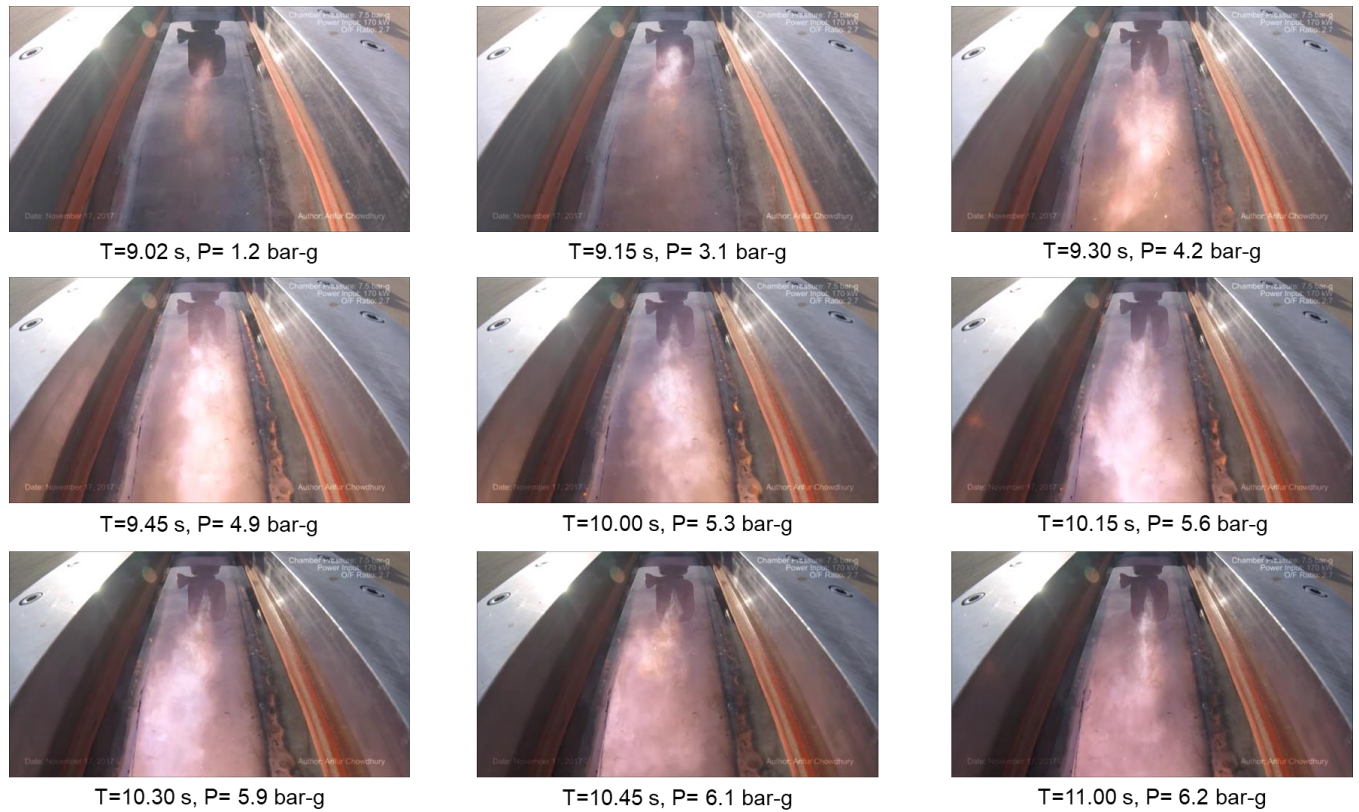


Figure 31 Main burner ignition-case 1

During this time the igniter is turned OFF. After that the main burner is operated for 28s and the chamber pressure is increased by 1.3 bar-g. The final chamber pressure is 7.5 bar-g. Figure 2 and 3 shows the flame images during main burner ignition and flame images at different time during the test for case 1, respectively. Flame images are captured only for case 1. The quartz window cannot withstand to high pressure and high temperature environment. Therefore, it is not possible to capture flame images for case 2 and 3. The main burner ignition images are captured at 0.25s rate for 2s from 9s to 11s. Figure 31 and 32 demonstrate flame images at different time frame. It is observed that although the flame is turbulent during the test, the chamber pressure does not oscillate, Figure 30. Therefore, it can be summarized that although the flame is turbulent it does not impact on the overall chamber pressure.

Figure 33 demonstrate the flowrates during the test. Main burner oxygen, main burner methane, igniter oxygen and igniter methane flowrates are plotted to understand flow behavior and

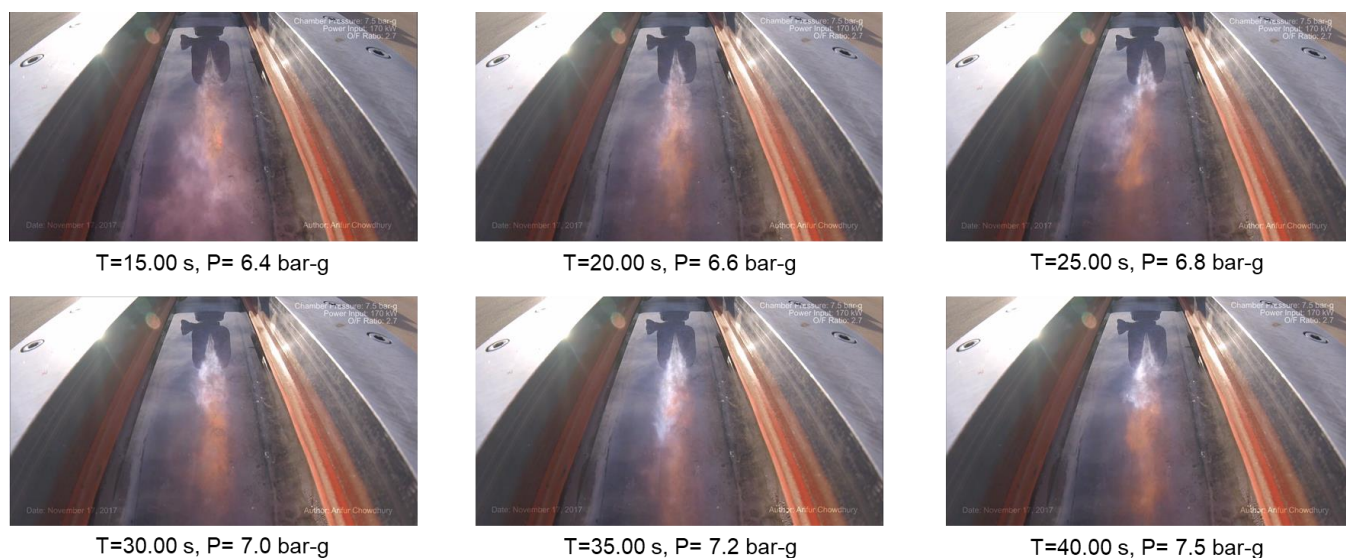


Figure 32 Flame images at different time frame during the test- case 1

power inputs for case 1. It is mentioned earlier that the flowrates are manipulated by setting the inlet pressure at the gas tank regulators. The final flowrates during the tests are dictated by the pressure differential between the feed line pressure and the chamber pressure. Once the auto sequence is initiated and final solenoid valves are opened the flowrates spikes until the chamber is pressurized. Afterwards the flowrates are settled when the chamber pressure stabilizes. At the end of the test the moment the final solenoid valves are closed the feed line pressure gets back to its initial pressure. It can be seen from Figure 4 that methane flow raises up to 404 SLPM as soon as the final solenoid valve (F-SV-3) is open. Afterwards the flowrates stabilize to 306 SLPM as soon as the chamber is pressurized. Similar trend can be seen for oxygen flowrates. Oxygen flow raises to 1200 SLPM when the final solenoid valve (O-SV-3) is opened. Afterwards when the chamber is pressurized the oxygen flowrate decreases and oscillates between 524 and 428 SLPM. This could be due to the gas tank regulators. The firing input and O/F ratio is calculated from the flowrate. It is found the firing input for this case is 170 kW and the O/F ratio is 2.72. Therefore, it can be said the test is performed at fuel rich condition. The exhaust gas compositions at equilibrium condition for case 1 are evaluated using Chemkin Pro software package, Figure 34. GRIMECH 3.0 is used as the reaction mechanism. It can be seen from the plot that the exhaust gas is mostly composed

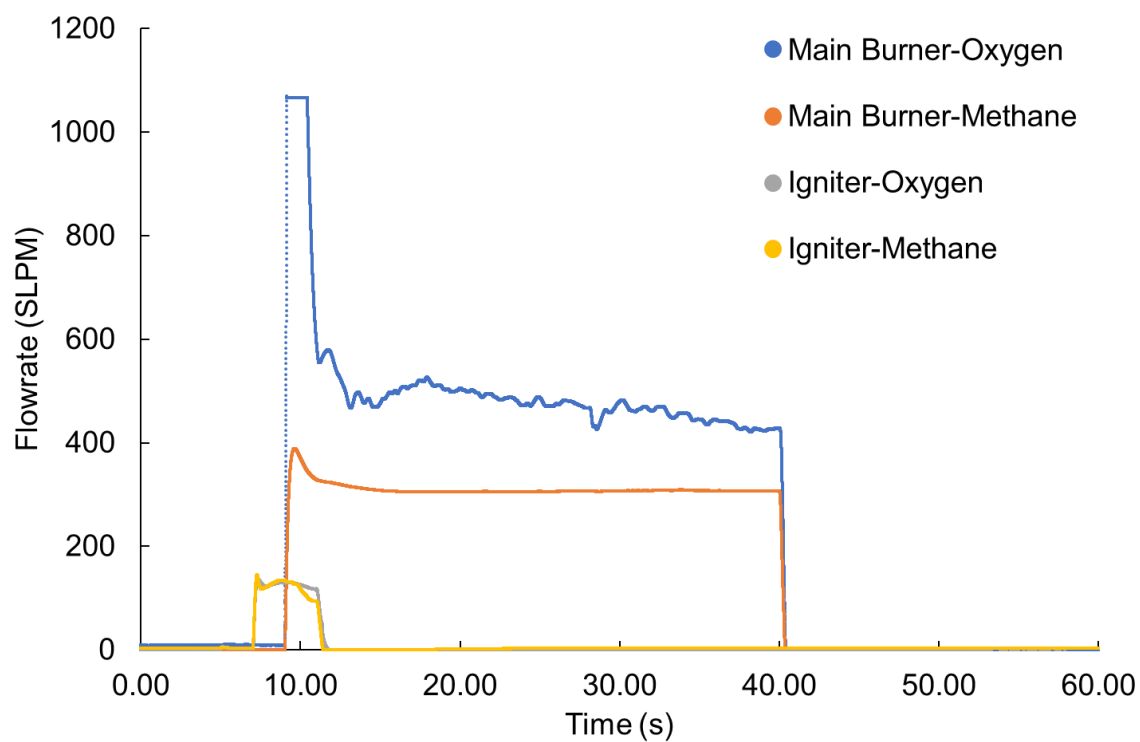


Figure 33 Volumetric flowrates with respect to time- case 1

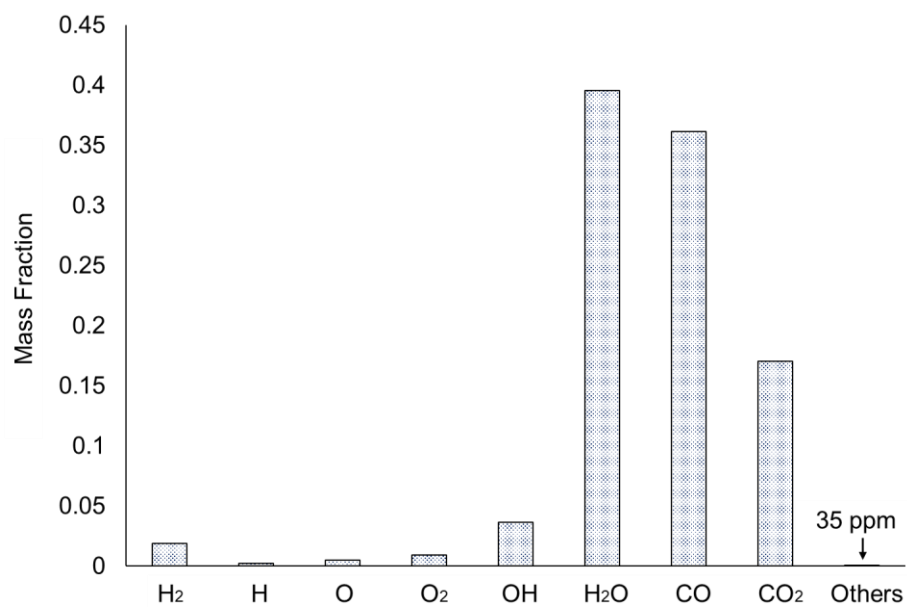
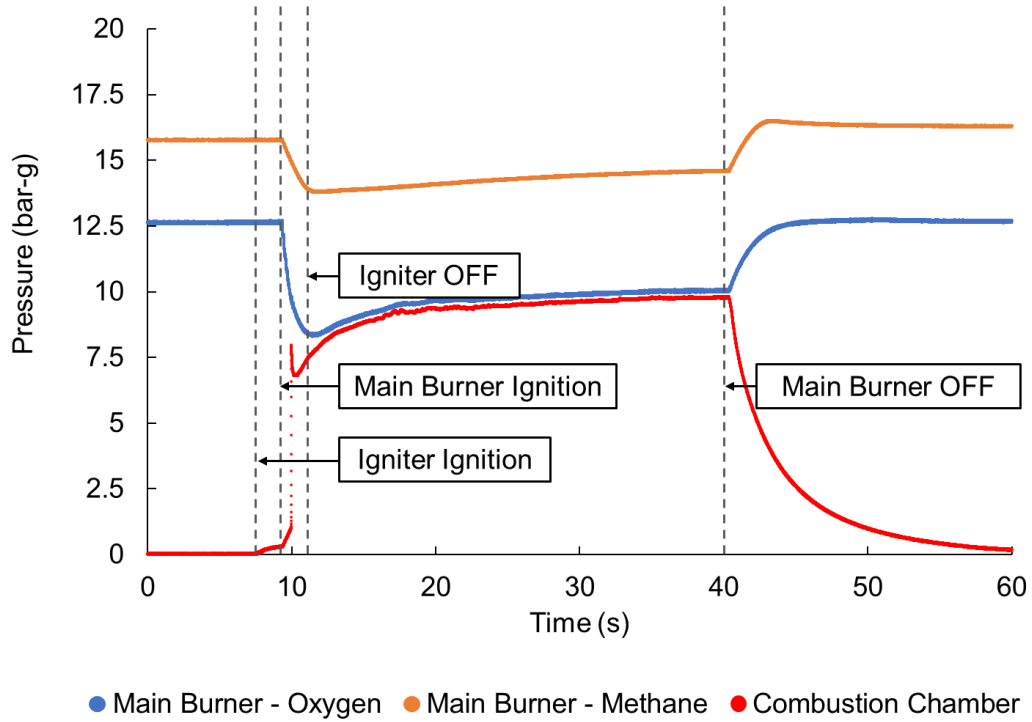


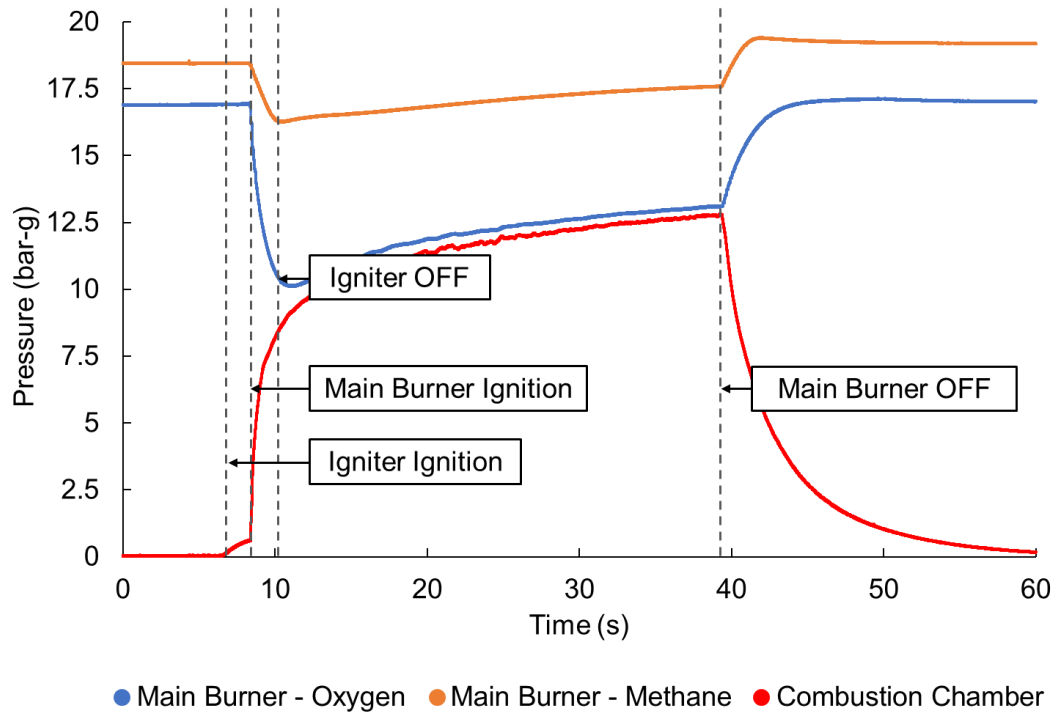
Figure 34 Exhaust gas composition at equilibrium condition- case 1

of water vapor (H_2O), carbon mono oxide (CO) and carbon dioxide. The yellow-ish color at the tail of the flame observed in Figure 32 is mostly due to the soot formation which can be seen from the exhaust gas composition [46]. Beltrame et al. [46] performed a study on soot formation in methane–oxygen enriched diffusion flames using counter blow burner. The author concluded the yellow zone at the oxy-methane combustion occur due to the soot radiation [46].

Figure 35 (a-b) represents the pressure curve with respect to time for case 2 and 3. Both of these cases displays similar trend as case 1. For the second case the chamber pressure is 10 bar-g while the methane and oxygen feed pressures are 15.8 bar-g and 12.6 bar-g, respectively, Figure 35(a). The figure demonstrates that the chamber pressure reaches up to 0.3 bar-g as soon as the igniter is ignited. The main burner is turned ON after 2s of igniter ignition. There is 2s overlaps of the igniter and the main burner.



(a)

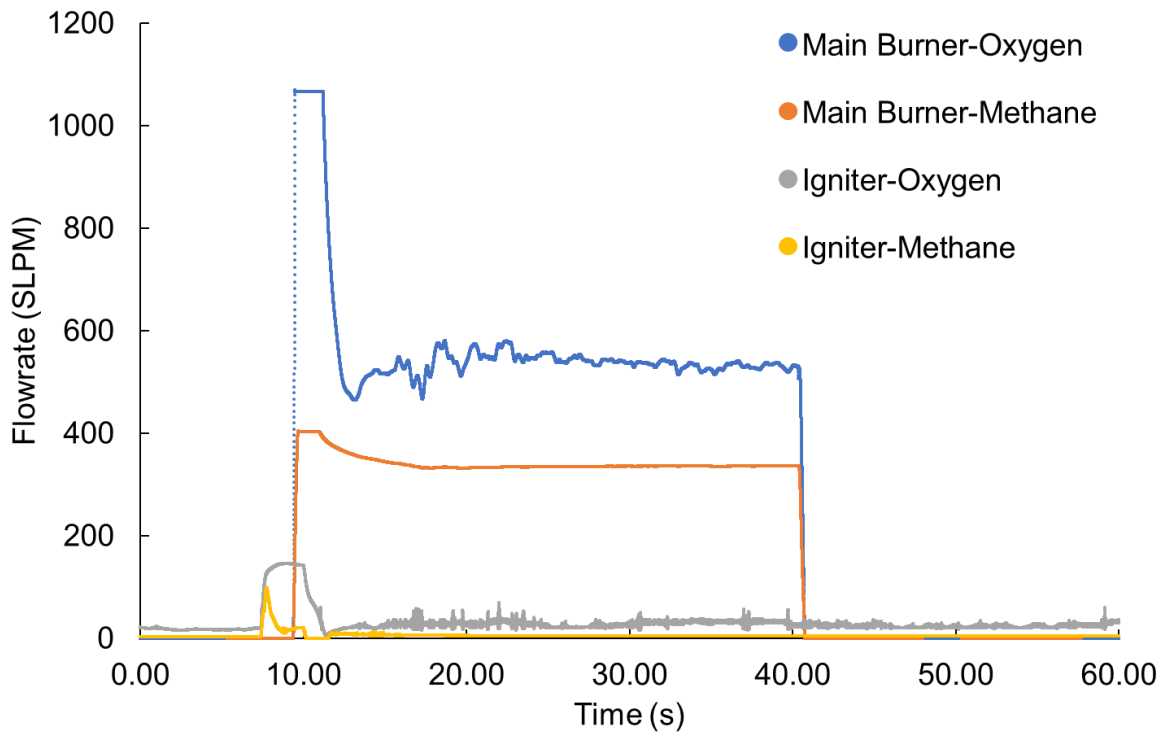


(b)

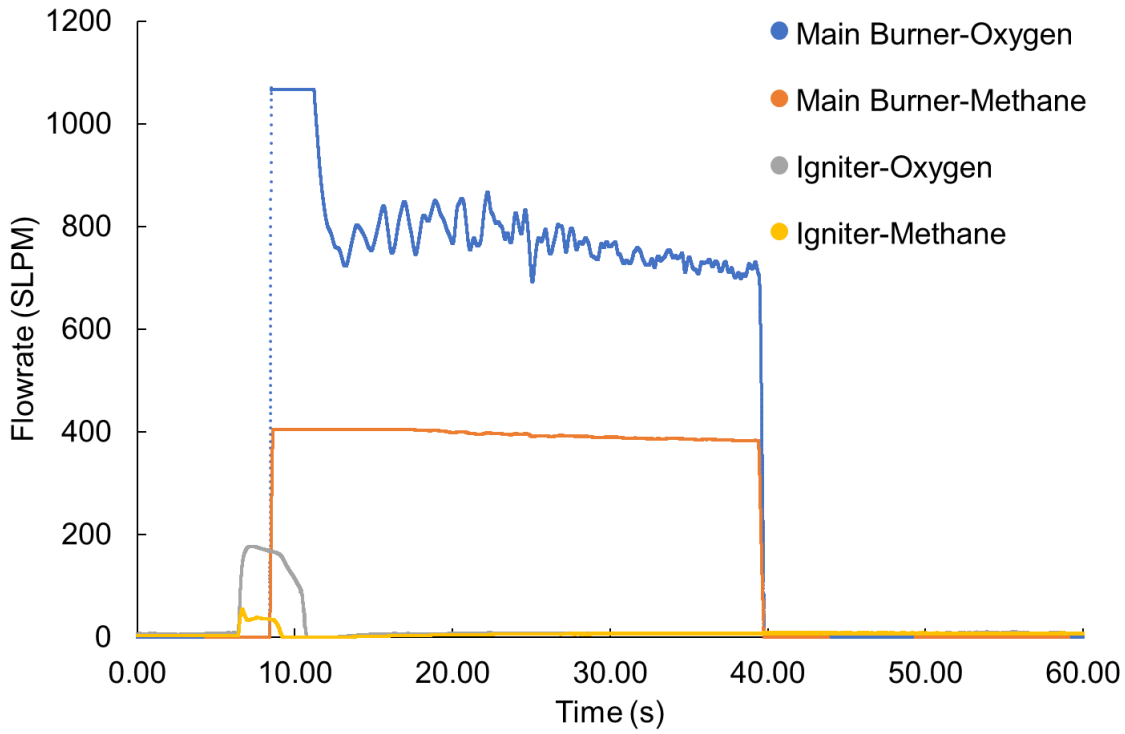
Figure 35 Pressure profile with respect to time - (a) case 2, (b) case 3

After the ignition of main burner, the chamber pressure reaches to 8 bar-g within 2s. At the same time the igniter is turned OFF and chamber pressure decreases to 6.8 bar-g. This decrement of the chamber pressure occurs due to the decrement of mass flow from the igniter. After that the main burner is operated for 28s and the chamber pressure increased by 3.2 bar-g. The final chamber pressure is 10 bar-g. For the third case the chamber pressure of 12 bar-g is obtained for methane feed pressure of 18.5 bar-g and oxygen feed pressure of 16.9 bar-g. It can be observed from Figure 35(b) that the chamber pressure reaches approximant 1 bar-g as soon as the igniter is ignited. After 2s of igniter ignition the main burner is turned ON. Similar to other two cases there is 2s overlaps of the igniter and the main burner. After the ignition of main burner, the chamber pressure reaches to 9.2 bar-g within 2s. The igniter is turned OFF after 4s of its operation. After that the main burner is operated for 28s and the chamber pressure increased by 3.7 bar-g. The final chamber for case 3 is 12.5 bar-g.

Figure 36(a-b) displays the volumetric flowrates during the test for case 2 and 3. It is mentioned earlier that the final flowrates during the tests are dictated by the feed line pressure and the chamber pressure. Figure 36(a-b) shows similar trend as case 1. The flowrates spike as soon as the final solenoid (F-SV-3 and O-SV-3) valves are opened and stabilizes when the chamber pressure stabilizes. It can be seen from Figure 36(a) that methane flow raises up to 404 SLPM as soon as the final solenoid valve is open. This number is the maximum flowrate can be read by the flowmeter. Afterwards the flowrates stabilize to 337 SLPM as soon as the chamber is pressurized. Similar trend can be seen for oxygen flowrates. Oxygen flow raises to 1200 SLPM when the final solenoid valve is opened. Afterwards when the chamber is pressurized the oxygen flowrate decreases and oscillates between 574 and 433 SLPM. Figure 36(b) shows that the methane flowrate goes up to 404 SLPM as soon as the final solenoid valve is open. Afterwards the flowrates stabilize



(a)



(b)

Figure 36 Volumetric flowrates with respect to time - (a) case 2, (b) case 3

to 383 SLPM as soon as the chamber is pressurized. Oxygen flow raises to 1200 SLPM when the final solenoid valve is opened. Afterwards when the chamber is pressurized the oxygen flowrate decreases and oscillates between 867 and 728 SLPM. The volumetric flowrates obtained from the experiments are used to calculate firing inputs and O/F ratios for case 2 and case 3. The firing inputs for case 2 and 3 are 190 kW and 220 kW, respectively. The O/F ratios for case 2 and case 3 are 3.1 and 3.9, respectively.

4.2 CFD Analysis

An attempt is made to replicate the test conditions using ANSYS Fluent CFD tool. The numerical simulation methodology is explained in chapter 2. Due to academic license limitations the total mesh elements are limited to 500,000. Furthermore, the simulation is conducted in 2D domain instead of 3D domain to reduce the computation time and to achieve better accuracy

considering the mesh element limitations. The pressure-based solver is used to simulate the fluid flow. While using the pressure-based solver the velocity field is obtained by solving a pressure (or pressure correction) equation. The pressure equation is evaluated from the continuity and the momentum equations in such a way that the velocity field, modified by the pressure, satisfies the continuity. Since the governing equations are nonlinear and coupled to one another, the solution process involves iterations in which the complete set of governing equations is evaluated recurrently until the solution converges. Fluent has three different inlet conditions which can be used to simulate fluid flow problems: (i) velocity inlet, (ii) pressure inlet and (iii) mass flow inlet. The velocity inlet boundary conditions are used to define the velocity and scalar properties of the flow at the inlet. The pressure inlet boundary conditions are used to state the total pressure and other scalar quantities at the inlet. Mass flow inlet boundary conditions are used in compressible flows to define a mass flow rate at the inlet. However, it is not necessary to use mass flow inlets in incompressible flows. The velocity inlet boundary conditions evaluate the mass flow since the density is constant and inlet area is fixed. For this particular analysis mass flowrate boundary conditions are used. In this way the power inputs for individual CFD cases can be precisely set. The detailed conditions are explained in Table x. The mass flowrate inlet boundary condition requires the input of mass flowrate, flow direction, thermal condition and mixture fraction at the boundary. For this particular case the flow is normal to the boundary. The fuel and oxidizer are injected at 295 K. Furthermore, Fluent requires specification of transported turbulence quantities at the inlet. k- ϵ turbulence model is used to incorporate fluid flow turbulence in the CFD model. This requires the input of turbulent intensity and hydraulic diameter at the inlet. The turbulence intensity is defined as the ratio of the root-mean-square of the velocity fluctuations to the mean flow velocity. If the turbulence intensity is 1% or less then the flow is considered less turbulent whereas if the turbulence intensity is greater than 10% then the flow is considered highly turbulent. For internal flows, the turbulence intensity at the inlets depends on the upstream flow profile. If the upstream flow is under-developed and undisturbed then the turbulence intensity will be low. On the other hand, if the flow is fully developed, the turbulence intensity may be as high as a few

percent. The turbulence intensity at the core of a fully-developed duct flow can be evaluated from the following equation which is derived from an empirical correlation for pipe flows:

$$I = 0.16 \text{Re}_{d_h}^{-1/8} \quad (17)$$

Where,

$$\text{Re} = \frac{\rho v d_h}{\mu} \quad (18)$$

For this particular analysis the turbulent intensity varies between 3.75 % to 5%.

Table 11 Fluent input parameters at the inlets

		Case 1	Case 2	Case 3
Mass Flowrate (kg/s)	Methane	0.00345	0.00383	0.00440
	Oxygen	0.00939	0.01192	0.01718
Turbulent Intensity (%)	Methane	3.87	3.82	3.75
	Oxygen	4.89	4.74	4.57
Hydraulic Diameter (m)	Methane	0.00457	0.00457	0.00457
	Oxygen	0.0047	0.0047	0.0047
Thermal Condition (K)	Methane	295	295	295
	Oxygen	295	295	295
Mean Mixture Fraction	Methane	1	1	1
	Oxygen	0	0	0

For this analysis convective heat transfer wall is used as the wall boundary condition. When the convective heat transfer boundary condition is used at a wall, Fluent uses the inputs of the external heat transfer coefficient and external heat sink temperature to compute the heat flux to the wall. Table 12 shows the detail inputs of the convective heat transfer boundary condition for three different cases:

Table 12 Fluent input parameters at the wall

	Case 1	Case 2	Case 3
Wall Thickness	0.0762	0.0762	0.0762
Free Stream Temperature (K)	300	300	300
Heat Transfer Coefficient (K-W/m ²)	22	22	22
Heat Generation Rate	0	0	0

Fluent gives the option of choosing several outlet boundary conditions for different cases. Among them outlet flow, pressure far-field and pressure outlet are commonly used. The outflow boundary conditions are used to model flow exits where the flow velocity and pressure specifications are initially unknown. This type of boundary conditions is appropriate where the exit flow is close to a fully developed condition. However, since the outflow boundary condition assumes a zero-normal gradient for all flow variables except pressure, this boundary conditions are not appropriate for compressible flow calculations. The pressure far-field boundary condition is used to model a free-stream compressible flow at infinity where the free-stream Mach number and the static conditions are defined. This type of outlet boundary condition is mostly used for compressible flows. The pressure outlet boundary condition is used to describe the static pressure at flow outlets. The employment of a pressure outlet boundary condition as opposed to an outflow outlet often results in a better rate of convergence when backflow occurs during iteration. For this particular analysis pressure outlet boundary condition is used. The simulation is performed by adding a fluid domain at the outlet section of the combustor. The outlet of the fluid domain is set to be at atmospheric pressure, Table 13. Then the exit diameter of the combustor is manipulated to achieve the pressure inside the combustor.

Table 13 Fluent input parameters at the outlet

	Case 1	Case 2	Case 3
Pressure- Gauge (bar)	0	0	0
Hydraulic Diameter (m)	0.28	0.28	0.28

As an initial point the exit diameter for each case is analytically calculated using equation 19 and CFD analysis is performed. Afterwards, the exit area is iteratively selected to achieve the chamber pressure similar to the test case. The exit area is a function of total mass flowrate, throat temperature, chamber pressure and gas properties. The total mass flowrate and chamber pressure is directly obtained from the test conditions. The temperature and gas properties from NASA CEA chemical equilibrium solver. The exit area and exit diameter from analytical solution is presented in Table 14.

$$A_t = \frac{(\dot{m} \times \sqrt{T_t})}{(P * \sqrt{(\frac{\gamma}{R}) (\frac{\gamma+1}{2})^{\frac{-\gamma+1}{2(\gamma-1)}}})} \quad (19)$$

Table 14 Exit area and exit diameter estimation from analytical solution

Analytical Estimation	Case 1	Case 2	Case 3
Exit Area (m ²)	3.21364E-05	2.91975E-05	3.08348E-05
Exit Diameter (mm)	6.40	6.10	6.27

Figure 37 demonstrate the exit diameter with respect to the chamber pressure from CFD analysis for the three cases. It is mentioned earlier that the exhaust area can be evaluated using equation x. Since mass flowrate is assigned at the beginning of the simulation and it is a steady state process ($\dot{m}_{in} = \dot{m}_{out}$), the chamber pressure during the CFD simulation depends on the temperature and the gas properties at the throat. It can be seen from the plot that the analytical solution overpredicts the exit area, Figure 37. This is due to the difference in estimating exhaust temperature and exhaust gas composition. During analytical analysis the temperature and gas properties are obtained from NASA CEA. NASA CEA provides the adiabatic flame temperature and corresponding gas properties for a given chamber pressure and O/F ratio. In reality, due to the length of the combustor, by the time combustion gas reaches to the exit nozzle, it cools down. The

gas at the exit is no longer similar to the adiabatic flame temperature. The CFD analysis simulates this reduction of temperature at the exit and evaluates the gas properties. Therefore, between the analytical solutions and the CFD estimations, the CFD estimation provides better approximation than the analytical solutions. It is observed that while doing the CFD analysis the 7.5 bar chamber pressure is obtained for 5.5 mm exit diameter which is lower than the

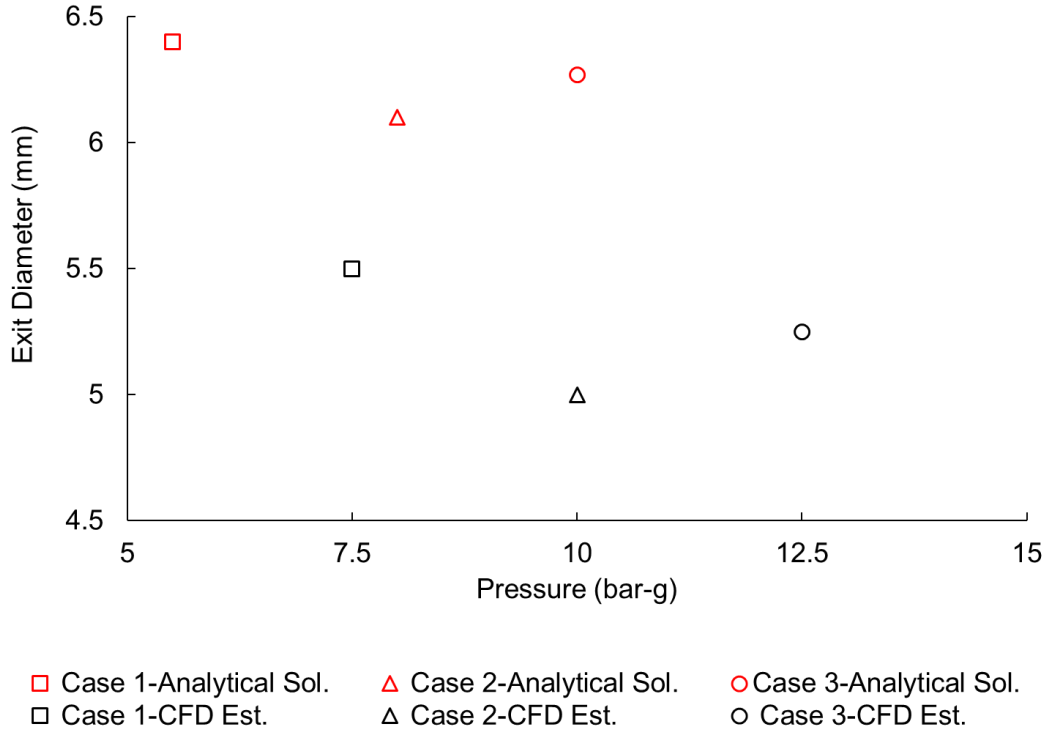


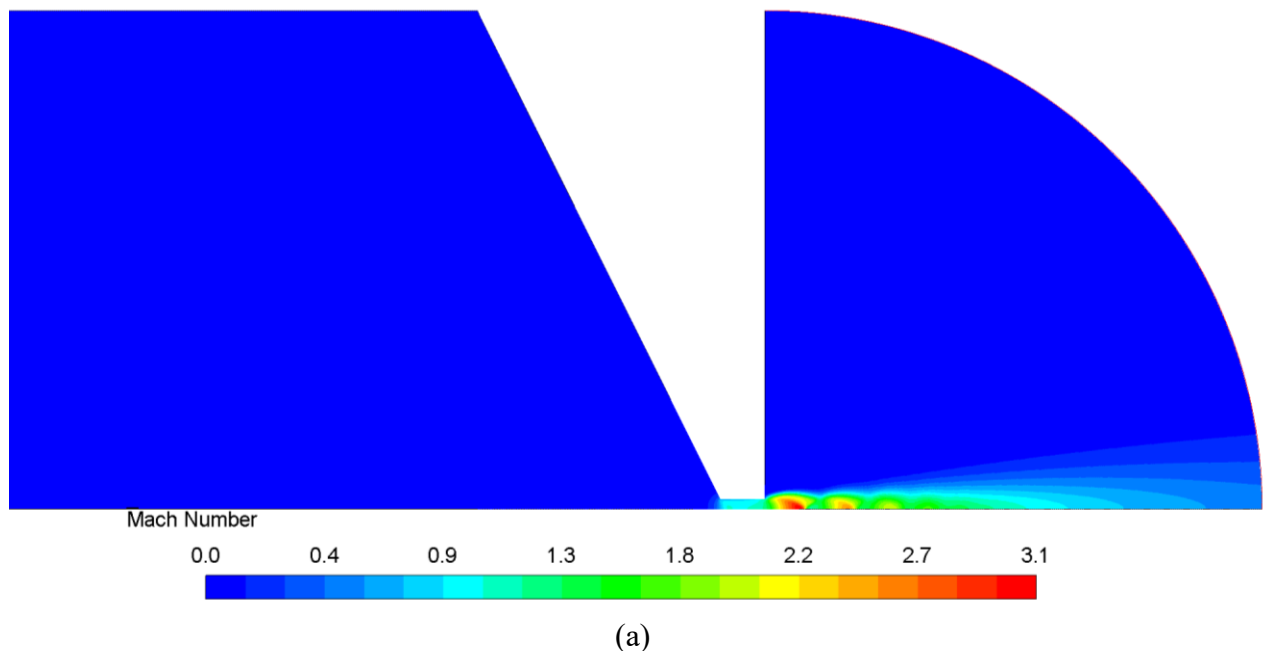
Figure 37 Exit diameter vs. chamber pressure comparison between the analytical solution and CFD estimation

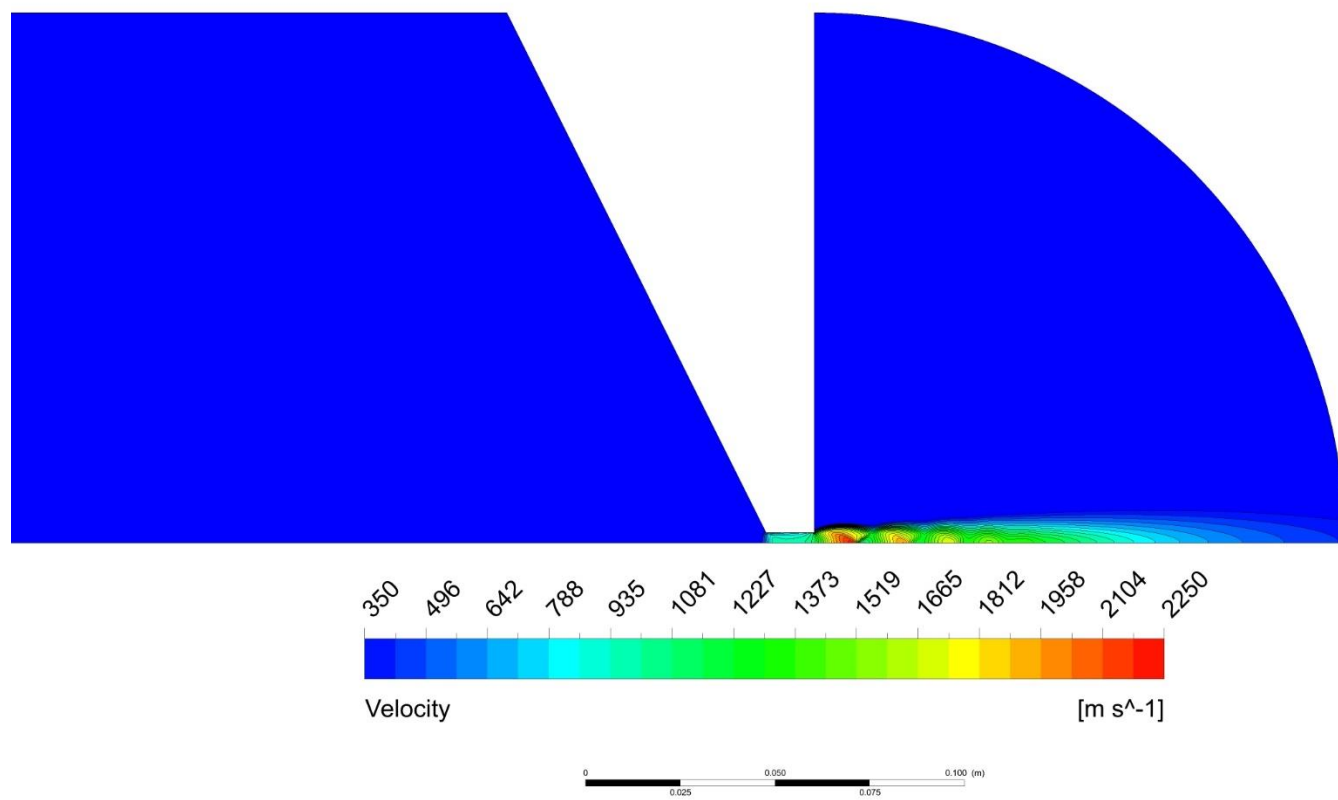
analytical estimation, 6.40 mm. The 6.40 mm exit diameter provides chamber pressure of 5.5 bar. These difference in the estimation of chamber pressure can be described by the combustion gas temperature, sonic velocity, specific heat ratio and gas constant assumption at the throat. For case 1, NASA CEA provides the adiabatic flame temperature, sonic velocity and gas constant are 3207 K, 1267 m/s, 442 J/kg-K, respectively. On the other hand, the CFD simulation provides the average temperature at the throat is 2000 K. The sonic velocity and gas constant at the throat are 938 m/s, 366 J/kg-K, respectively. Hence, the discrepancy between the analytical solution and CFD

estimation is contributed by the difference gas properties at the throat. During the actual test the 7.5 bar chamber pressure is obtained at 3.175 exit diameter for the power input of 170 kW and O/F mixture ratio of 2.72. Similar trend is observed for case 2 and case 3. For case 2, during the CFD analysis the 10 bar chamber pressure is obtained for 5.0 mm exit diameter which is lower than the analytical estimation, 6.1 mm. The 6.1 mm exit diameter provides chamber pressure of 8 bar. It is observed that during the experimental study the 10 bar chamber pressure is obtained at 3.175 mm exit diameter when the power input is 180 kW and O/F mixture ratio is 3.1. For case 3 while doing the CFD analysis the 12.5 bar chamber pressure is obtained for 5.25 mm exit diameter which is lower than the analytical estimation, 6.27 mm. The 6.27 mm exit diameter provides chamber pressure of 10 bar. While performing the test the 12.5 bar chamber pressure is gained for 3.175 mm exit diameter when the power input is 220 kW and O/F mixture ratio is 3.91. It is found that between the CFD estimation and actual test the CFD estimation over predicts the exit diameter in comparison to the actual test where gas may leak from different joints and fittings. Furthermore, during the CFD analysis the combustion product and flame temperature is evaluated using the PDF table. The integration of multistep detailed chemistry may improve the error percentage between the CFD analysis and the actual test.

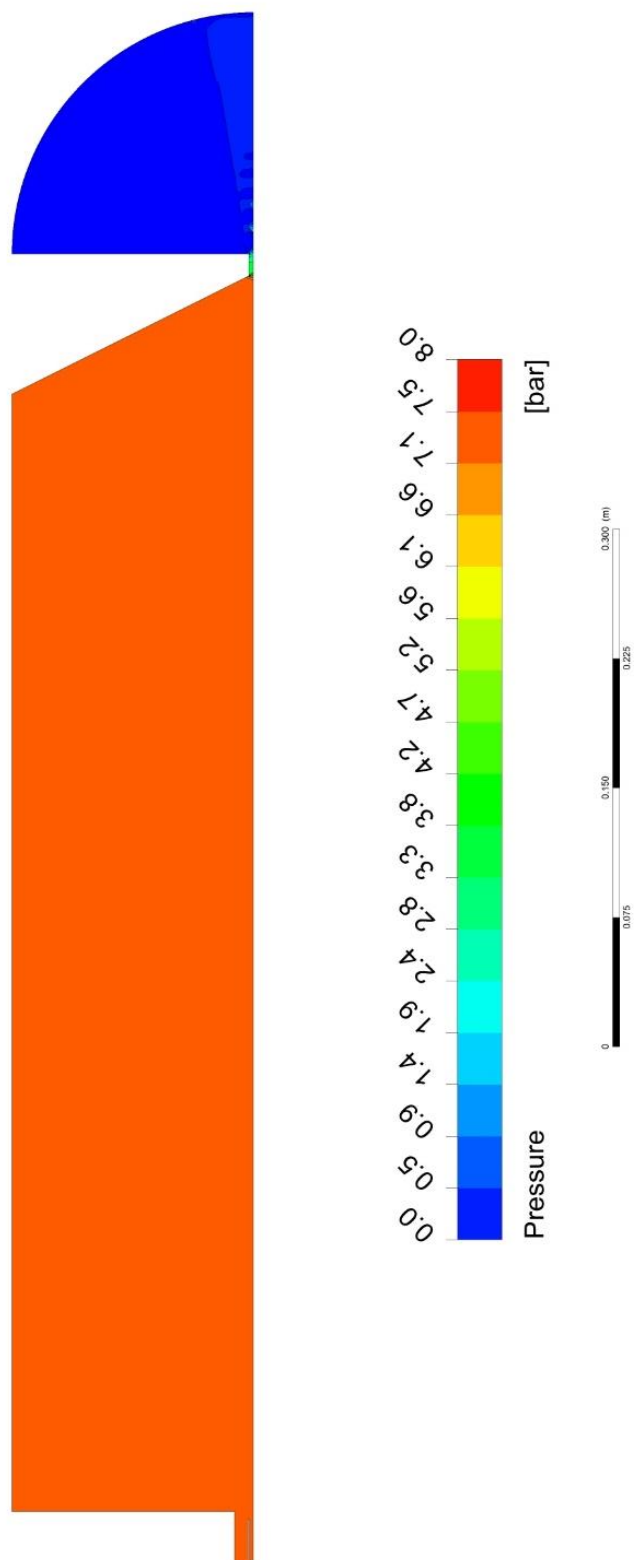
Figure 38 displays the velocity profile, pressure contour and temperature contour inside the combustor for case 1. It can be seen from the figure that the velocity reaches to Mach 1 at the exit of the combustor. Thus, the flow is choked. At this condition the pressure inside the combustor is close to 7.5 bar, Figure 38(a). During the CFD analysis, the sonic velocity and exhaust temperature obtained are 938 m/s and 2000 K, respectively. The flame inside the combustor is simulated using non-premixed combustion model. The combustion products are automatically generated using a pdf table built into the software. The temperature contours inside the combustor are shown in Figure 38(d). The maximum flame temperature calculated by Fluent is approximately 2950K while NASA CEA calculates 3300K. This discrepancy occurs mostly due to small differences in the estimated properties of the exhaust gases, which impacts the specific heat ratio and other physical properties of the system. Similar trend is observed for case 2 and case 3. Figure

39 and 40 displays the velocity profile, pressure contour and temperature contour inside the combustor for case 2 and case 3. It can be seen from Figure 39 (c) that the pressure inside the combustor is close to 10 bar. The velocity at the combustor exit can be seen in Figure 39(a-b). It can be seen from the figure that the velocity reaches to Mach 1. combustor. While performing the CFD analysis, the sonic velocity and exhaust temperature obtained are 940 m/s and 2040 K at exit at the nozzle exit, respectively. The temperature contours inside the combustor are shown in Figure 39(d). The maximum flame temperature calculated by Fluent is approximately 3000 K. Figure 40(c) displays the pressure contour inside the

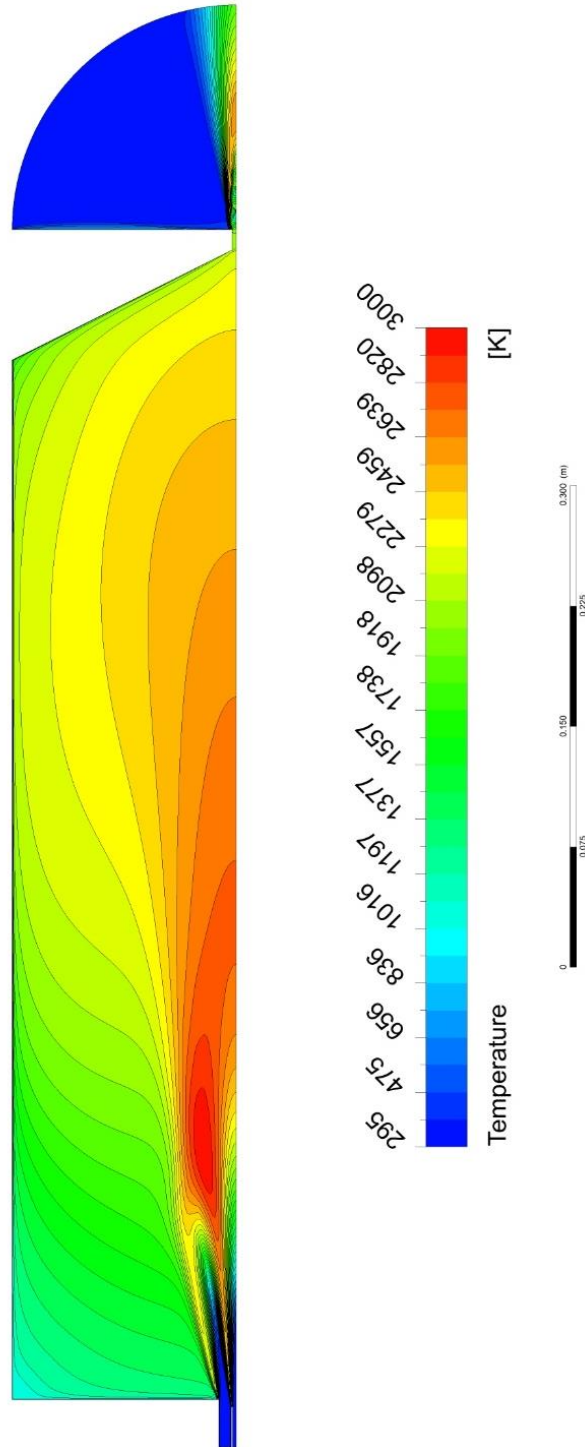




(b)

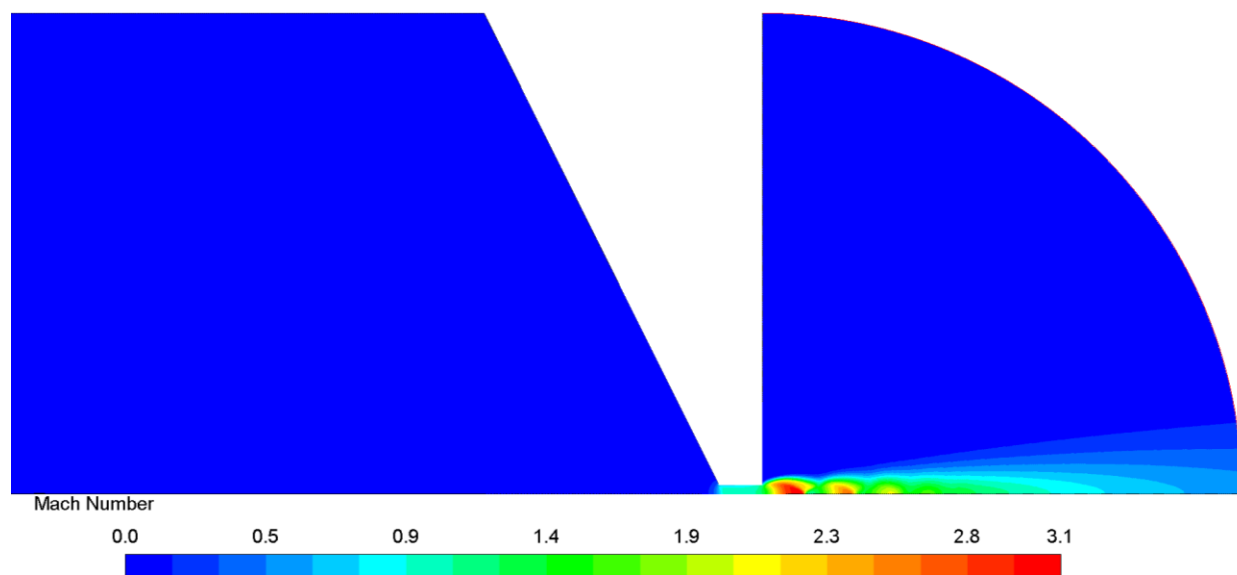


(c)

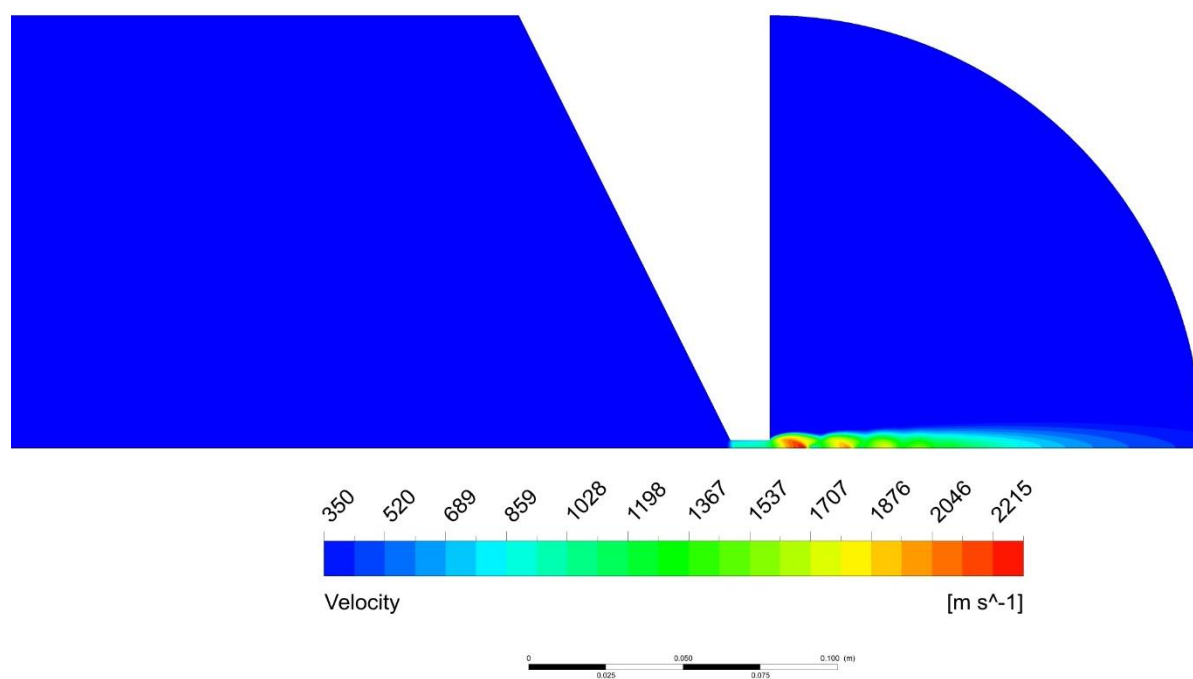


(d)

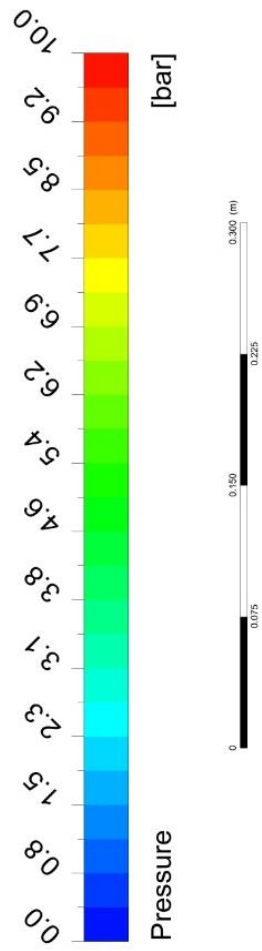
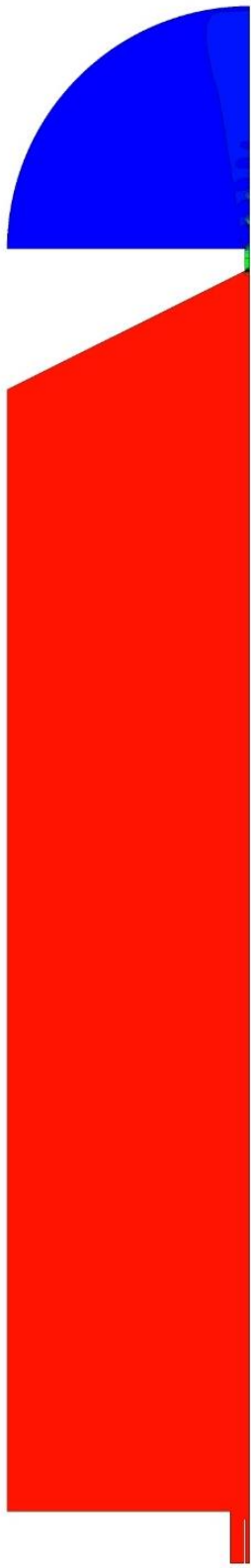
Figure 38 CFD results for case 1 (a) Mach number at the exit, (b) velocity number at the exit, (c) pressure contour inside the combustor and (d) temperature contour inside the combustor



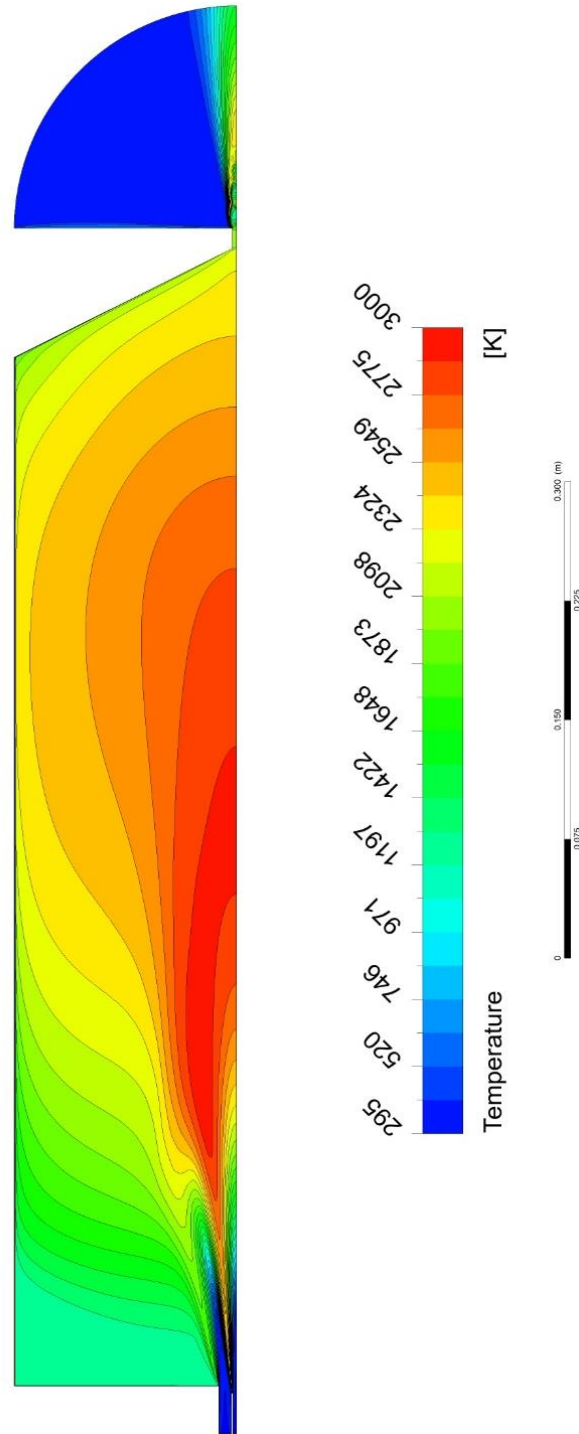
(a)



(b)

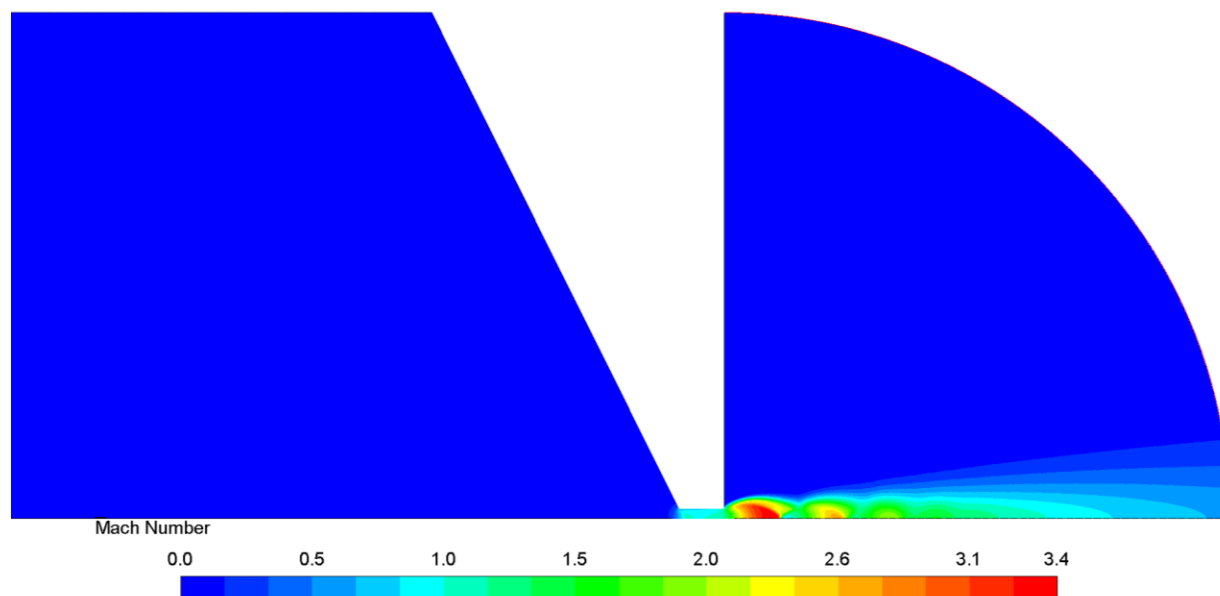


(c)

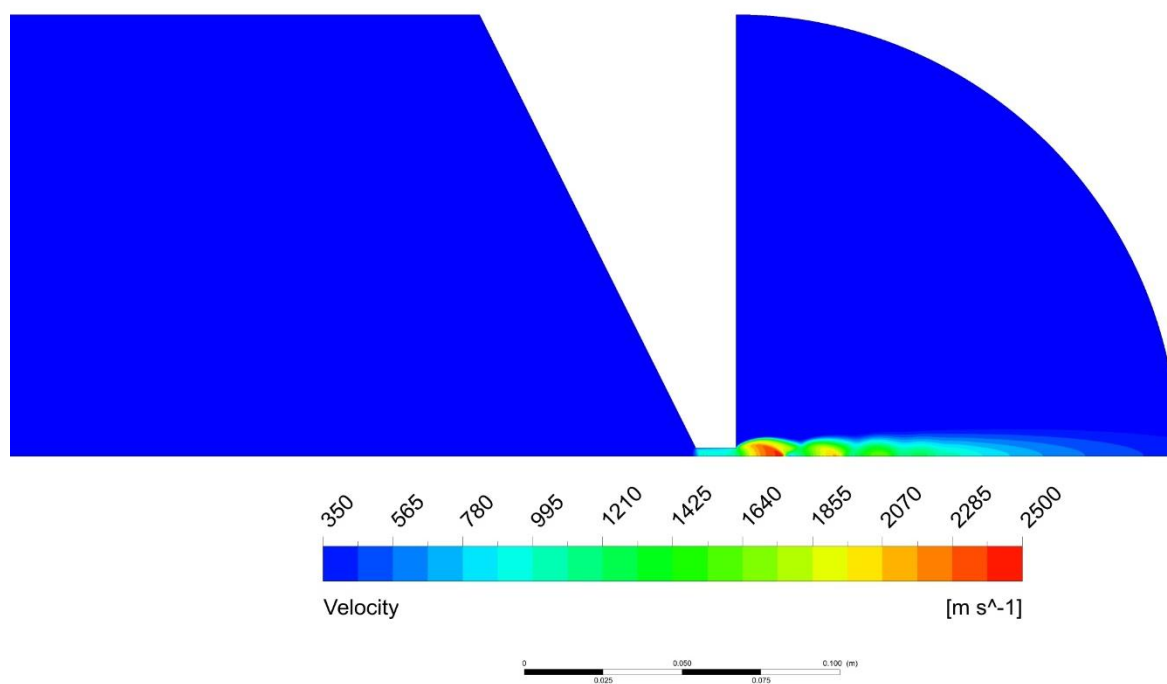


(d)

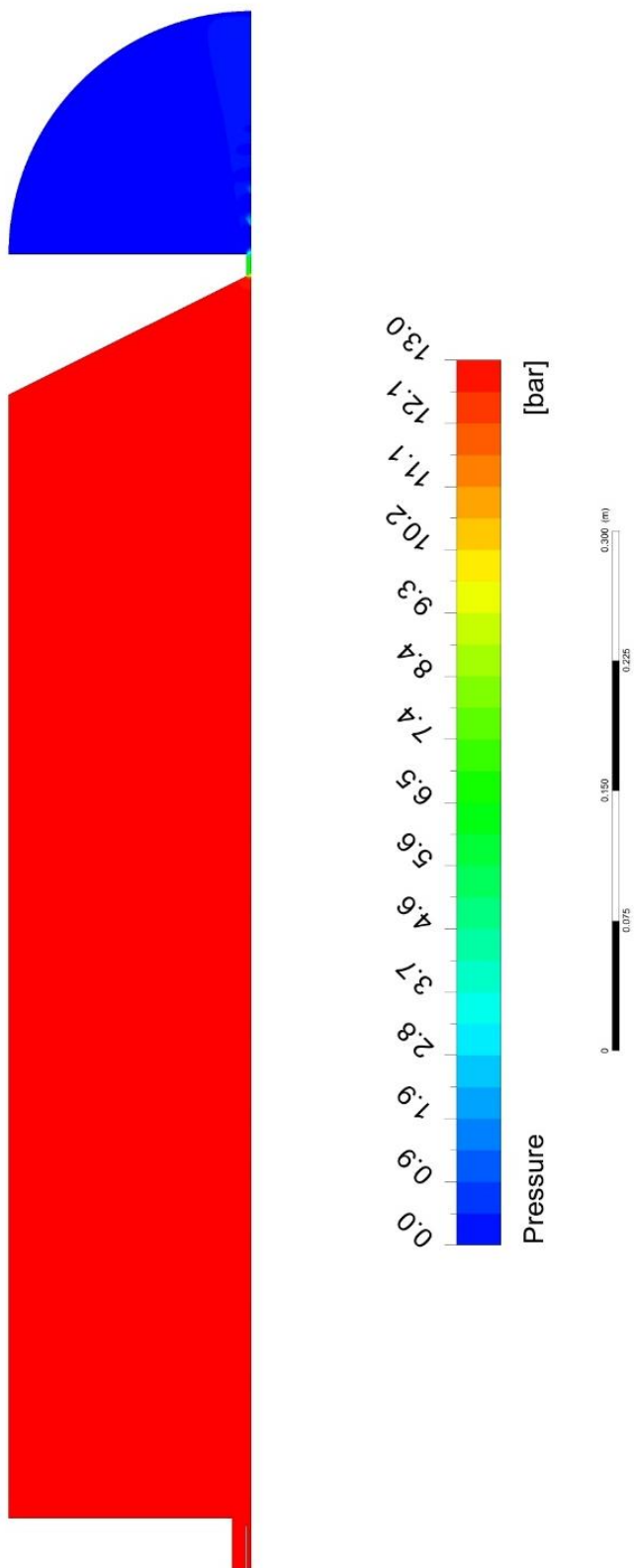
Figure 39 CFD results for case 2 (a) Mach number at the exit, (b) velocity number at the exit, (c) pressure contour inside the combustor and (d) temperature contour inside the combustor



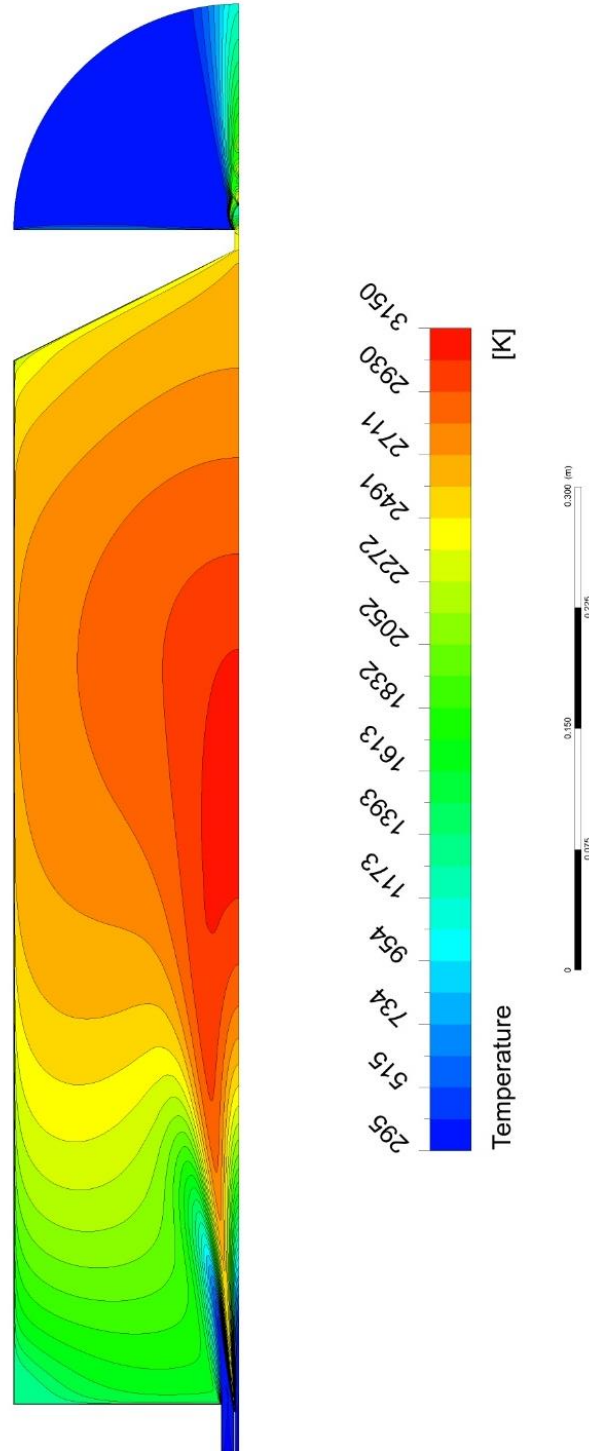
(a)



(b)



(c)



(d)

Figure 40 CFD results for case 3 (a) Mach number at the exit, (b) velocity number at the exit, (c) pressure contour inside the combustor and (d) temperature contour inside the combustor

combustor for case 3. It can be seen from Figure 40(c) that the pressure inside the combustor is close to 12.5 bar. The velocity at the combustor exit can be seen in Figure 40(a-b). It can be seen from the figure that the velocity reaches to Mach 1. During the CFD analysis, the sonic velocity and exhaust temperature obtained are 950 m/s and 2400 K at the nozzle exit, respectively. The temperature contours inside the combustor are shown in Figure 41. The maximum flame temperature calculated by Fluent is approximately 3100 K. One of the primary objective of this dissertation study is to develop a steady state high pressure combustor development. The CFD analysis provides a better understanding about the near wall temperature profile at steady state condition. Figure 41 represent the near wall temperature profile from the CFD analysis for all three cases at the test condition. The temperature profile is obtained at 1 mm below the wall. It can be seen that the combustor wall temperature gradually increases towards the end of the combustor and passes the material operation range when it operates at steady state condition for all three cases. The melting point of SS 410 is 1800 K and maximum operational temperature is 935 K. Therefore, the combustor requires cooling system for continuous operation.

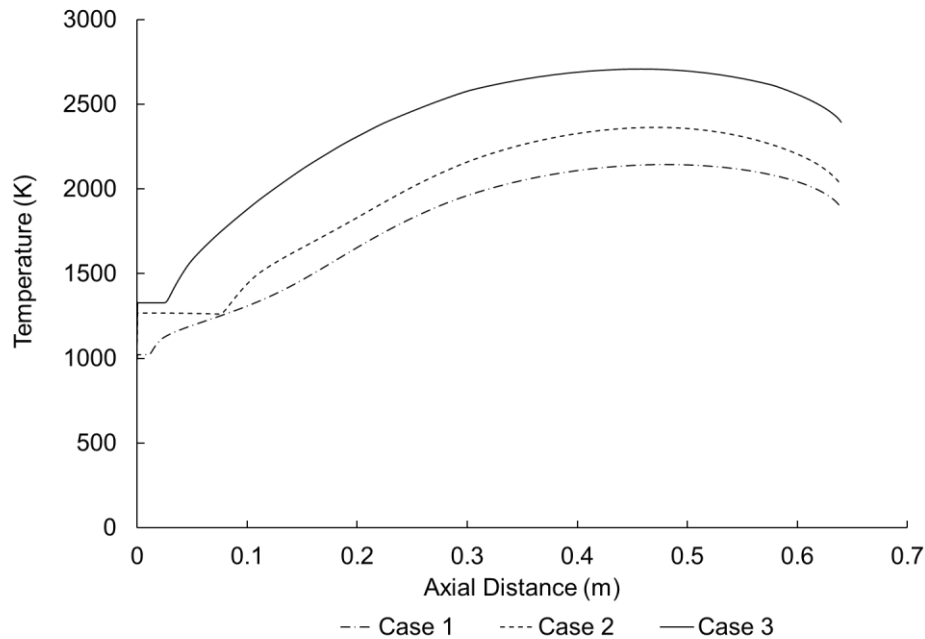


Figure 41 Temperature profile near the wall (R= 0.138 m)

4.3 Combustor Cooling System

The existing combustor is made out of Stainless Steel-410 [3]. The material allowable temperature is obtained by a thermo-mechanical analysis that considers the material's properties and their changes with temperature. Since the high-pressure combustor is a cylindrical vessel and it will be operated up to 20 bar pressure, the analysis is performed using the pressure vessel model. The assumptions that are considered to obtain the total stresses are:

- The pressure inside the combustor is uniform and positive
- The combustor is a thick-walled cylinder
- The material throughout the combustor is homogeneous
- The geometry and the loadings are symmetrical

Figure 42 shows the schematic of a pressure vessel and the direction of all the stresses in front and side view.

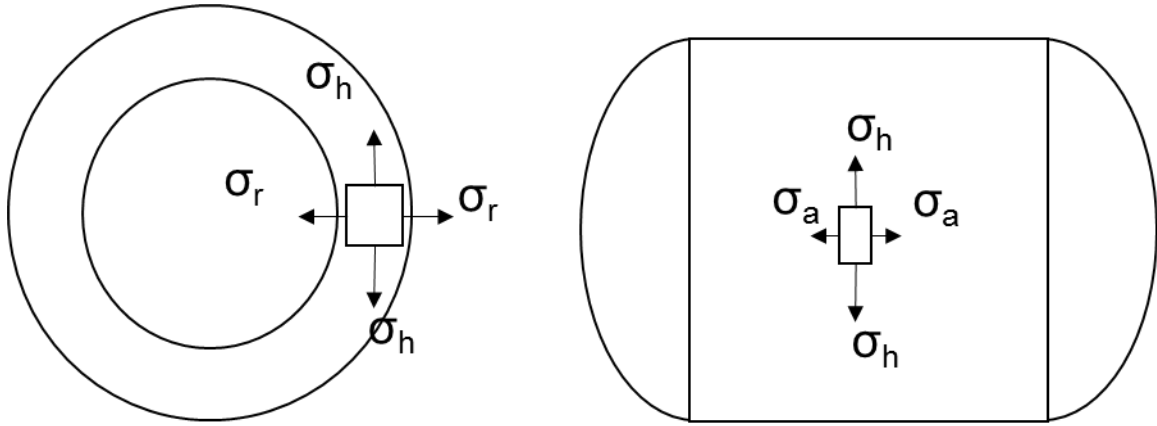


Figure 42 Schematic of a pressure vessel and the direction of all the stresses in front and side view

For thick walled the hoop stress can be evaluated using following formula:

$$\sigma_h = \frac{r_i^2 P_i - r_o^2 P_o}{(r_o^2 - r_i^2)} + \frac{(P_i - P_o) r_i^2 r_o^2}{(r_o^2 - r_i^2) r_i^2} \quad (20)$$

The combustor has an inner radius of 0.14 m and an outer radius of 0.23 m. While performing the analysis the combustion chamber pressure is assumed to be 20 bar (2 MPa) and the

outer pressure is taken to be the atmospheric pressure. The hoop stress in the combustor is calculated to be 4 MPa (40 bar) based on Equation 20. The thermal stress is calculated in the combustor with Equation 21:

$$\sigma = \frac{E\alpha qt}{2(1-\nu)k} \quad (21)$$

Where, E is Young's Modulus, α is the coefficient of thermal expansion, q is the heat flux, t is the thickness, ν is Poisson's ratio of the material and the k is the thermal conductivity. The basic conduction equation for heat flux is:

$$q = \frac{k(T_{wg} - T_{wair})}{t} \quad (22)$$

By substituting Equation. 22 into Equation. 21, the resulting thermal stress equation becomes:

$$\sigma_t = \frac{E\alpha(T_{wg} - T_{wair})}{2(1-\nu)} \quad (23)$$

The maximum operating temperature of the SS 410 is 975 K. However, Young's Modulus is a temperature dependent mechanical property and decreases with an increasing operating temperature. From the available data the highest temperature for which the mechanical properties of SS 410 could be obtained is 825 K, Figure 43. With existing data, an extrapolation is performed, using a 3rd order polynomial equation.

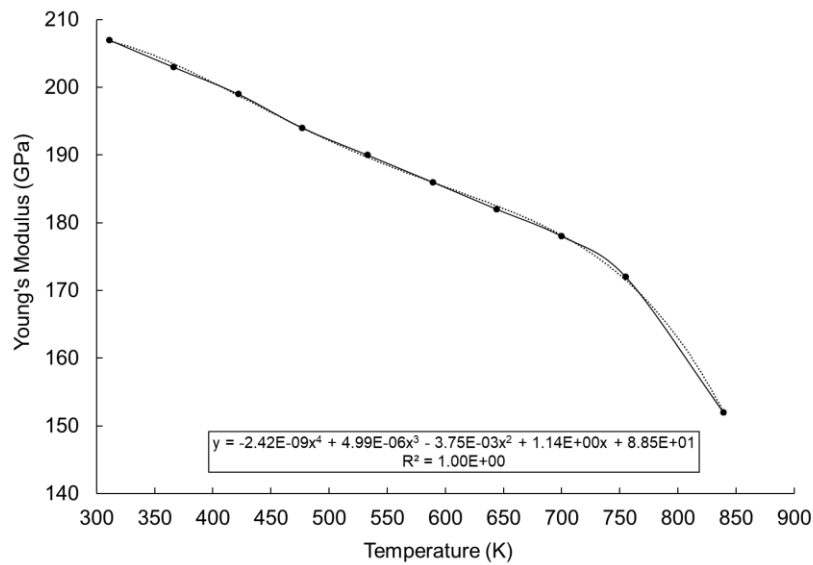


Figure 43 Young's Modulus of SS410 for a range of temperatures

The thermal stress is calculated to be 395 MPa (3950 bar). Using the extrapolated value of the material yield strength at 975 K, it is found that it is 250 MPa (2500 bar). Thus, without any cooling at these conditions failure will occur as the expected stresses are larger than the maximum yield strength of the material. Since both the expected thermal stresses and material yield strength are temperature dependent it is useful to compare these properties, Figure 44. From Figure 44, it is observed that failure is expected to occur at 725 K. A safety factor of 1.4 was chosen, corresponding to an allowable operating temperature of 600 K. This is the maximum temperature that must be reached at the inner wall of the combustor with the cooling system. To meet these requirements, the proposed cooling solution must keep the combustor inner chamber walls at a maximum allowable temperature of 600 K.

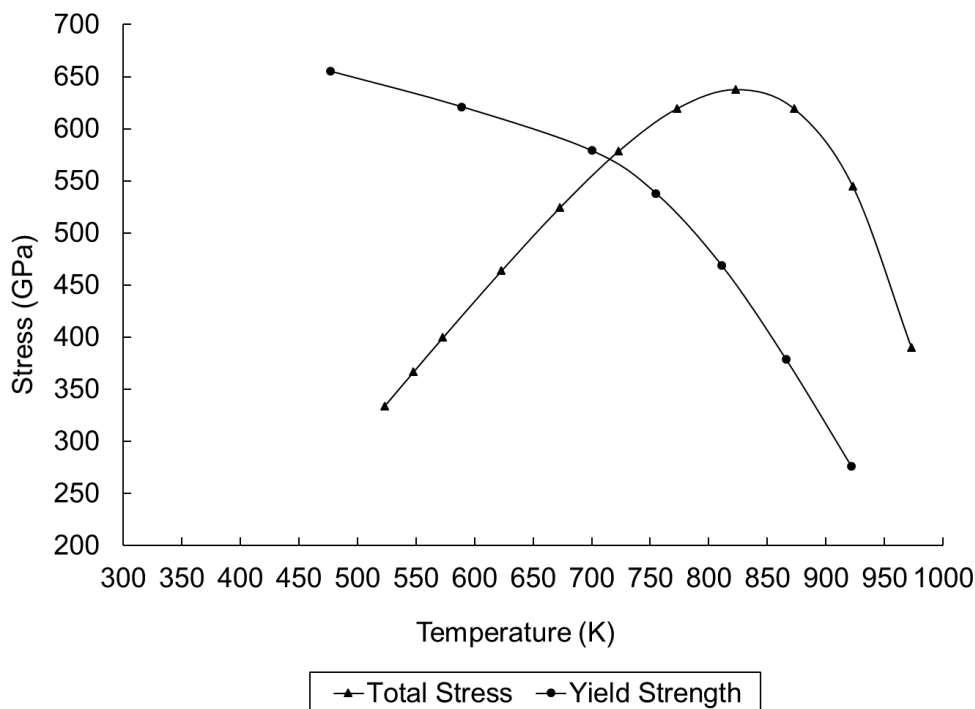
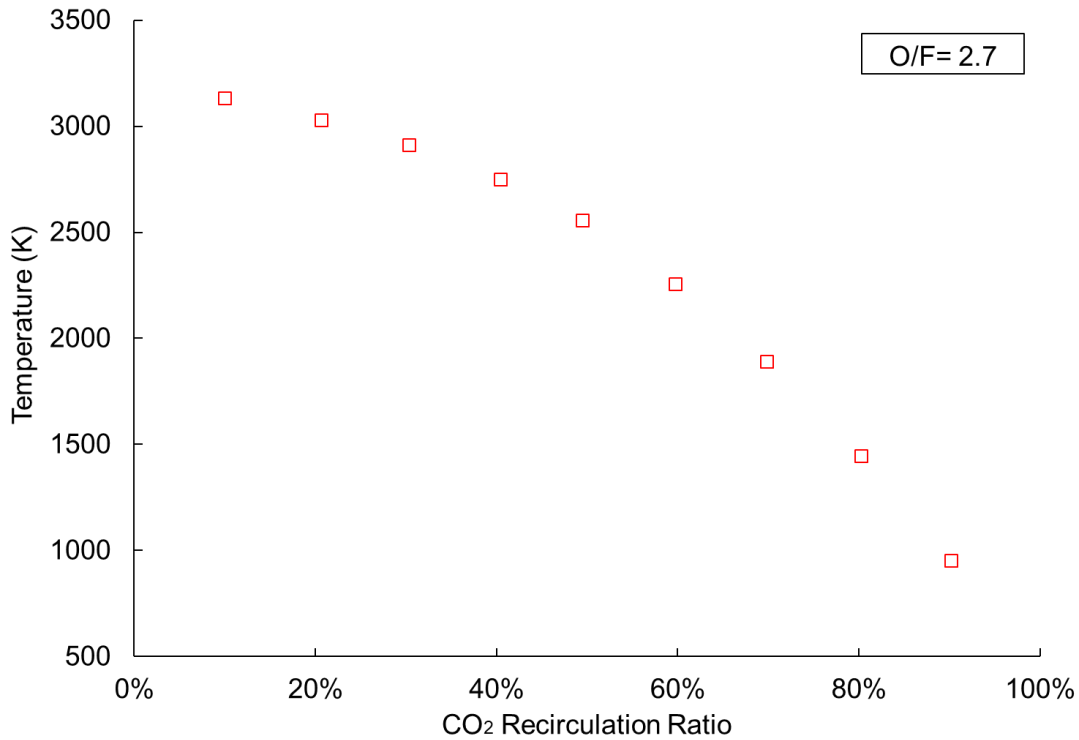


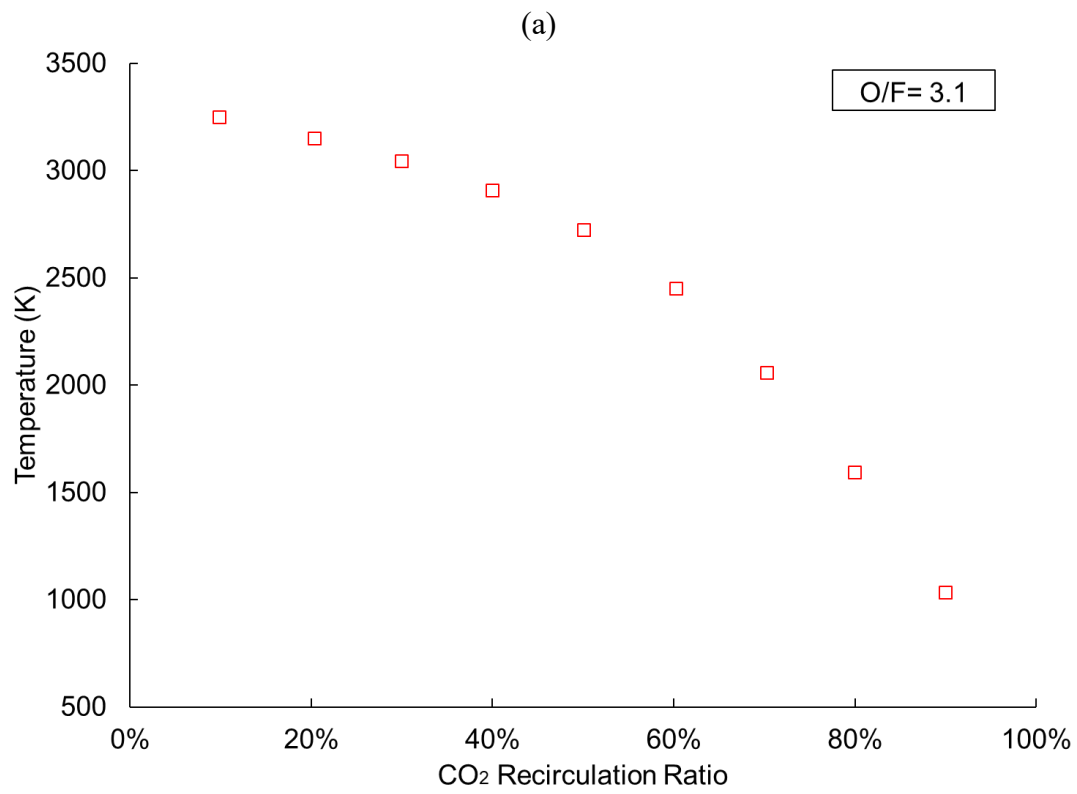
Figure 44 Total stress and Yield Strength vs the temperature

One of the advantages of oxy-methane combustion is that the combustion product consists mostly of carbon dioxide and water vapor [1-10]. The exhaust carbon dioxide can be recirculated back into the combustor for reducing the combustion temperature. Figure 45(a-b) shows the temperature reduction due to carbon dioxide dilution. The carbon dioxide recirculation ratio is calculated using Equation 24 where, \dot{m}_{CO_2} , \dot{m}_{O_2} and \dot{m}_{CH_4} are mass flowrate of carbon dioxide, oxygen and methane respectively.

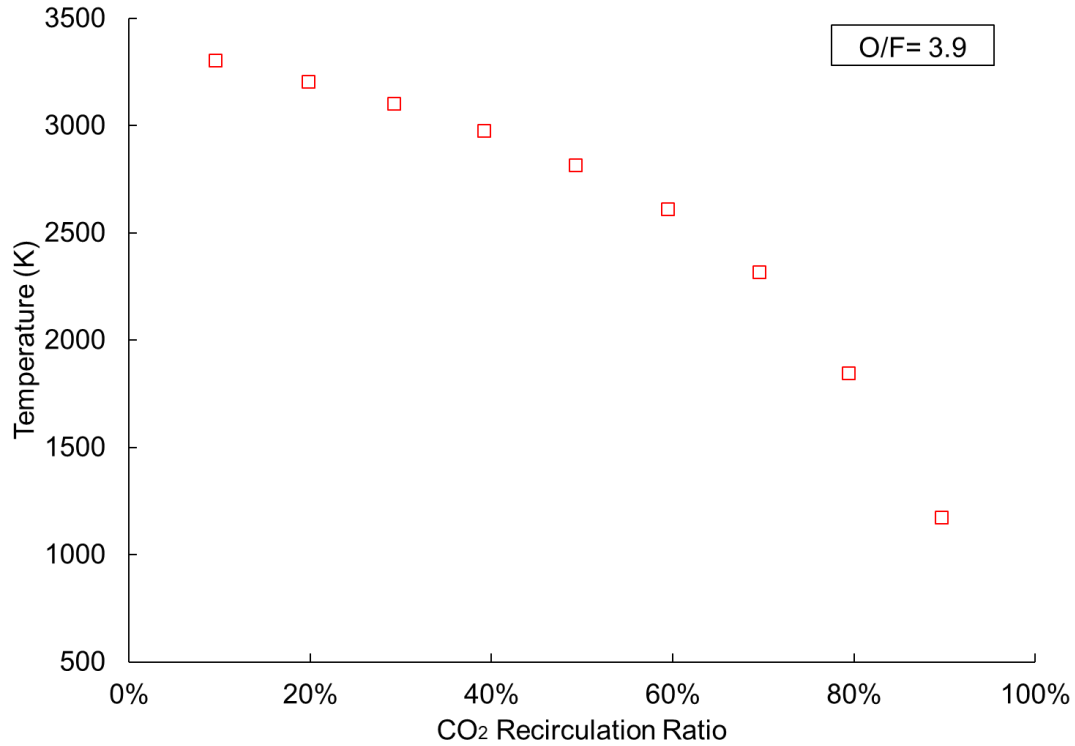
$$\dot{m}_{\text{CO}_2} = \dot{m}_{\text{CO}_2} / (\dot{m}_{\text{CH}_4} + \dot{m}_{\text{O}_2} + \dot{m}_{\text{CO}_2}) \quad (24)$$

The analysis is performed Chemkin Pro software package. GRIMECH 3.0 reaction mechanism is used to evaluate the combustion temperature. It can be seen from Figure 45(a-b) that the overall combustion temperature decreases as the CO₂ recirculation ratio increases. For case 1 the lowest combustion temperature obtained 953 K at 90% carbon dioxide recirculation ratio. Similar trend is observed for case 2 and case 3. The lowest combustion temperature is obtained 1030 K and 1175 K at 90% recirculation ratio for case 2 and case 3, respectively. However, the CO₂ possesses some





(b)



(c)

Figure 45 Effect of CO₂ recirculation ratios on adiabatic flame temperature (a) case 1, (b) case 2 and (c) case 3

concerns in terms of flame ignition. Literature study shows that the dilution of carbon dioxide introduces ignition delay which may have inverse impact on burner ignition [47,48]. Ignition delay refers to the time interval between the fuel injection and the start of the combustion [47,48]. Figure 46 exhibits the ignition delay due to the carbon dioxide dilution for three cases. The ignition delay estimations are performed using Chemkin Pro software package. The initial condition for the calculations are obtained from the test conditions. The carbon dioxide recirculation ratio is varied from 10% to 90%. It is found that as the carbon dioxide recirculation ratio increases the ignition delay time increases for all three cases. It is also found that O/F mixture ratios have significant impact on the ignition delay characteristics. From Figure 46 it can be seen that between 10% to 60% the ignition delay doesn't vary much among the three cases even though O/F ratios are different for all three cases. It is also observed that between 70% to 90% the ignition delay time increases as the O/F ratios are decreases. The ignition delay time is comparatively less while the

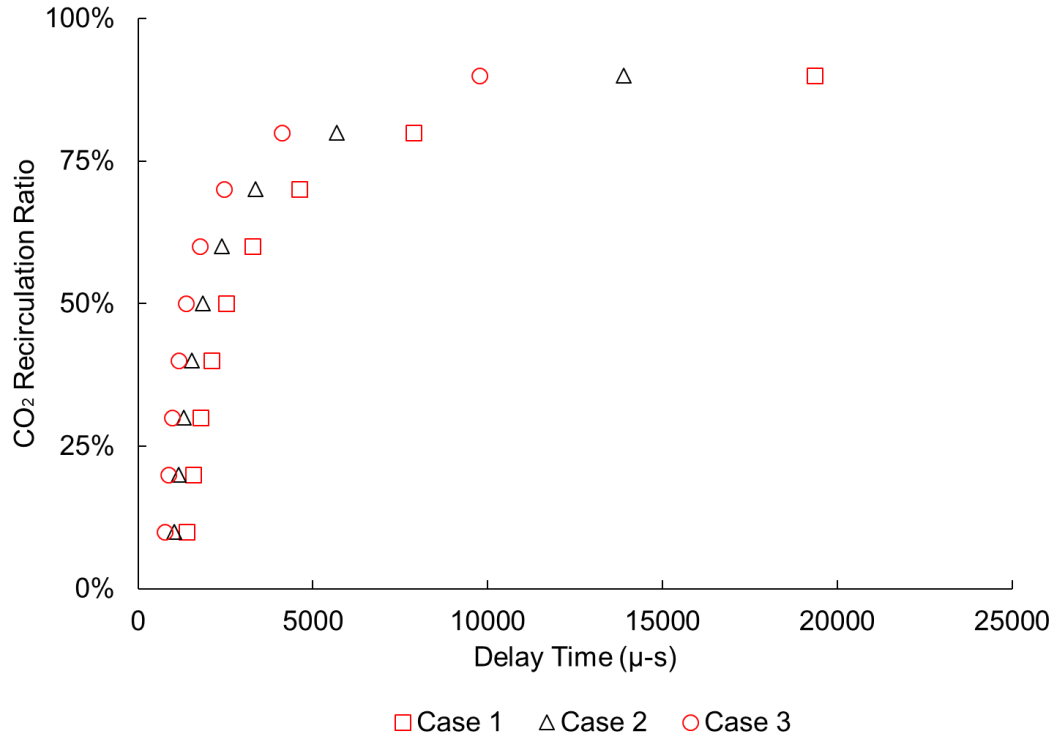


Figure 46 Effect of CO₂ recirculation ratios on ignition (a) case 1, (b) case 2 and (c) case 3

test is conducted close to stoichiometric condition. For case 3 the O/F ratio is 3.9 and ignition delay time is 14000 μ -s for 90% carbon dioxide recirculation. On the other hand, for case 1 the O/F ratio is 2.72 and ignition delay time is 19000 μ -s for 90% carbon dioxide recirculation. Thus, the cooling system must be designed such a way that the burner ignition does not get effected, at the same time combustor wall reaches below the material allowable temperature.

To meet the cooling system requirements, the design shown in Figure 47Table is implemented. This design will inject a high velocity ring of room temperature CO₂ along the inner walls of the combustor. In this configuration, CO₂ will act as a protective layer, keeping the walls at a low temperature protecting from the high temperature steam that may lead to accelerated corrosion. The modular design enables quick change of plates for different flow distribution configurations without having to disassemble or remanufacture the combustor. The carbon dioxide mass flowrates for the three cases at different carbon dioxide recirculation ratio is presented in Table 15. Detailed combustor design is presented in chapter 2.

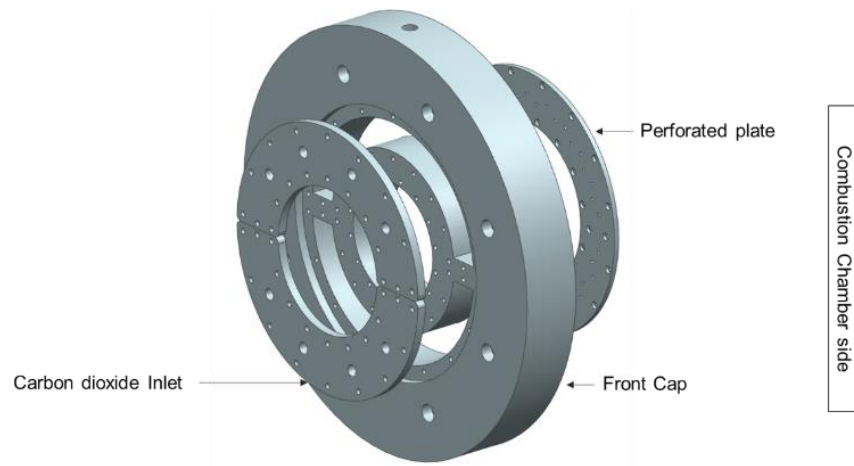


Figure 47 CO₂ cooling system manifold

Table 15 Carbon dioxide mass flowrates for different cases

CO ₂ Recirculation Ratio	Case 1	Case 2	Case 3
	CO ₂ Mass Flowrate (kg/s)	CO ₂ Mass Flowrate (kg/s)	CO ₂ Mass Flowrate (kg/s)
10 %	0.001428	0.001749	0.002399
20 %	0.003212	0.003935	0.005398
30 %	0.005507	0.006746	0.009254
40 %	0.008566	0.010494	0.014395
50 %	0.012849	0.015741	0.021593
60 %	0.019274	0.023612	0.032389
70 %	0.029981	0.03673	0.050383
80 %	0.051396	0.062965	0.086371
90 %	0.115641	0.141672	0.194335

Chapter 5: Supercritical Combustor Development

The ultimate goal of the project is to develop a laboratory scale supercritical oxy-combustor for continuous operation. Since the employment of supercritical fluid in gas turbine is fairly new concept there are many questions that need to be answered. This part of the dissertation provides a preliminary guideline for developing a laboratory scale supercritical oxy combustor. The knowledge obtained from the high pressure (up to 20 bar) test will assist in understanding the combustion chamber pressurization mechanism and flame behavior at high pressure. In this section a cycle analysis on a commercial scale directly heated oxyfuel supercritical gas turbine is presented. The analysis provides an overview of the cycle configuration and cooling mechanism. Afterwards, an investigation is conducted to understand the impact of equation of states in supercritical fluid analysis. Finally, a CFD analysis is performed on a 100 bar and 300 bar laboratory scale supercritical combustor based on the high pressure oxy-combustor pressurization mechanism. The analysis is conducted for firing input of 1 MW.

5.1 Cycle Analysis

There are very few studies have investigated the use of supercritical fluids in an oxy-based Brayton cycle configuration and no known studies have been performed to optimize the fuel and oxygen pressurization and delivery configuration for this system. Authors of previous studies typically show the delivery of the supercritical fluid to the combustion chamber without many details on how the elevated pressure was achieved. Since very few studies exist on the topic of directly heated supercritical gas turbines despite their promise of higher efficiency and reduced physical footprint it is deemed beneficial to investigate their performance in detail. In order to fill this gap a cycle analysis is performed on a commercial scale directly heated supercritical oxyfuel Brayton cycle to determine the optimal pressurization and feed system (either gaseous or compressed liquid) for oxygen, fuel, and CO₂ recirculation, and an overall system efficiency and thermal efficiency analysis of the various configurations mentioned. The cycle analyses are performed using ASPEN HYSYS®.

Previous studies determined that the liquid feed system is more efficient and a commercially viable option for a supercritical power generation system [1]. However, it was also found that the expected oxy-methane combustion temperatures could reach as high as 3500K. Due to existing material limitations this is not feasible, as some studies have shown that the maximum allowable temperature for supercritical combustion is 1400 to 1500 K [1,19,23]. One of the advantages of oxyfuel combustion is that the exhaust carbon dioxide can be recirculated to reduce the combustion temperature [23,25-29]. From various literature sources in order to reduce the temperature down to the material operating limit more than two thirds of exhaust carbon dioxide need to be recycled into the combustor [23,25-29]. Thus, in order to operate within the material operability range, a significant amount of carbon dioxide needs to be recirculated to reduce the temperature to 1400K. Since it is required to recycle CO₂, it is desired to build this system using the most efficient configuration. The purpose of this portion of the investigation is to determine the most efficient carbon dioxide recirculation methodology that will provide higher efficiency.

In this section two CO₂ recirculation methods are considered. The first case assumes the CO₂ is cryogenically cooled to a liquid and pumped to a supercritical state, this is the so called liquid feed system configuration (Figure 48 (a)). The second case assumes that gaseous CO₂ is compressed to a supercritical state using a compressor and delivered to the combustion chamber, this is the so called gaseous feed system configuration (Figure 48 (b)). Thermodynamic analysis shows that to reduce the temperature to the material operating limit of 1400K an amount of 84% and 88% of carbon dioxide should be recirculated for the liquid and gaseous CO₂ feed system configurations, respectively. The inlet temperatures of the CO₂ recirculation into the combustion chamber for liquid and gaseous phase are 214 K and 525 K, respectively. For this analysis, the exhaust mass flowrate and gross power production are kept constant. The analysis reveals that gross power production depends on the amount of working fluid. For both cases, the gross power production is 590 MW, the detailed power distribution and efficiency values are shown in Tables 5 and 6. From literature the air separation unit generally requires 15-20% power input and the CO₂ capture unit requires 9-10% of the gross power production [2,30]. For this study, the analysis is

conducted assuming that the required power for the air separation unit is 16-17% of the gross power production while recirculating gaseous and liquid carbon dioxide. The power consumed by the CO₂ capture unit is estimated to be 10% of the gross power production.

Table 16 Power consumption distribution for different CO₂ recirculation configurations when combined with a liquid methane and oxygen feed system

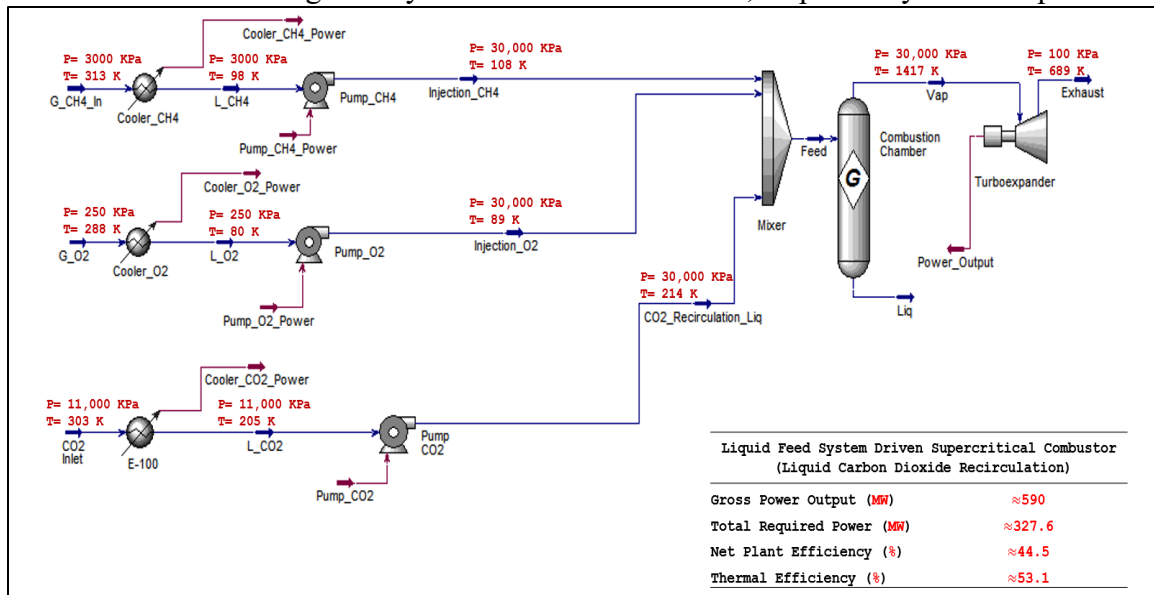
Power Consumption (MW)	w/ Liquid CO₂	w/ Gaseous CO₂
	Recirculation Feed	Recirculation Feed
Air Separation Unit	100	90
Methane Pump	1.7	1.2
Oxygen Pump	2.7	2
Carbon Dioxide Pump	9.2	0
Methane Condenser	21	16
Oxygen Condenser	36	27
Carbon Dioxide Condenser	98	-
Carbon Dioxide Compressor	-	70
Carbon Dioxide Capture Unit	59	59
Total Power Consumption (MW)	327.6	265.2

Table 17 Power production for the two different CO₂ recirculation configurations assuming a liquid methane and oxygen delivery system

Table 17 Power production for the two different CO₂ recirculation configurations assuming a liquid methane and oxygen delivery system

	Liquid CO₂	Gaseous CO₂
	Recirculation Feed	Recirculation Feed
Gross Power Production (MW)	590	590
Net Power Production (MW)	262.4	324.8
Net Plant Efficiency (%)	44.5	55.1
Thermal Efficiency (%)	53.1	60.1

The analysis shows that the estimated net plant and thermal efficiency while incorporating gaseous carbon dioxide recirculating feed system is 55.1% and 60.1%, respectively. The net plant and



(a)

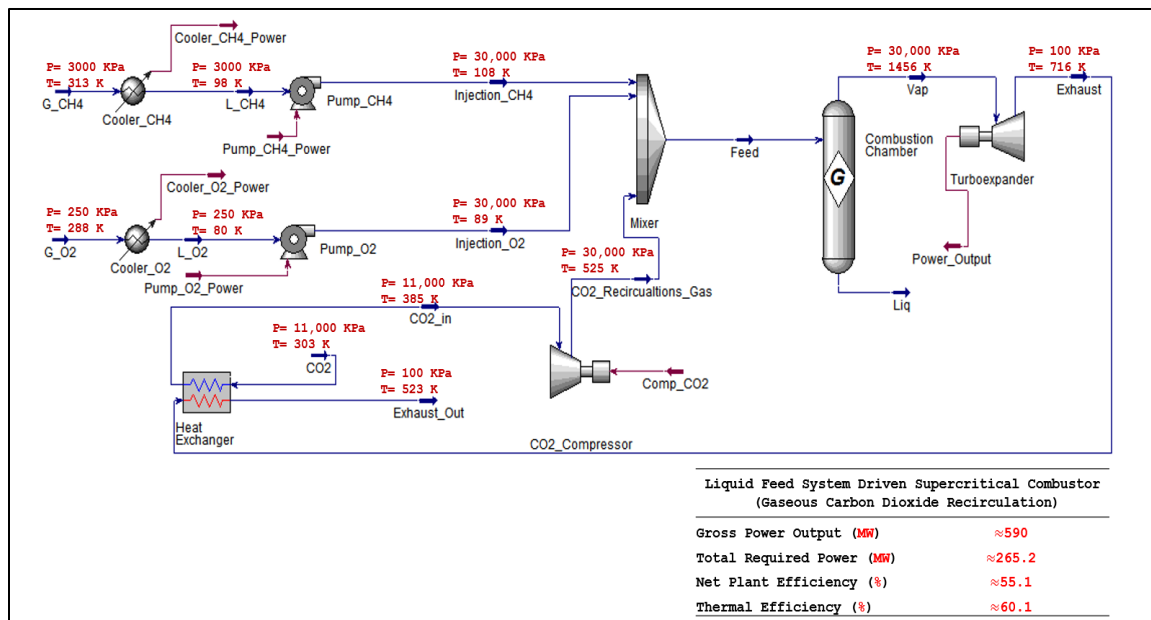


Figure 48 ASPEN HYSYS® layout of the liquid feed methane and oxygen feed system supercritical combustor, (a) showing liquid CO₂ recirculation, (b) showing gaseous CO₂ recirculation

thermal efficiency when incorporating liquid carbon dioxide recirculating feed system is 44.5 % and 53.1%, respectively. This lower efficiency is due to the power consumption required for the condensation and pumping process of the carbon dioxide. Given the total exhaust mass flowrates and gross power output, the net power production for liquid carbon dioxide recirculation feed is 262.4 MW and power output for a system using gaseous carbon dioxide recirculation feed is 324.8 MW. Thus, it is recommended to arrange this type of system so that gaseous carbon dioxide can be delivered and compressed into the combustion chamber while the fuel and oxidizer are introduced in a liquid phase.

5.2 Comparison of Equation of States for Supercritical Fluid Analysis

A wide range of fluid properties is provided by the National Institute of Standards and Technology (NIST) for scientific use. Typically, the property values are measured experimentally and provided as a function of pressure or temperature by NIST. It is found that the property values are available for sufficiently high pressure range. However, it is limited to temperatures typically below the range applicable for combustion. On the contrary, JANAF tables provide fluid properties up to 6000K, although the properties are given at 1 atm pressure [49]. Therefore, these tables are not applicable for high pressure supercritical combustion analysis. Figure 49 is a graphical representation of the NIST data for supercritical fluids of interest in this study. Methane properties are available up to 1000 MPa (10000 bar). However, temperatures are limited to be between 90 to 625 K. Oxygen property values are available up to 82 MPa (820 bar) with the temperature limit of 54 to 1000 K. Carbon dioxide property values are available up to 800 MPa (8000 bar) with the temperature limit of 216 to 1100 K. Water property values are available up to 1000 MPa (10000 bar) with the temperature limits between 273 to 1275 K. Beyond this range the property values need to be calculated using formulations.

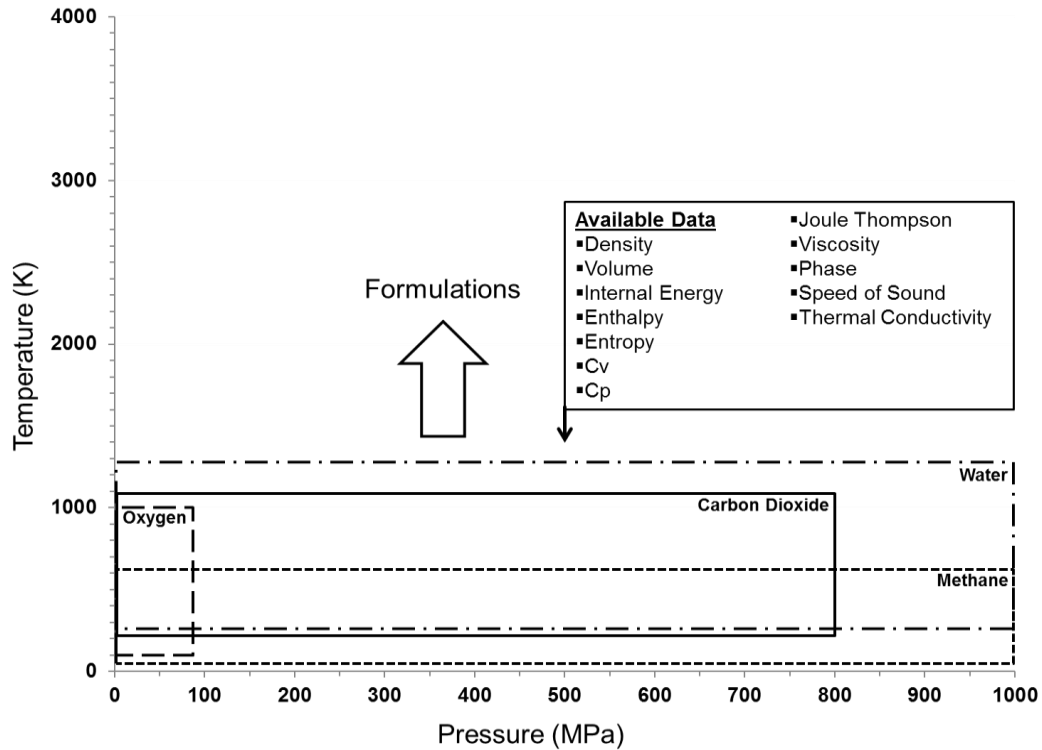


Figure 49 Thermodynamic properties availability (NIST database)

Since directly heated supercritical oxy-combustion promises to achieve high efficiencies with low pollutant emissions and since it is very new, there are many questions that need to be answered. Thus, for this purpose a study is performed to investigate the use of three different equations of state (EOS) methods and their impact on results when coupled with the flow computations [50]. Current literature suggests that the Lee Kesler equation of state (EOS) is most appropriate for analyzing supercritical combustion [21]. However, many commercial software packages, such as Fluent which is a popular computational modeling tool, do not contain the Lee Kesler EOS. Instead Fluent has built into it the Peng Robinson EOS and ideal gas law models. It would be useful to know whether it is necessary to incorporate a more complex model, such as the Lee Kesler EOS, and if the fidelity of the results would greatly improve. Lee and Kesler have expressed the compressibility factor of any fluid in terms of the compressibility factor of the reference fluid and the simple fluid [51-53], Equation 20. The simple fluid is defined by a type of fluid that consists of either an element or molecules involving no more than two types of atoms

[14]. On the other hand, a reference fluid characterizes the behavior of a wide range of chemically similar fluids.

$$z = z^{(o)} + \frac{\omega}{\omega^{(r)}} \cdot (z^{(r)} - z^{(o)}) \quad (25)$$

In Equation 25, the superscript (o) and (r) represent the simple fluid and reference fluid, respectively. The compressibility factor for both of these fluids are calculated using Benedict-Webb-Rubin (BWR) equation, Equation 26.

$$z = 1 + \frac{B}{V_r} + \frac{C}{V_r^2} + \frac{D}{V_r^5} + \frac{c_4}{T_r^3 V_r^2} \left(\beta + \frac{\gamma}{V_r^2} \right) \exp \left(-\frac{\gamma}{V_r^2} \right) \quad (26)$$

where,

$$B = b_1 - \frac{b_2}{T_r} - \frac{b_3}{T_r^2} - \frac{b_4}{T_r^3}$$

$$C = c_1 - \frac{c_2}{T_r} + \frac{c_3}{T_r^3}$$

$$D = d_1 + \frac{d_2}{T_r}$$

The value of the coefficients can be found in Table 18.

Table 18 Constants for the BWR-Lee-Kesler equation

Constant	Simple Fluid	Reference Fluid	Constant	Simple Fluid	Reference Fluid
b ₁	0.1181193	0.2026579	c ₃	0.0	0.016901
b ₂	0.265728	0.331511	c ₄	0.042724	0.041577
b ₃	0.154790	1.027655	d ₁ x 10 ⁴	0.155428	0.48736
b ₄	0.030323	0.203488	d ₂ x 10 ⁴	0.623689	0.0740336
c ₁	0.0236744	0.0313385	β	0.65392	1.226
c ₂	0.0186984	0.0503618	γ	0.060167	0.03754

Lee et al. [49] has provided the detailed procedure for calculating the thermodynamic properties using the Lee Kesler method. The isothermal enthalpy, isothermal entropy, isochoric

heat capacity and isobaric heat capacity departure are derived from Equation 21 by following the Lee Kesler method. They are stated in Equation. 27-31, respectively.

Isothermal enthalpy departure,

$$\frac{\Delta h}{R.T_c} = \frac{h-h^0}{R.T_c} = T_r \left[z - 1 - \frac{b_2 + 2b_3/T_r + 3b_4/T_r^2}{T_r.V_r} - \frac{c_2 - 3c_3/T_r^2}{2T_r.V_r^2} + \frac{d_2}{5T_r.V_r^2} + 3E \right] \quad (27)$$

with,

$$E = \frac{c_4}{2T_r^3.V_r} \left[\beta + 1 - \left(\beta + 1 + \frac{\gamma}{V_r^2} \right) \exp\left(-\frac{\gamma}{V_r^2}\right) \right]$$

Isothermal entropy departure,

$$\frac{\Delta s}{R} + \ln \frac{p}{p^0} = \frac{s-s^0}{R} + \ln \frac{p}{p^0} = \ln z - \frac{b_1 + b_3/T_r^2 + 2b_4/T_r^3}{V_r} - \frac{c_1 - 2c_3/T_r^3}{2V_r^2} - \frac{d_1}{5V_r^5} + 2E \quad (28)$$

Isochoric heat capacity departure,

$$\frac{C_v - C_v^0}{R} = \frac{2(b_3 + 3b_4/T_r)}{T_r^2.V_r} - \frac{3C_3}{T_r^3.V_r^2} - 6E \quad (29)$$

Isobaric heat capacity departure,

$$\frac{C_p - C_p^0}{R} = \frac{C_v - C_v^0}{R} - 1 - T_r \left(\frac{\partial P_r}{\partial T_r} \right)_{V_r}^2 / \left(\frac{\partial P_r}{\partial V_r} \right)_{T_r} \quad (30)$$

In this study, the Plocker-Knapp mixing rule is coupled with the Lee Kesler formulations that calculates the mixing of the combustion products. The Lee Kesler Plocker (LKP) EOS does not have an analytic solution for the compressibility factor. Moreover, it is a non-linear function of reduced temperature (T_r), reduced pressure (P_r), and reduced specific volume (V_r). The Van Wijngaarden-Dekker-Brent numerical scheme is used to evaluate the root of the LKP EOS. Additionally, the Chung-Lee-Starling [52] method is used to formulate dynamic viscosity and thermal conductivity. All these formulations are implemented in the Fluent via a User Defined Function (UDF).

The formula for calculating the compressibility factor using the Peng Robinson (PR) EOS is stated in Equation 26 [51]. It is observed that, unlike LKP method, the PR EOS utilizes the cubic root method for evaluating the compressibility factor.

$$Z^3 - (1-B) Z^2 + (A-3B^2-2B) Z - (AB-B^2-B^3) = 0 \quad (31)$$

where,

$$A = \frac{aP}{R^2T^2}$$

$$B = \frac{bP}{RT}$$

$$Z = \frac{P\theta}{RT}$$

At critical points the values of a and b can be written as following:

$$a(T_c) = 0.45724 \frac{R^2 T_c^2}{P_c}$$

$$b(T_c) = 0.07780 \frac{RT_c}{P_c}$$

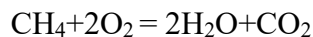
The thermo-physical properties of the mixture such as density, sensible enthalpy, total enthalpy, entropy, specific heats, density derivatives (dp/dP , dp/dT), enthalpy derivatives (dH/dP , dH/dT), and the speed of sound can be derived from Equation 30. The Peng Robinson EOS is already embedded into the Ansys Fluent. Therefore, the analysis is conducted by selecting the PR EOS method directly from Fluent. The fundamental difference between LKP EOS and the PR EOS lies in the approach of calculating the compressibility factor. The LKP method utilizes the reference fluid compressibility factor for evaluating the actual compressibility factor, whereas, the PR EOS employs a cubic root approximation. Besides, the coefficients used for calculating the compressibility factor of the simple and reference fluid are obtained experimentally. Hence, the LKP EOS tends to provide closer approximation of the compressibility factor than the PR EOS.

The Lee Kesler EOS along with Plocker Knapp mixing rule is coupled with Fluent via a user defined function (UDF). Comparisons are made between the Lee Kesler EOS, Peng Robinson EOS, and the ideal gas law. These different models are tested using a coaxial shear injector at a pressure of 30MPa (300 bar). Since little is known about the combustion kinetics at this elevated pressure, 30MPa (300 bar), for simplicity the model presented in this paper has been conducted assuming one-step reaction chemistry. Therefore, only 4 species (H_2O , CH_4 , O_2 , CO_2) are considered in this study. Basic properties such as critical temperature, critical pressure, critical density, acentric factor, dipole moment, critical specific volume, molecular weight are obtained from the NIST database. The UDF performance is validated by comparing the results from ASPEN Plus process simulator. The comparison demonstrates an agreement within $\pm 0.5\%$ difference for

multiple compositions, temperatures, and pressure conditions. The study shows that the Peng Robinson equation of state under predicts the chamber temperature in comparison to the Lee-Kesler Plocker model. This is due to the assumptions and methodology made in each model for the thermodynamic properties of the fluid. It is believed that the Lee-Kesler Plocker EOS represents a better approximation of temperature since the equations used are based on experimental data and prior literature suggests use of this model [11]. However, the density approximation between these two models varies less than 5%. The detailed analysis is provided by Chowdhury and Kim et al. [50]. The employment of LKP for CFD analysis significantly increases the simulation time. Even though LKP provides better approximation of the combustion characteristics Peng Robinson is more cost effective. In addition to that, combustion kinetics at supercritical condition must be developed to accurately simulate the combustion phenomenon. Therefore, Peng-Robinson is used for the further analysis incorporating one step reaction model.

5.3 CFD Analysis

A CFD analysis is performed to investigate the effect of real gas model and simplified combustion chemistry in supercritical combustion simulation. A steady state pressure based solver is used for the calculations. The simulation is performed in 2D domain. The geometry that is used for this analysis is as same as the high pressure (< 20 bar) combustor. However, the length of the chamber is reduced to 300 mm. The standard k- ϵ model is chosen for the turbulence modeling. For the combustion, the species transport model is employed incorporating one step reaction chemistry. During the simulation methane is used as the fuel and pure oxygen is used as the oxidizer. The combustion products are carbon dioxide and water vapor. The combustion reaction is shown below:



The P-1 radiation model is incorporated with the model to simulate the radiation effect. During the simulation carbon dioxide is used as the diluent. The inlet temperature for fuel, oxidizer and diluent is chosen to be atmospheric temperature. The Peng-Robinson real gas model is used to simulate

the real gas effect. The power input is 1 MW. The carbon dioxide recirculation ratio is 90%. The pressure is set to be 100 bar and 300 bar at the outlet of the chamber, Figure 50.

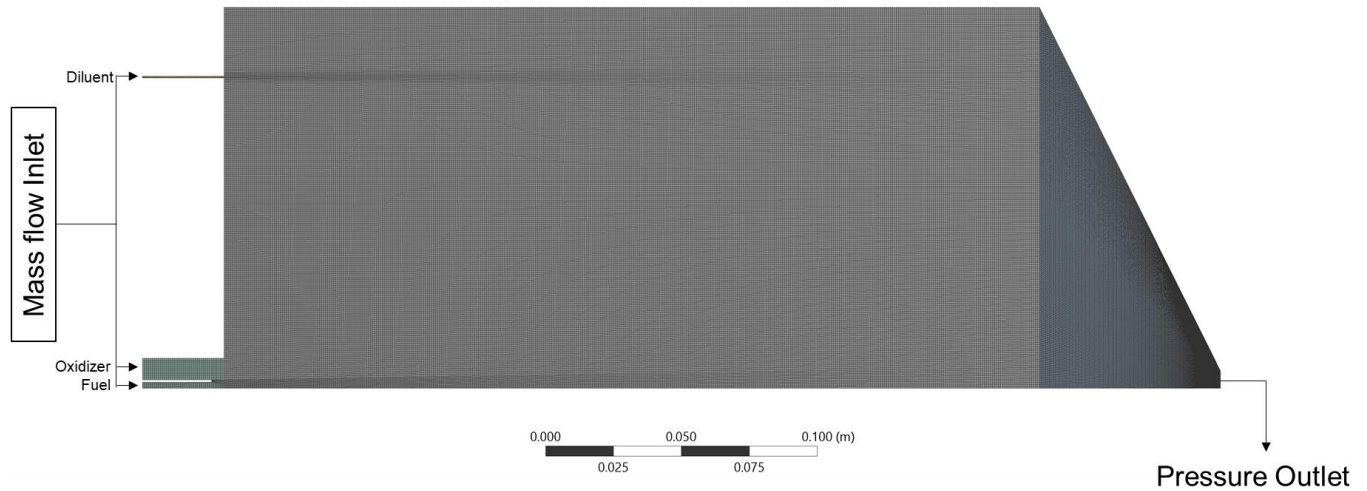


Figure 50 Mesh (Supercritical combustion simulation)

A summary of the computational model is shown in Table 19.

Table 19 Boundary condition (Supercritical combustion simulation)

Section	Input
General	
Type	Pressure Based
Time	Steady State
Models	
Energy	On
Viscous Model	k- ϵ (Standard)
Radiation	P-1 (On)
Species	Species Transport
Boundary Conditions	

Method	Axisymmetric Boundary
Inlets	<ul style="list-style-type: none"> - Fuel (Methane) Inlet Temperature: 300 K - Oxidizer (Oxygen) Inlet Temperature: 300 K - Diluent (Carbon Dioxide) Inlet Temperature: 300 K
Outlet	Pressure Outlet: 100 bar and 300 bar
Wall	Combustor Wall: Adiabatic
Solution	
Method	<ul style="list-style-type: none"> - Scheme-Coupled - High Order Term Relaxation
Initialization	Hybrid

To understand the real gas effect and the combustion temperature, the temperature inside the combustor and compressibility factor is plotted at four different radial direction with respect to the axial direction, Figure 51 and 52. Figure 51 demonstrate the temperature profile inside the combustor. It can be seen from the figures that the maximum temperature goes up to 4300 K for 100 bar and 4700 K for 300 bar case. During the CFD simulation species transport model is used integrating one step reaction chemistry. The combustion products are only carbon dioxide and water vapor. The existing knowledge regarding combustion chemistry is not well equipped for modeling supercritical combustion phenomenon. Therefore, the CFD simulation overestimate the combustion temperature. However, to use CFD simulation as the designing tool for the cooling system, it is important to understand the combustion characteristics. Otherwise, the simulation results may misinterpret the temperature profile and the cooling system design won't be accurate. Therefore, detailed combustion chemistry at the supercritical condition must be developed and should be incorporated to accurately replicate the combustion phenomenon.

The ideal gas approximation does not compare well with physical parameters measured from a supercritical fluid. Generally, ideal gas assumptions are made at lower than supercritical pressures. Assumptions typically used for ideal gases are shown in Equation (32,33) [53,54]. In these equations P_r represents the reduced pressure, P the actual pressure, P_{cr} the critical pressure, T_r the reduced temperature, T the actual temperature, and T_{cr} the critical temperature.

$$P_r = P/P_{cr} \ll 1$$

(32)

$$T_r = T/T_{cr} > 2$$

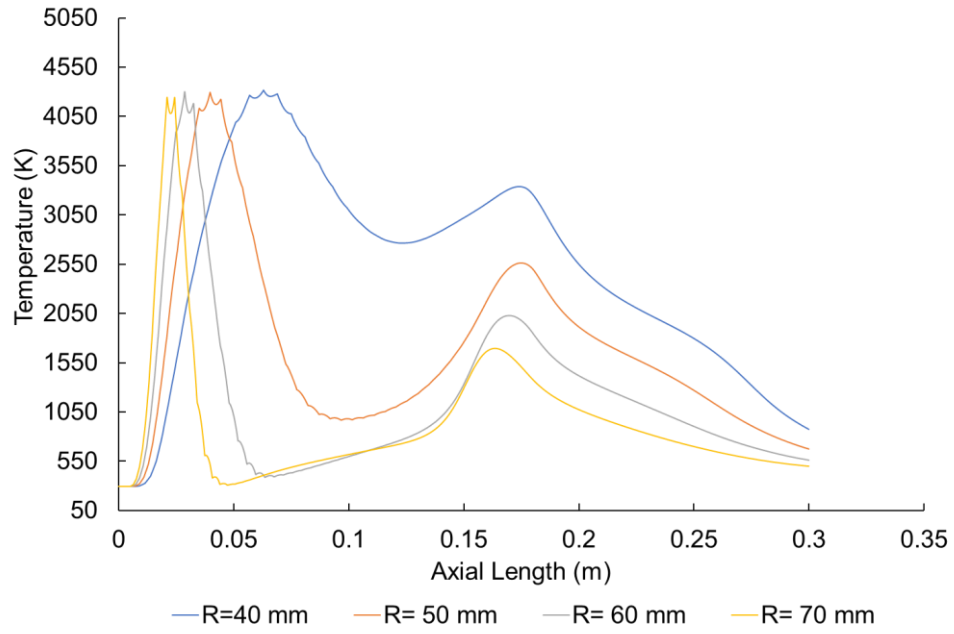
(33)

For the current study, the supercritical combustion process results in relative pressure raises above 1 and relative temperatures below 2 for the different fluids. Therefore, the combustion products behave as real gas. Critical properties of the corresponding fluids are shown in Table 20.

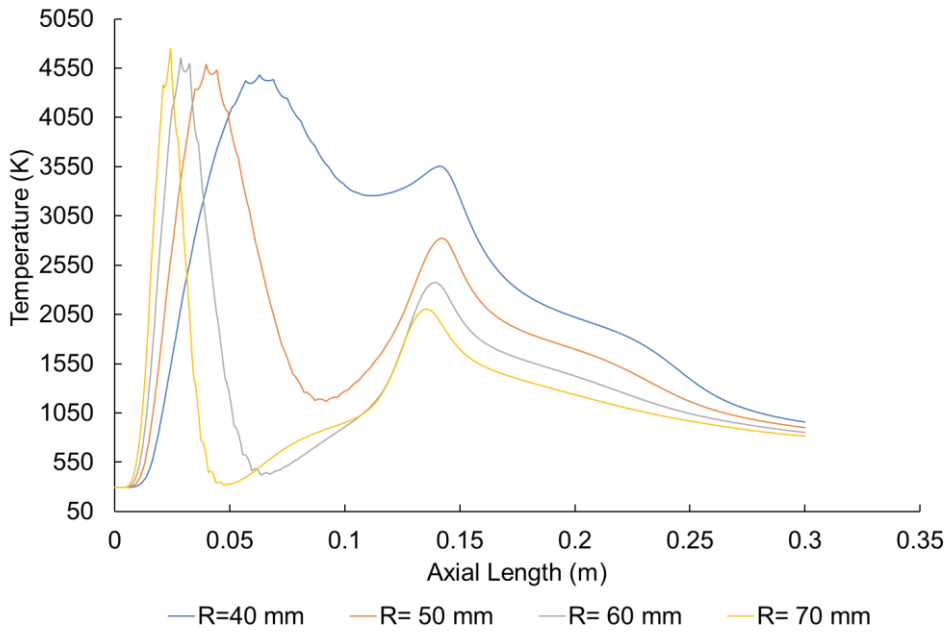
Table 20 Critical properties of fluids

Elements	Critical Pressure (bar)	Critical Temperature (K)
CH ₄	45	190
O ₂	50	154
CO ₂	74	304
H ₂ O	221	647

The simulations are conducted at 100 bar and 300 bar pressure. At, 100 bar only carbon dioxide reaches to supercritical phase. This is because the critical pressure for water vapor is 221 bar. On the other hand, at 300 bar both carbon dioxide and water vapor reaches to supercritical phase. It can be seen from Figure 52(a) and 52(b) that, the compressibility factor varies between 0.8 and 1.03 for 100 bar case and between 0.87 and 1.07 for 300 bar case. It is observed that, as the pressure increases the compressibility factor increases. Thus, it can be summarized that real gas model must be used for supercritical combustion analysis.

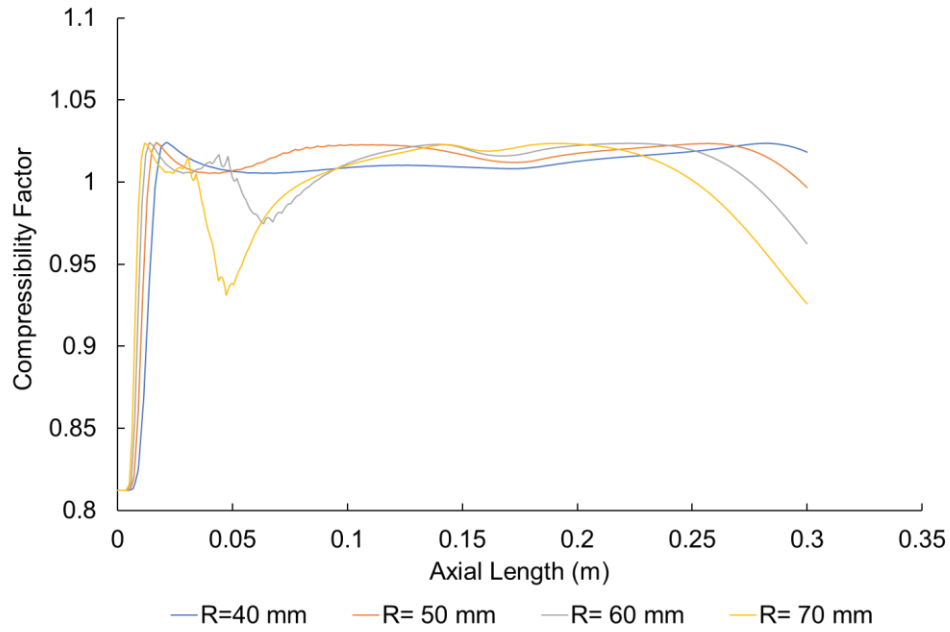


(a)

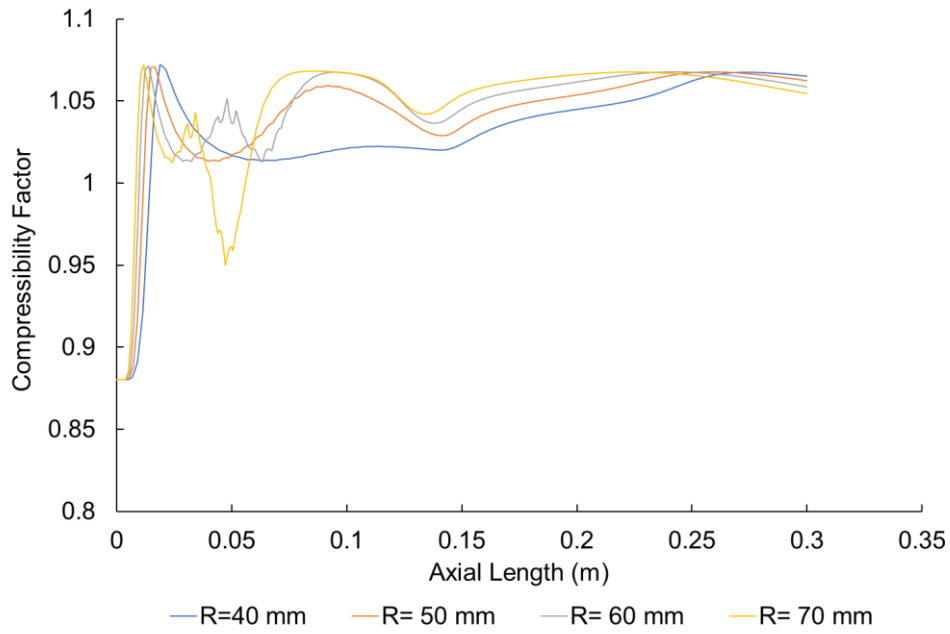


(b)

Figure 51 Temperature with respect to axial distance: (a) 100 bar case and (b) 300 bar case



(a)



(b)

Figure 52 Compressibility factor with respect to axial distance: (a) 100 bar case and (b) 300 bar case

Chapter 6: Summary and Future Work

The main purpose of this dissertation is to perform qualitative analysis on oxy-methane combustion at high pressure (< 20 bar) and compare to CFD model for future scale up to supercritical condition. This is a orderly first step in testing at elevated pressures of 100 and 300 bar pressures. During this experimental study a combustor is designed, developed and tested up to a 250 kW firing inputs and 20 bar pressure. To deliver the required power input, a shear-coaxial injector is designed using methane as the fuel and oxygen. In the dissertation, the test data are presented for 150 kW – 250 kW thermal power inputs and up to 12.5 bar-g pressure. A CFD analysis is conducted to simulate the combustion process. The simulation is performed using a 2D domain to replicate and design for the experiments. While performing the CFD simulation the exit area of the combustor is selected iteratively to replicate the test pressure. The key findings from the study can be summarized as followings:

- It is found that while performing the CFD analysis the 7.5 bar chamber pressure is gained for 5.5 mm exit diameter which is 14% lower than the analytical estimation, 6.40 mm. The 6.40 mm exit diameter results in chamber pressure of 5.5 bar. Similarly, during the CFD simulation the 10 bar chamber pressure is attained for 5.0 mm exit diameter which is 18% lower than the analytical estimation of 6.1 mm. The 6.1 mm exit diameter provides chamber pressure of 8 bar. While performing the CFD analysis the 12.5 bar chamber pressure is gained for 5.25 mm exit diameter which is 16% lower than the analytical estimation, 6.27 mm. The 6.27 mm exit diameter delivers chamber pressure of 10 bar. Therefore, it can be summarized that the error between the analytical calculation and CFD estimation falls within 14%-18%. However, during the test the exit area is kept constant at 3.175mm. The error between the CFD estimation and exit area in real tests for case 1, case 2 and case 3 are 42%, 37% and 40%.

- It is summarized that between the CFD estimation and actual test the CFD estimation over predicts the exit diameter. During the actual test gas may leak from different joints and fittings. Furthermore, while doing the CFD analysis the combustion product and flame temperature is evaluated using the PDF table. The integration of multistep detailed chemistry may improve the error percentage between the CFD analysis and the actual test.

- The CFD analysis provides a better understanding about the near wall temperature profile at steady state condition. It is observed that the combustor wall temperature passes the material operation range for all three cases. A thermo-mechanical analysis is conducted to determine the maximum operating temperature for the combustor wall. It is found that the maximum operating temperature is 600 K. Therefore, the combustor requires cooling system for steady state operation.

- Carbon dioxide can be used as the diluent for reducing the combustion temperature. However, the dilution of carbon dioxide possesses a concern in terms of ignition delay. The ignition delay estimations are performed using Chemkin Pro software package. The initial condition for the calculations are as same as the test conditions. The carbon dioxide recirculation ratio is varied between 10% and 90%. It is observed that as the carbon dioxide recirculation ratio increases the ignition delay time increases for all three cases. It is detected that between 10% to 60% the ignition delay doesn't vary much among the three cases even though O/F ratios are different. However, it is found that between 70% to 90% the ignition delay time increases as the O/F ratios are decreases. The ignition delay time is comparatively less while the test is conducted close to stoichiometric condition. For case 3 the O/F ratio is 3.9 and ignition delay time is 14000 μ -s for 90% carbon dioxide recirculation. On the other hand, for case 1 the O/F ratio is 2.72 and ignition delay time is 19000 μ -s for 90% carbon dioxide recirculation. Therefore, the cooling system must be designed such a way that the burner ignition does not get effected, at the same time combustor wall reaches below the material allowable temperature.

- For the steady state experiments a cooling mechanism is designed such a way that it will inject a high velocity ring of room temperature CO₂ along the inner walls of the combustor. In this configuration, CO₂ will act as a protective layer, keeping the walls at a low temperature protecting from the high temperature steam that may lead to accelerated corrosion. The modular design enables quick change of plates for different flow distribution configurations without having to disassemble or remanufacture the combustor.

- To perform the test for steady state condition feed system must be modified. While performing the tests, methane is delivered from k-bottles (maximum capacity 350 SCF). A larger system must be implemented for continuous operation. It is detected from the experiments that the oxygen flowrates oscillate significantly during the operation. This may cause trouble during steady state operation. The gas delivery system along with the regulators must be modified to prevent any kind of disruption during gas flow. The current setup is equipped with gas tanks to deliver carbon dioxide for cooling. However, these tanks operate at very low pressure (maximum operating pressure 28 bar/ 400 psi) and low flowrates. To safely deliver carbon dioxide gas, a liquid system along with vaporizer must be installed. A detailed specification of a electric vaporizer is provided in the appendix.

- The experimental work presented in the dissertation is extended to a model for a supercritical (100 bar and 300 bar) oxy-methane burner and combustor design. At first a cycle analysis is presented to demonstrate the superiority of supercritical gas turbine over existing gas turbines. A CFD model for developing supercritical oxy-methane burner and the combustor, incorporating real gas model, is presented. Due to the computational time Peng Robinson equation of state is used for simulating supercritical fluid. It is detected that the compressibility factor varies between 0.8 and 1.03 for 100 bar case and between 0.87 and 1.07 for 300 bar case. It is also observed that the compressibility factor increases with the pressure. It is found

that existing knowledge is not enough to simulate combustion at supercritical phase. Detailed combustion chemistry at the supercritical condition must be developed and should be incorporated to accurately replicate the combustion phenomenon.

References

- [1] McClung A, Brun K, Chordia L. Technical and economic evaluation of supercritical oxy-combustion for power generation. In: 4th International supercritical CO₂ power cycles symposium (2014), Paper No. 40; Southwest Research Institute; Pittsburgh, Pennsylvania.
- [2] Hong, J., Field, R., Gazzino, M., & Ghoniem, A. F. (2010). Operating pressure dependence of the pressurized oxy-fuel combustion power cycle. *Energy*, 35(12), pp. 5391-5399.
- [3] Sarker, S., Nunez, J., Valdez, C., Hossain, S., Love, N., & Choudhuri, A. (2015). Preliminary design of an optically accessible high-pressure combustor. *Proceedings of the Institution of Mechanical Engineers, Part C: Journal of Mechanical Engineering Science*, 229(3), pp. 505-517.
- [4] Carroni, R., Griffin, T., Mantzaras, J., & Reinke, M. (2003). High-pressure experiments and modeling of methane/air catalytic combustion for power-generation applications. *Catalysis Today*, 83(1), pp. 157-170.
- [5] Stephen, D. T., Zhu, D., & Law, C. K. (2004). Optically accessible high-pressure combustion apparatus. *Review of scientific instruments*, 75(1), pp. 233-239.
- [6] Singla, G., Scoufflaire, P., Rolon, C., & Candel, S. (2005). Transcritical oxygen/transcritical or supercritical methane combustion. *Proceedings of the combustion institute*, 30(2), pp. 2921-2928.
- [7] Karataş, A. E., & Gülder, Ö. L. (2012). Soot formation in high pressure laminar diffusion flames. *Progress in Energy and Combustion Science*, 38(6), pp. 818-845.
- [8] Metghalchi, M. A. K. J., & Keck, J. C. (1980). Laminar burning velocity of propane-air mixtures at high temperature and pressure. *Combustion and flame*, 38, pp. 143-154.
- [9] Thomson, K. A., Gülder, Ö. L., Weckman, E. J., Fraser, R. A., Smallwood, G. J., & Snelling, D. R. (2005). Soot concentration and temperature measurements in co-annular, nonpremixed CH₄/air laminar flames at pressures up to 4 MPa. *Combustion and Flame*, 140(3), pp. 222-232.
- [10] Spalart, P. R. (2000). Strategies for turbulence modelling and simulations. *International Journal of Heat and Fluid Flow*, 21(3), pp. 252-263.
- [11] Ladeinde, F. (2009). A critical review of scramjet combustion simulation. *AIAA*, 127, 2009.
- [12] Edge, P., Gubba, S. R., Ma, L., Porter, R., Pourkashanian, M., & Williams, A. (2011). LES modelling of air and oxy-fuel pulverised coal combustion—impact on flame properties. *Proceedings of the Combustion Institute*, 33(2), pp. 2709-2716.
- [13] Zong, N., Meng, H., Hsieh, S. Y., & Yang, V. (2004). A numerical study of cryogenic fluid injection and mixing under supercritical conditions. *Physics of Fluids (1994-present)*, 16(12), pp. 4248-4261.
- [14] Sierra-Pallares, J., del Valle, J. G., García-Carrascal, P., & Ruiz, F. C. (2016). Numerical study of supercritical and transcritical injection using different turbulent Prandtl numbers: A second law analysis. *The Journal of Supercritical Fluids*, 115, pp. 86-98.

- [15] Veynante, D. (2009). Large eddy simulations of turbulent combustion. Springer Berlin Heidelberg , In Turbulence and interactions ,pp. 113-138.
- [16] Tucker, P. K., Menon, S., Merkle, C. L., Oefelein, J. C., & Yang, V. (2008). Validation of high-fidelity CFD simulations for rocket injector design. AIAA Paper : 5226
- [17] Baurle, R. A. (2004). Modeling of high speed reacting flows: established practices and future challenges. AIAA paper, pp. 267, 2004.
- [18] Wang, J., Sun, Z., Dai, Y., and Ma, S. Parametric optimization design for supercritical CO₂ power cycle using genetic algorithm and artificial neural network. Applied Energy 2010, 87(4), pp 1317-1324.
- [19] Ohji, A. (2002). Research and Development of Advanced Steam Turbine Systems Employing Ultra Super Critical Pressure Steam Conditions for Future Generations. JSME International Journal Series B Fluids and Thermal Engineering, 45(2), pp. 399-407.
- [20] Ma, Z., & Turchi, C. S. (2011, May). Advanced supercritical carbon dioxide power cycle configurations for use in concentrating solar power systems. In Proceedings of Supercritical CO₂ Power Cycle Symposium , pp. 24-25.
- [21] Oh, C. H. (2006). Development of a Supercritical Carbon Dioxide Brayton Cycle: Improving VHTR Efficiency and Testing Material Compatibility-Final Report (No. INL/EXT-06-01271). Idaho National Laboratory (INL).
- [22] Chowdhury, A. A., Bugarin, L., Badhan, A., Choudhuri, A., & Love, N. (2016). Thermodynamic analysis of a directly heated oxyfuel supercritical power system. Applied Energy, 179, 261-271.
- [23] Iwai, Y., Suzuki, M. I. Y. M. S., & Harris, D. C. M. (2015, June). Development Approach to the Combustor of Gas Turbine for Oxy-Fuel, Supercritical CO₂ Cycle. In ASME Turbo Expo 2015: Turbine Technical Conference and Exposition (pp. V009T36A013-V009T36A013). American Society of Mechanical Engineers.
- [24] U.S. Energy Information Administration - EIA - Independent Statistics and Analysis. (n.d.). Retrieved February 24, 2018, from <https://www.eia.gov/tools/faqs/faq.php?id=427&t=3>
- [25] Zhang, N., & Lior, N. Two novel oxy-fuel power cycles integrated with natural gas reforming and CO₂ capture. Energy 2008, 33(2), pp. 340-351.
- [26] Buhre, B. J. P., Elliott, L., Sheng, C. D., Gupta, R. P., & Wall, T. F. Oxy-fuel combustion technology for coal-fired power generation. Progress in energy and combustion science 2005, 31(4), pp. 283-307.
- [27] Wall, T., Liu, Y., Spero, C., Elliott, L., Khare, S., Rathnam, R., & Gupta, R. An overview on oxyfuel coal combustion—state of the art research and technology development. Chemical Engineering Research and Design 2009, 87(8), pp. 1003-1016.
- [28] Wall, T. F. Combustion processes for carbon capture. Proceedings of the combustion institute 2007, 31(1), pp. 31-47.
- [29] Glarborg, P., & Bentzen, L. L. Chemical effects of a high CO₂ concentration in oxy-fuel combustion of methane. Energy & Fuels 2008, 22(1), pp. 291-296.

- [30] White, C. M., Strazisar, B. R., Granite, E. J., Hoffman, J. S., and Pennline, H. W. Separation and capture of CO₂ from large stationary sources and sequestration in geological formations coalbeds and deep saline aquifers. *Journal of the Air & Waste Management Association* 2003, 53(6), pp. 645-715.
- [31] NETL, Current and Future Technologies for Natural Gas Combined Cycle (NGCC) Power Plants, DOE/NETL-341/061013. Pittsburgh, Pennsylvania
- [32] Chen, L., Yong, S. Z., & Ghoniem, A. F. (2012). Oxy-fuel combustion of pulverized coal: Characterization, fundamentals, stabilization and CFD modeling. *Progress in energy and combustion science*, 38(2), 156-214.
- [33] Lux, J., & Haidn, O. (2009). Effect of recess in high-pressure liquid oxygen/methane coaxial injection and combustion. *Journal of Propulsion and Power*, 25(1), pp. 24-32.
- [34] Karim, G. A. (2003). Hydrogen as a spark ignition engine fuel. *International Journal of Hydrogen Energy*, 28(5), 569-577.
- [35] Bromberg, L., Cohn, D. R., Rabinovich, A., O'brie, C., & Hochgreb, S. (1998). Plasma reforming of methane. *Energy & fuels*, 12(1), 11-18.
- [36] Cengel, Y. A. (2010). *Fluid mechanics*. Tata McGraw-Hill Education.
- [37] Ahmed, S., & Krumpelt, M. (2001). Hydrogen from hydrocarbon fuels for fuel cells. *International journal of hydrogen energy*, 26(4), pp. 291-301.
- [38] Bromberg, L., Cohn, D. R., Rabinovich, A., O'Brie, C., & Hochgreb, S. (1998). Plasma reforming of methane. *Energy & fuels*, 12(1), pp. 11-18.
- [39] Kendrick, D., Herding, G., Scouflaire, P., Rolon, C., & Candel, S. (1999). Effects of a recess on cryogenic flame stabilization. *Combustion and Flame*, 118(3), pp. 327-339.
- [40] Tripathi, A., Juniper, M., Scouflaire, P., Rolon, J. C., Durox, D., & Candel, S. (1999, June). Lox tube recess in cryogenic flames investigated using OH and H₂O emission. In *35th Joint Propulsion Conference and Exhibit* (p. 2490).
- [41] Wheeler, D. B., & Kirby, F. M. (1979). High-pressure LOX/CH₄ injector program. NASA Report.
- [42] Sanchez, L. E., Chaparro, J., Torres, S. A., Love, N. D., & Choudhuri, A. R. (2016). Development and Testing of a O₂/CH₄ Torch Igniter for Propulsion Systems. In *52nd AIAA/SAE/ASEE Joint Propulsion Conference* (p. 4975).
- [43] Launder, B. E., & Spalding, D. B. (1974). The numerical computation of turbulent flows. *Computer methods in applied mechanics and engineering*, 3(2), pp. 269-289.
- [44] Richards, G. A., Casleton, K. H., & Chorpening, B. T. (2005). CO₂ and H₂O diluted oxy-fuel combustion for zero-emission power. *Proceedings of the Institution of Mechanical Engineers, Part A: Journal of Power and Energy*, 219(2), 121-126.
- [45] Hainsworth, D., Pourkashanian, M., Richardson, A. P., Rupp, J. L., & Williams, A. (1996). The influence of carbon dioxide on smoke formation and stability in methane-oxygen-carbon dioxide flames. *Fuel*, 75(3), 393-396.

- [46] Beltrame, A., Porshnev, P., Merchan-Merchan, W., Saveliev, A., Fridman, A., Kennedy, L. A., ... & Charon, O. (2001). Soot and NO formation in methane–oxygen enriched diffusion flames. *Combustion and flame*, 124(1-2), 295-310.
- [47] Koroglu, B., Pryor, O. M., Lopez, J., Nash, L., & Vasu, S. S. (2016). Shock tube ignition delay times and methane time-histories measurements during excess CO₂ diluted oxy-methane combustion. *Combustion and flame*, 164, 152-163.
- [48] Lakshminarayanan, P. A., & Aghav, Y. V. (2010). Ignition Delay in a Diesel Engine. In *Modelling Diesel Combustion* (pp. 59-78). Springer, Dordrecht.
- [49] Chase, M. W. (1986). JANAF thermochemical tables. JANAF thermochemical tables, by Chase, MW Washington, DC: American Chemical Society; New York: American Institute of Physics for the National Bureau of Standards, c1986.. United States. National Bureau of Standards., 1.
- [50] Chowdhury, A. A., Choudhuri, A., Love, N., Kim, H., Ma, J., & Tsiava, R. (2017, June). Impact of Equation of State Model and CO₂ Diluent on Combustion Characteristics of a Directly Heated Supercritical Oxy-Fuel Combustor. In *ASME Turbo Expo 2017: Turbomachinery Technical Conference and Exposition* (pp. V04BT04A047-V04BT04A047). American Society of Mechanical Engineers.
- [51] Plocker, U., Knapp, H., & Prausnitz, J. (1978). Calculation of high-pressure vapor-liquid equilibria from a corresponding-states correlation with emphasis on asymmetric mixtures. *Industrial & Engineering Chemistry Process Design and Development*, 17(3), pp. 324-332.
- [52] Lee, B. I., & Kesler, M. G. (1975). A generalized thermodynamic correlation based on three-parameter corresponding states. *AIChE Journal*, 21(3), 510-527.
- [53] Chung, T. H., Ajlan, M., Lee, L. L., & Starling, K. E. (1988). Generalized multiparameter correlation for nonpolar and polar fluid transport properties. *Industrial & engineering chemistry research*, 27(4), pp. 671-679.
- [54] Peng, D. Y., & Robinson, D. B. (1976). A new two-constant equation of state. *Industrial & Engineering Chemistry Fundamentals*, 15(1), pp. 59-64.
- [55] Çengel, Y. A., and Boles, M. A. *Thermodynamics: An engineering approach*. 2011. (7th Ed.). McGraw-Hill Education.
- [56] Maslov, V. P. (2010). On an ideal gas related to the law of corresponding states. *Russian Journal of Mathematical Physics* 2010, 17(2), pp 240-250.

Appendix

❖ High Pressure Burner Test Preliminary CFD Analysis:

The high pressure combustor is designed to operate up to 500 kW and 20 bar. Initially a CFD analysis is conducted by recirculating carbon dioxide to observe the temperature profile inside the chamber. This section provides the details of the CFD analysis,

Table 20 Boundary condition (Preliminary CFD analysis-High pressure test)

Section	Input
General	
Type	Pressure Based
Time	Steady State
Models	
Energy	On
Viscous Model	k- ϵ (Standard)
Radiation	P-1 (On)
Species	Non-Premixed Combustion
Boundary Conditions	
Method	Axisymmetric Boundary
Inlets	<ul style="list-style-type: none"> - Fuel (Methane) Inlet Mass Flow Inlet: Primary (0.004 kg/s), Secondary (0.006 kg/s) Temperature: 300 K - Oxidizer (Oxygen) Inlet Mass Flow Inlet: Primary (0.016 kg/s), Secondary (0.0024 kg/s) Temperature: 300 K - Coolant (Carbon Dioxide) Inlet Mass Flow Inlet: 0.09 kg/s (Total) Temperature: 300 K
Outlet	Pressure Outlet: 1 bar
Wall	Combustor Wall: Convection Fluid Domain Wall: Temperature (300K)
Solution	
Method	<ul style="list-style-type: none"> - Scheme-Coupled - High Order Term Relaxation
Initialization	Primary Methane Inlet

A CFD simulation is conducted of the high pressure combustor using ANSYS Fluent commercial software. A 2D pressure based axisymmetric method is selected for the simulation. The 2D simulation method is selected to reduce the computational time. The simulation performed by adding a fluid domain at the outlet section of the combustor. The outlet of the fluid domain is defined at atmospheric pressure. The exit diameter of the combustor is manipulated to achieve 20 bar pressure inside the combustor. Figure 53(a) shows the density and the velocity contour at the inlet of the combustor. Both methane, oxygen and carbon dioxide is injected at 20 bar pressure. The mass flow inlet is used as the boundary condition. The density of methane, oxygen and carbon dioxide 20 bar and atmospheric temperature are 13.3 kg/m^3 , 25.96 kg/m^3 and 39.4 kg/m^3 . It can be seen from the contour that the density matches with the density of the corresponding fluids at 20 bar. Figure 53(b) displays the velocity at the combustor inlet. The velocity value matches with the hand calculated values with a maximum of 5% error. The error is mostly contributed by the simplified 2D geometry. Figure 54 displays the pressure contour inside the combustor. It can be seen from the figure that the pressure inside the combustor as high as 20 bar ($\approx 2000,000 \text{ Pa}$). The exit of the combustor is selected iteratively. A 20-bar combustion chamber pressure is obtained for the exit diameter of 7.6 mm. The way the combustor is designed that the maximum velocity (Mach 1) must be pass through the exit to have the combustor at 20 bar continuously. The velocity at the combustor exit can be seen in Figure 56. It can be seen from the Figure that the velocity reaches Mach 1. However, the sonic velocity doesn't match with the hand calculation. When hand calculated, the sonic velocity is found to be close to 700 m/s. This is due to the different assumption that is made during calculation. While hand calculating the sonic velocity, the temperature and fluid properties are obtained from NASA CEA software. The temperature is underestimated at NASA CEA. Therefore, the sonic velocity lower in the hand calculation.

The combustion phenomenon inside the combustor is simulated using non-premixed combustion model. The coolant is introduced by adding carbon dioxide as the secondary stream during combustion modeling. The combustion products are automatically generated using the pdf table. The temperature contour inside the combustor is shown in Figure 55. It can be seen that the

combustor wall temperature gradually increases towards the end of the combustor. Although the maximum allowable material temperature is selected to be 600 K after adding the safety factor, the near wall temperature at the end section of the combustor is still above the material operation limit. Therefore, combustor metal window is modified so that secondary carbon dioxide stream can be injected into the combustor. Furthermore, the injector faceplate cooling system also facilitate in cooling the injector face. Figure 57 and 58 are showing the mass fraction of methane and carbon dioxide inside the combustor. The combustion is modeled at stoichiometric condition. Therefore, it is presumable that all the methane will be consumed after the combustion. It is observed that more than 100% methane is consumed after the combustion. The 0.5% left over methane inside the combustor occur due to the 2D model assumption. The inlet area may not exactly match with the 3D geometry, therefore the fuel and oxidizer mass flow rate during the combustion simulation may not exactly matches with the actual mass flow. It can be seen from Figure 58 that the combustion occurs at carbon dioxide filled environment. Also, the wall is well shielded by carbon dioxide.

Figure 59 shows the streamline inside the combustor. It can be seen that there is a recirculation right at the inlet of carbon dioxide. Besides there is another recirculation zone adjacent to the injector face. The high temperature at the injector face is contributed due to this recirculation zone. Finally, it can be observed that due to the angular exit design the gases smoothly exit the combustor.

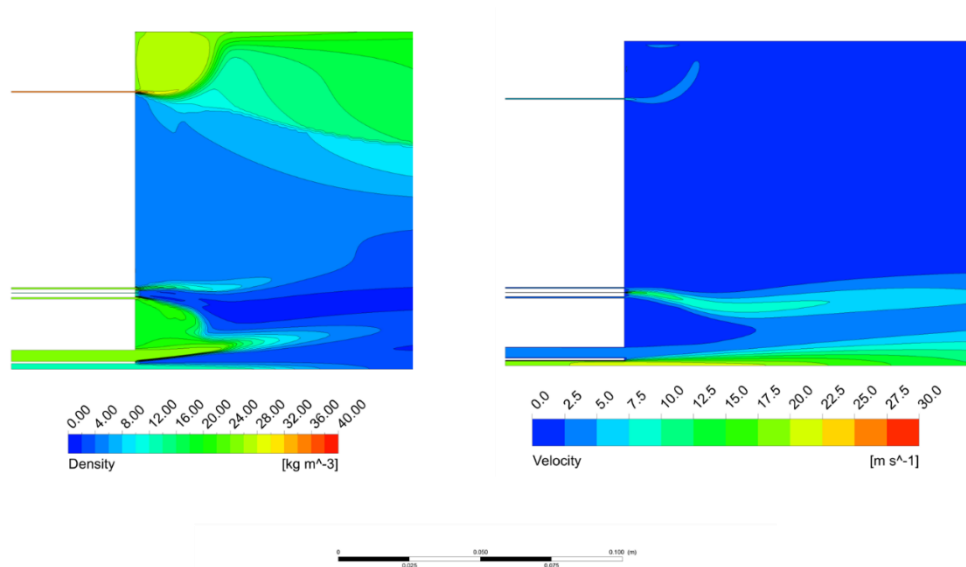


Figure 53 Density and velocity profile at the inlet of the combustor

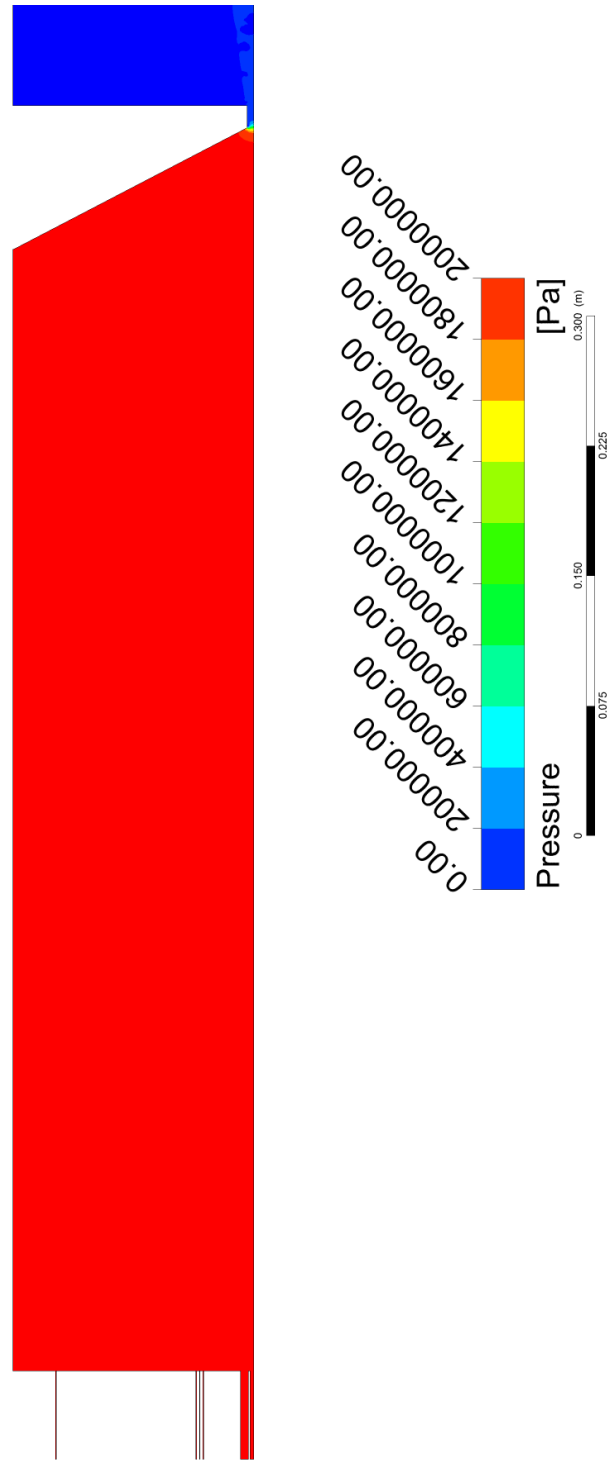


Figure 54 Pressure inside the combustor

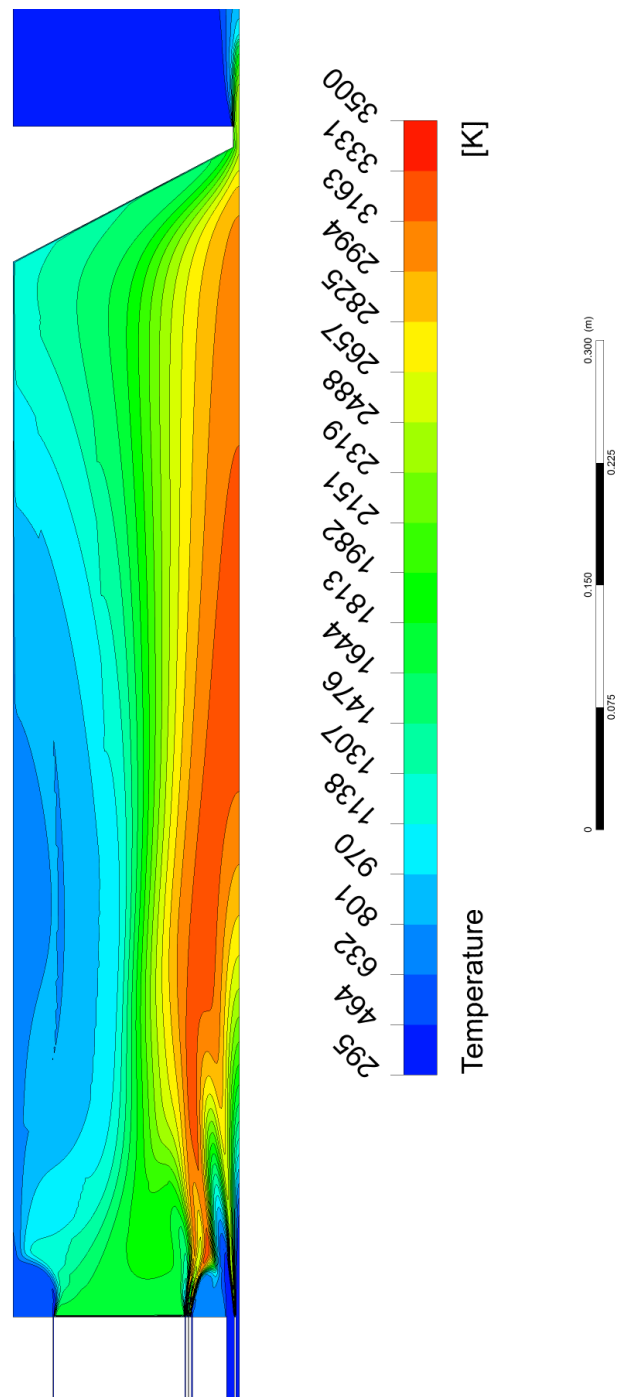


Figure 55 Temperature profile inside the combustor

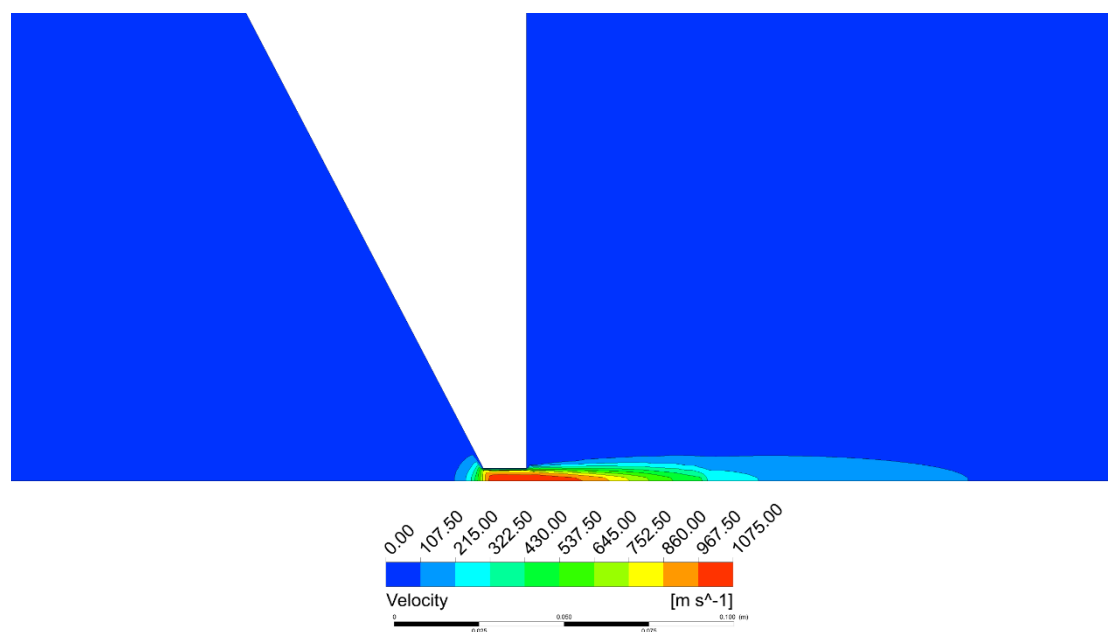


Figure 56 Exit velocity

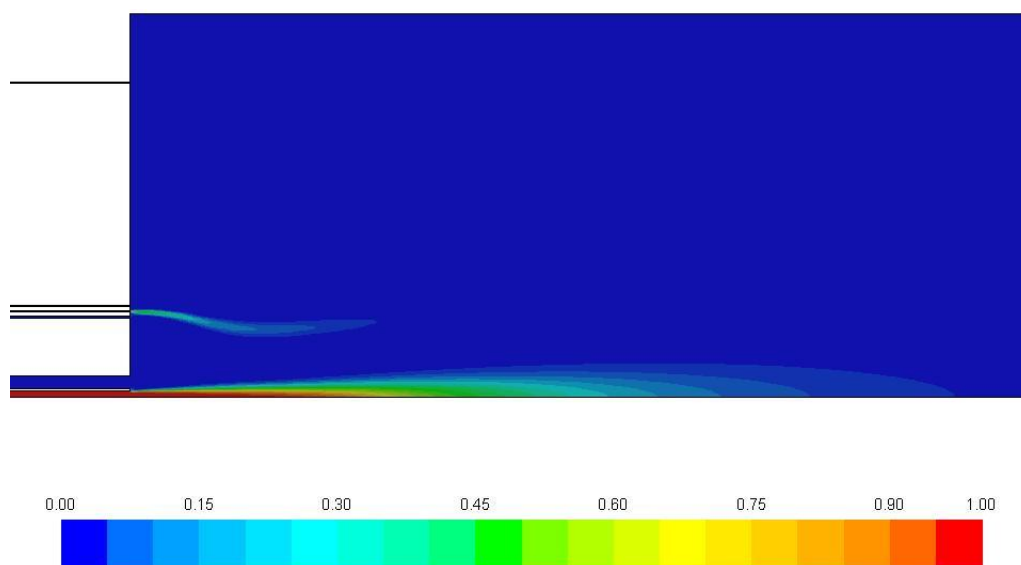


Figure 57 Methane mass fraction

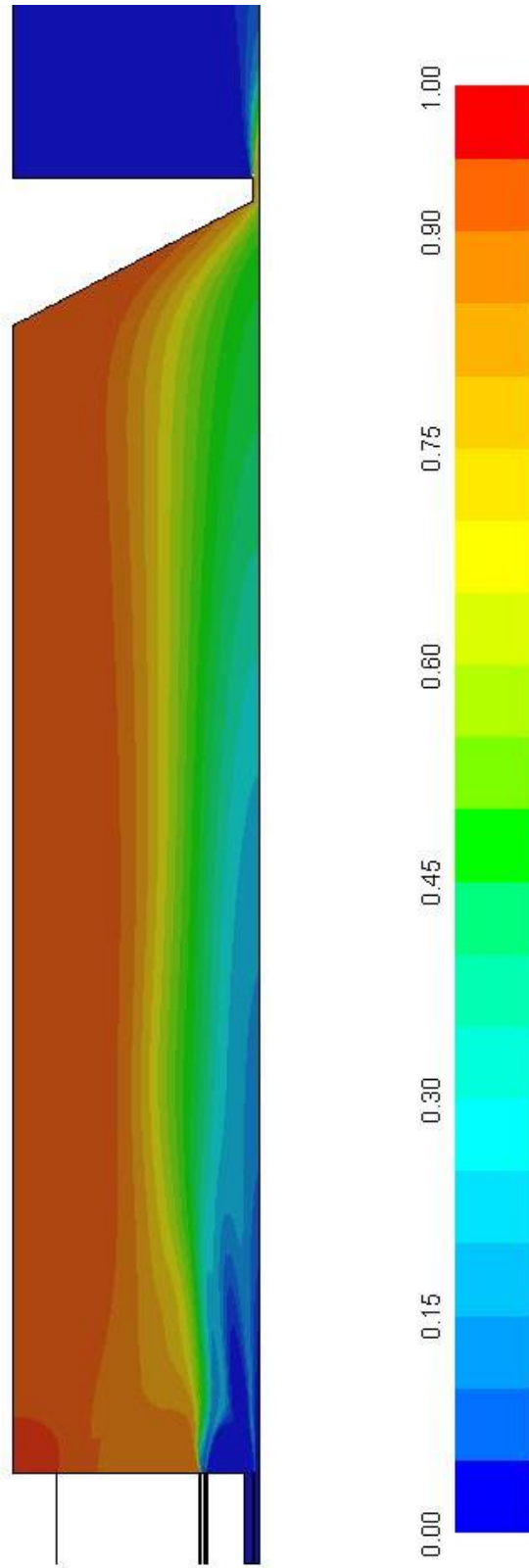


Figure 58 Carbon dioxide mass fraction

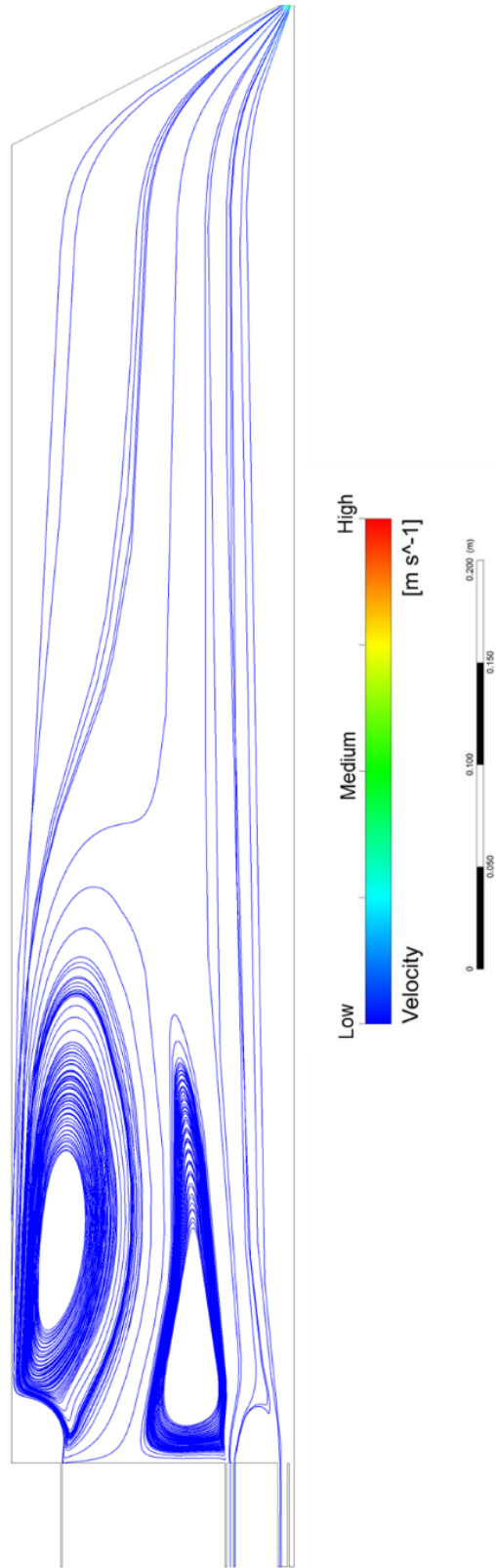


Figure 59 Streamline inside the combustor

❖ High pressure burner test procedure:



Center for Space Exploration Technology Research
University of Texas at El Paso

EFFECTIVE DATE: TBD

High Pressure Burner Test Procedure

APPROVALS

Arifur Chowdhury
Team Lead/ Originator

Date

Charles Hill
cSETR Safety Manager

Date

Luz Bugarin
cSETR Lab Manager

Date:

Version 6.0

Updated: October 18, 2017

Emergency Contact Information

- If any personnel injury occurs, the following is offered as a guide:
- Move injured personnel only if necessary to prevent further injury.
- Emergency contacts:
 - UTEP Police (915)747-5611
 - EH&S (915) 747-7124
 - Luz Bugarin (915) 747-7398

► **Section 1: INTRODUCTION**

The purpose of this experimental study is to demonstrate a high pressure (< 20 bar) oxy-methane combustion test up to/ at ≈ 250 kW. Through the experimental tasks the team will learn how to design and operate a high pressure oxy-combustion system. The ultimate goal is to develop a 300 bar oxy-methane laboratory scale combustor for power generation purposes.

The operating parameters for the test can be summarized as following:

Fuel: Methane

Oxidizer: oxygen

Diluent: Carbon dioxide

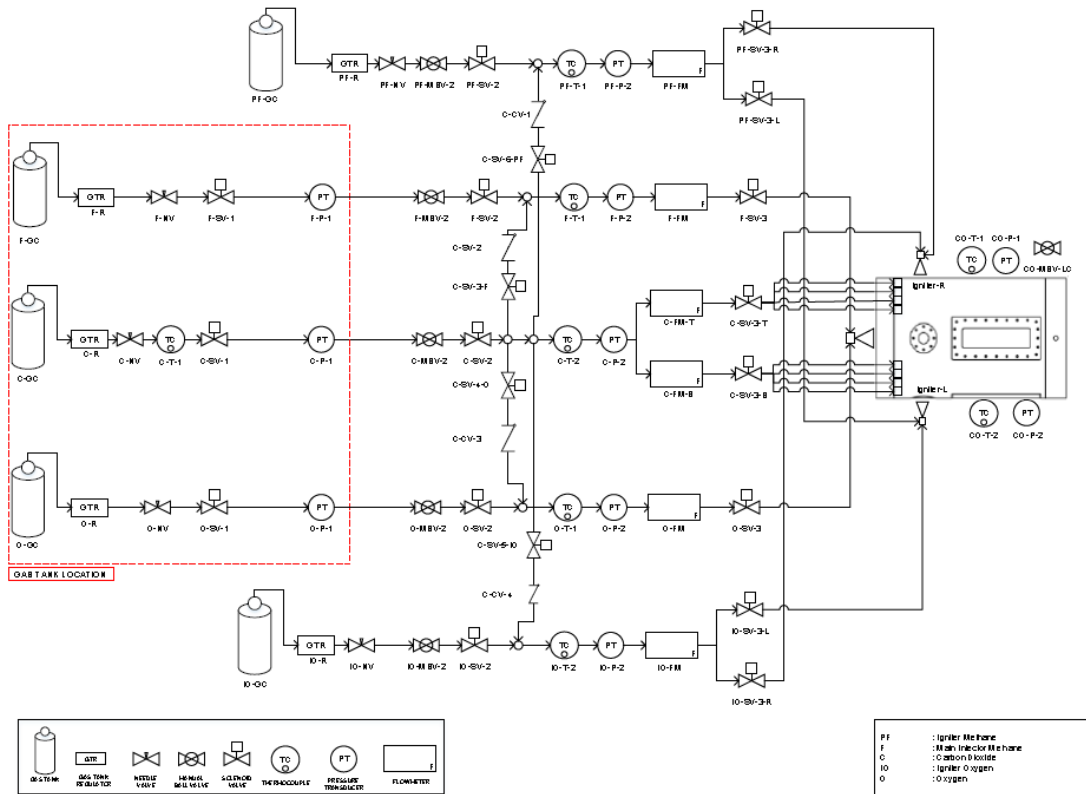
Pressure: up to 300 psi

Power Input: up to 250 kW

Duration: 30 seconds

The experiment will be conducted at Fabens research facility. The test apparatus includes a combustor, fluid delivery system and gas tanks. The piping and instrumentation diagram for the fluid delivery system can be found in section 2. The fluid delivery system will be remotely controlled using DAQ system and LabVIEW. The leak check of the fluid delivery system has already been performed. To confirm a safe operation, the DAQ system and LabVIEW system check will be performed before the test. Afterwards the igniter test will be performed.

► **Section 2: PIPING AND INSTRUMENTATION DIAGRAM**



HIGH PRESSURE BURNER TEST P&ID

AUTHOR: ARIFUR ROHWDHURY DATE: 26-SEPT-2017

Figure 1 P&ID

Table 1 Instrumentation list

Schematic Notation	Part Type	DATA COLLECTION RATE
IGNITER -OXYGEN		
IO-GC	Gas Cylinder	
IO-R	Gas Tank Regulators	
IO-NV	Needle Valve	
IO-MBV-2	Ball Valve	
IO-SV-2	Solenoid Valve	
IO-T-1	Thermocouple	1 Hz
IO-P-2	Pressure Transducer	10 Hz
IO-FM	Flowmeter	1 Hz
IO-SV-3-L	Solenoid Valve	
IO-SV-3-R	Solenoid Valve	
MAIN INJECTOR-OXYGEN		
O-GC	Gas Cylinder	
O-R	Gas Tank Regulators	
O-NV	Needle Valve	
O-SV-1	Solenoid Valve	
O-MBV-1	Ball Valve	
O-P-1	Pressure Transducer	10 Hz
O-MBV-2	Ball Valve	
O-SV-2	Solenoid Valve	
O-T-1	Thermocouple	1 Hz
O-P-1	Pressure Transducer	10 Hz
O-FM	Flowmeter	1 Hz
O-SV-3-MI	Solenoid Valve	
CARBON DIOXIDE		
C-GC	Gas Cylinder	
C-R	Gas Tank Regulators	
C-T-1	Thermocouple	1 Hz
C-SV-1	Solenoid Valve	
C-NV	Needle Valve	
C-P-1	Pressure Transducer	10 Hz
C-MBV-2	Ball Valve	
C-SV-2	Solenoid Valve	
C-SV-4-O	Solenoid Valve	
C-SC-6-PF	Solenoid Valve	
C-SV-5-IO	Solenoid Valve	
C-SV-3-F	Solenoid Valve	
C-T-2	Thermocouple	1 Hz
C-P-2	Pressure Transducer	10 Hz
C-FM-T	Flowmeter	1 Hz
C-FM-B	Flowmeter	1 Hz
C-SV-3-T	Solenoid Valve	
C-SV-3-B	Solenoid Valve	

MAIN INJECTOR - METHANE		
F-GC	Gas Cylinder	
F-R	Gas Tank Regulators	
F-NV	Needle Valve	
F-SV-1	Solenoid Valve	
F-MBV-1	Ball Valve	
F-P-1	Pressure Transducer	10 Hz
F-MBV-2	Ball Valve	
F-SV-2	Solenoid Valve	
F-T-1	Thermocouple	1 Hz
F-P-2	Pressure Transducer	10 Hz
F-FM	Flowmeter	1 Hz
F-SV-3-MI	Solenoid Valve	
IGNITER - METHANE		
PF-GC	Gas Cylinder	
PF-R	Gas Tank Regulators	
PF-NV	Needle Valve	
PF-MBV-2	Ball Valve	
PF-SV-2	Solenoid Valve	
PF-T-1	Thermocouple	1 Hz
PF-P-2	Pressure Transducer	10 Hz
PF-FM	Flowmeter	1 Hz
PF-SV-3-L	Solenoid Valve	
PF-SV-3-R	Solenoid Valve	
COMBUSTOR		
CO-T-1	Thermocouple	1 Hz
CO-T-1	Thermocouple	1 Hz
CO-P-1	Pressure Transducer	10 Hz
CO-P-1	Pressure Transducer	10 Hz
RV	Relief Valve	

► **Section 3: PRE-TEST PROCEDURE**

▪ **Safety Considerations**

These experiments pose a series of hazards to personnel and equipment. Refer to the Hazards Analysis (Section 7) presented in this section for a list of hazards associated with the operation of this experimental setup. Use extreme caution when operating pressure system and high voltage electrical systems.

Use approved personal protective equipment (PPE):

- Eyes: Safety glasses shall be worn at all times. Safety glasses may be found at the entrance of the research facility. Replacements may be ordered from <http://www.homedepot.com/p/3M-Clear-Frame-with-Clear-Scratch-Resistant-Lenses-Indoor-Safety-Glasses-90551-00000B/202552394>



- Ears: Earplugs or earmuffs shall be used where uncomfortable noise levels occur during operations. These may be found at the entrance of the research facility.



- Hands: When handling high voltage connections, insulating gloves should be worn. When handling seeding particles, latex gloves must be worn. These may be found at the entrance of the research facility.



- Skin: Lab coats must be worn at all times inside the research facilities.

Pressure must be relieved from the system before removing any test article or line component. All pressure gauges should read 0 psig before attempting to remove a component.

All personnel shall wear approved personal protective equipment for the operation being performed as defined below:

▪ **Conduction of Tests**

Eyes	Safety glasses with side shields shall be worn. Visiting personnel shall wear safety glasses with side shields.
Feet	Steel-toe boots must be worn at all times while inside the research facilities.

Body Lab coats must be worn at all times during experimental procedures

Ears Earplugs or earmuffs shall be used as required.

- If any personnel injury occurs, the following is offered as a guide:
- Move injured personnel only if necessary to prevent further injury.
- Emergency contacts:
 - UTEP Police (915)747-5611
 - EH&S (915) 747-7124
 - Luz Bugarin (915) 747-7398

▪ **Hazard Analysis**

Severity Level	
1	Minor
2	Moderate
3	Significant
4	Catastrophic

Event Frequency	
1	Unlikely
2	Infrequent
3	Frequent

	System	Hazard	Severity	Likelihood	Mitigation
1	Feed Systems	Overpressure	2 - Moderate	1 - Unlikely	Relief valves will be installed in the delivery lines (Refer to Figure 1).
2	Feed Systems	Valve failure to open	2 - Moderate	2 - Infrequent	Molex electrical connectors will be used for secure connection. Power supplies and valve operation tested prior to experimental procedures
3	Feed Systems	Valve failure to close	2 - Moderate	2 - Infrequent	Emergency stop switch to cut power to non-responsive valves will be installed in the experimental setup.
4	Combustor	Quartz Window cracking	2 - Moderate	2 - Infrequent	Keep combustor pressure below the maximum operating pressure of the quartz window. Two pressure valves will be installed to prevent combustor from over pressurization.
6	Combustor	Gas accumulation	3 - Significant	1 - Unlikely	Two pressure relief valves will be installed to prevent combustor from gas accumulation.
7	Combustor	Failure to ignite	2 - Moderate	2 - Infrequent	Pilot flame on before oxy/methane delivery. Carbon dioxide will be injected into the combustor in case of any emergency.
8	Combustor	Detonation	4 - Catastrophic	1 - Unlikely	Carbon dioxide will be injected into the combustor in case of any emergency. Human presence will be sufficiently far to prevent any physical accident.
9	Pilot Flame	Methane leak	3 - Significant	1 - Unlikely	Leak check conducted prior to experimentation
10	Pilot Flame	Failure to ignite	3 - Significant	2 - Infrequent	Sparking system functionality will be checked prior to experimentation. Carbon dioxide will be injected into the combustor in case of any emergency.
12	Control	LabVIEW failure (failure to initiate, freezing,	3 - Significant	2 - Infrequent	LabVIEW software functionality will be tested prior to initiating experimental procedures. Upon freezing, stop experimental procedures and troubleshoot.

		failure to run vi) Computer failure (failure to turn on, freezing, failure to open laser software)			
13	Control		3 - Significant	1 - Unlikely	Computer functionality is tested prior to initiating experimental procedures. Upon freezing, stop experimental procedures and troubleshoot.
14	Power	Power outage	3 - Significant	1 - Unlikely	Normally Closed valves will be used in the system.
15	Power	Electric shock	2 - Moderate	1 - Unlikely	High voltage electrical gloves are part of personnel.
16	Ignition	Failure to spark	1 - Minor	1 - Unlikely	Battery voltage will be checked. Igniter will be tested before starting the pilot flame.

▪ **DAQ System and LabVIEW Operation Verification Process**

*The LabVIEW operation verification will be performed inside the HQ site.

- ✓ **The operability of the solenoid valves will be evaluated by hearing the 'click' sound while opening.** Solenoid valves are NORMALLY CLOSED when not powered.
- ✓ **The operability of the pressure transducers will be evaluated by assessing the pressure reading at ambient condition (0psi) and pressurized condition (150 ± 5 psi).**

Solenoid Valve Check Procedure

- _____ Verify 'HPC_LabVIEW_Control_Acquisition.vi' is running in LabVIEW on the DAQ computer.

(All solenoid (refer to schematics in Figures 1) must be in the CLOSED position prior to starting LabVIEW verifications procedures. Solenoid valves are NORMALLY CLOSED when not powered.)*

- _____ Open IO-SV-2 using LabVIEW and check the 'click' sound. If 'click' sound doesn't occur then proceed to the followings:
 - _____ Check the wire connections
 - _____ Check LabVIEW programming
- _____ Open IO-SV-3-L using LabVIEW and check the 'click' sound. If 'click' sound doesn't occur then proceed to the followings:
 - _____ Check the wire connections
 - _____ Check LabVIEW programming
- _____ Open IO-SV-3-R using LabVIEW and check the 'click' sound. If 'click' sound doesn't occur then proceed to the followings:
 - _____ Check the wire connections
 - _____ Check LabVIEW programming
- _____ Open O-SV-1 using LabVIEW and check the 'click' sound. If 'click' sound doesn't occur then proceed to the followings:
 - _____ Check the wire connections
 - _____ Check LabVIEW programming
- _____ Open O-SV-2 using LabVIEW and check the 'click' sound. If 'click' sound doesn't occur then proceed to the followings:
 - _____ Check the wire connections
 - _____ Check LabVIEW programming
- _____ Open O-SV-3 using LabVIEW and check the 'click' sound. If 'click' sound doesn't occur then proceed to the followings:
 - _____ Check the wire connections
 - _____ Check LabVIEW programming
- _____ Open C-SV-1 using LabVIEW and check the 'click' sound. If 'click' sound doesn't occur then proceed to the followings:
 - _____ Check the wire connections
 - _____ Check LabVIEW programming
- _____ Open C-SV-2 using LabVIEW and check the 'click' sound. If 'click' sound doesn't occur then proceed to the followings:
 - _____ Check the wire connections
 - _____ Check LabVIEW programming
- _____ Open C-SV-3-T using LabVIEW and check the 'click' sound. If 'click' sound doesn't occur then proceed to the followings:
 - _____ Check the wire connections
 - _____ Check LabVIEW programming
- _____ Open C-SV-3-B using LabVIEW and check the 'click' sound. If 'click' sound doesn't occur then proceed to the followings:
 - _____ Check the wire connections
 - _____ Check LabVIEW programming

- _____ Open C-SV-3-F using LabVIEW and check the 'click' sound. If 'click' sound doesn't occur then proceed to the followings:
 - _____ Check the wire connections
 - _____ Check LabVIEW programming
- _____ Open C-SV-4-O using LabVIEW and check the 'click' sound. If 'click' sound doesn't occur then proceed to the followings:
 - _____ Check the wire connections
 - _____ Check LabVIEW programming
- _____ Open C-SV-5-IO using LabVIEW and check the 'click' sound. If 'click' sound doesn't occur then proceed to the followings:
 - _____ Check the wire connections
 - _____ Check LabVIEW programming
- _____ Open C-SV-6-PF using LabVIEW and check the 'click' sound. If 'click' sound doesn't occur then proceed to the followings:
 - _____ Check the wire connections
 - _____ Check LabVIEW programming
- _____ Open F-SV-1 using LabVIEW and check the 'click' sound. If 'click' sound doesn't occur then proceed to the followings:
 - _____ Check the wire connections
 - _____ Check LabVIEW programming
- _____ Open F-SV-2 using LabVIEW and check the 'click' sound. If 'click' sound doesn't occur then proceed to the followings:
 - _____ Check the wire connections
 - _____ Check LabVIEW programming
- _____ Open F-SV-3 using LabVIEW and check the 'click' sound. If 'click' sound doesn't occur then proceed to the followings:
 - _____ Check the wire connections
 - _____ Check LabVIEW programming
- _____ Open PF-SV-2 using LabVIEW and check the 'click' sound. If 'click' sound doesn't occur then proceed to the followings:
 - _____ Check the wire connections
 - _____ Check LabVIEW programming
- _____ Open PF-SV-3-L using LabVIEW and check the 'click' sound. If 'click' sound doesn't occur then proceed to the followings:
 - _____ Check the wire connections
 - _____ Check LabVIEW programming
- _____ Open PF-SV-3-R using LabVIEW and check the 'click' sound. If 'click' sound doesn't occur then proceed to the followings:
 - _____ Check the wire connections
 - _____ Check LabVIEW programming

Pressure Transducer Check Procedure (Ambient Condition)

- _____ Check PF-P-2 reads ambient pressure (0 + 1 psi). If it doesn't read the accurate pressure then proceed to the followings:
 - _____ Check the wire connections
 - _____ Check LabVIEW programming
- _____ Check F-P-1 reads ambient pressure (0 + 1 psi). If it doesn't read the accurate pressure then proceed to the followings:
 - _____ Check the wire connections
 - _____ Check LabVIEW programming
- _____ Check F-P-2 reads ambient pressure (0 + 1 psi). If it doesn't read the accurate pressure then proceed to the followings:
 - _____ Check the wire connections
 - _____ Check LabVIEW programming
- _____ Check C-P-1 reads ambient pressure (0 + 1 psi). If it doesn't read the accurate pressure then proceed to the followings:

- o ☐ Check the wire connections
 - o ☐ Check LabVIEW programming
- ☐ Check C-P-2 reads ambient pressure (0 ± 1 psi). If it doesn't read the accurate pressure then proceed to the followings:
 - o ☐ Check the wire connections
 - o ☐ Check LabVIEW programming
- ☐ Check O-P-1 reads ambient pressure (0 ± 1 psi). If it doesn't read the accurate pressure then proceed to the followings:
 - o ☐ Check the wire connections
 - o ☐ Check LabVIEW programming
- ☐ Check O-P-2 reads ambient pressure (0 ± 1 psi). If it doesn't read the accurate pressure then proceed to the followings:
 - o ☐ Check the wire connections
 - o ☐ Check LabVIEW programming
- ☐ Check IO-P-2 reads ambient pressure (0 ± 1 psi). If it doesn't read the accurate pressure then proceed to the followings:
 - o ☐ Check the wire connections
 - o ☐ Check LabVIEW programming

Pressure Transducer Check Procedure (Pressurized Condition 150 psi)

(*Pressurize igniter oxygen feed line up to 150 psi)

- ☐ Check IO-P-2 reads pressure (150 ± 5 psi). If it doesn't read the accurate pressure then proceed to the followings:
 - o ☐ Check the wire connections
 - o ☐ Check LabVIEW programming

(*Pressurize main injector oxygen feed line up to 150psi)

- ☐ Check O-P-1 reads pressure (150 ± 5 psi). If it doesn't read the accurate pressure then proceed to the followings:
 - o ☐ Check the wire connections
 - o ☐ Check LabVIEW programming
- ☐ Check O-P-2 reads pressure (150 ± 5 psi). If it doesn't read the accurate pressure then proceed to the followings:
 - o ☐ Check the wire connections
 - o ☐ Check LabVIEW programming

(*Pressurize carbon dioxide feed line up to 150psi)

- ☐ Check C-P-1 reads pressure (150 ± 5 psi). If it doesn't read the accurate pressure then proceed to the followings:
 - o ☐ Check the wire connections
 - o ☐ Check LabVIEW programming
- ☐ Check C-P-2 reads pressure (150 ± 5 psi). If it doesn't read the accurate pressure then proceed to the followings:
 - o ☐ Check the wire connections
 - o ☐ Check LabVIEW programming

(*Pressurize methane feed line up to 150psi)

- ☐ Check F-P-1 reads pressure (150 ± 5 psi). If it doesn't read the accurate pressure then proceed to the followings:
 - o ☐ Check the wire connections
 - o ☐ Check LabVIEW programming
- ☐ Check F-P-2 reads pressure (150 ± 5 psi). If it doesn't read the accurate pressure then proceed to the followings:
 - o ☐ Check the wire connections
 - o ☐ Check LabVIEW programming

(*Pressurize igniter methane feed line up to 150psi)

- ☐ Check PF-P-2 reads pressure (150 ± 5 psi). If it doesn't read the accurate pressure then proceed to the followings:
 - o ☐ Check the wire connections
 - o ☐ Check LabVIEW programming

▪ **Emergency OFF Check Procedure (Automatic Sequence)**

*Must be checked before the test

*Emergency shut down procedure:

- ✓ The emergency shut down procedure is an automatic procedure which can be activated by the '**KILL SWITCH**'
- ✓ The '**KILL SWITCH**' is located at the remote-control station and LabVIEW program

Red Line Limits

- ✓ Pressure: 400 psi
- ✓ Temperature (Feed Line): 315 K
- ✓ Temperature (Combustor): 600 K

Emergency Sequence

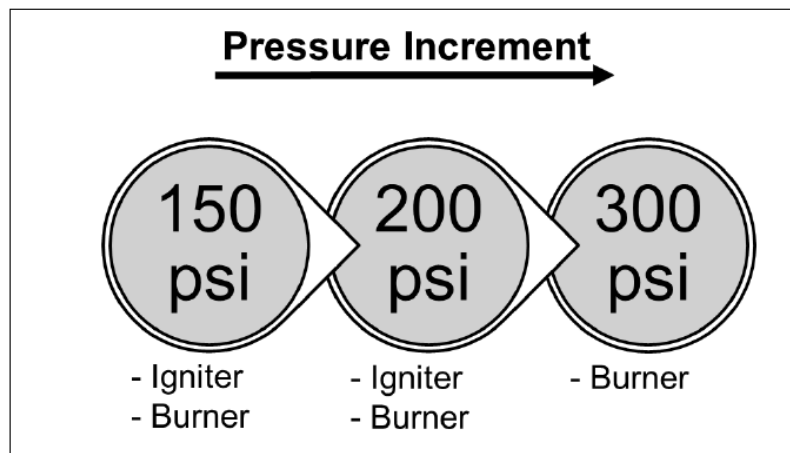
* Make sure C-MBV-2 is OPEN prior to the test

In the case of emergency '**ACTIVATE**' the '**KILL SWITCH**' and it will initiate following automatic sequence:

- _____ Close PF-SV-2
(Closes methane solenoid valve at the gas tank trailer)
- _____ Close IO-SV-2
(Closes oxygen solenoid valve at the gas tank trailer)
- _____ Close F-SV-1
(Closes methane solenoid valve at the feed system trailer)
- _____ Close O-SV-1
(Closes oxygen solenoid valve at the feed system trailer)
- _____ Close F-SV-2
(Closes methane solenoid valve at the feed system trailer)
- _____ Close O-SV-2
(Closes oxygen solenoid valve at the feed system trailer)
- _____ OPEN F-SV-3
(Opens main injector methane solenoid valve at the feed system trailer)
- _____ OPEN O-SV-3
(Opens main injector oxygen solenoid valve at the feed system trailer)
- _____ OPEN C-SV-1
(Opens oxygen solenoid valve at the gas tank trailer)
- _____ OPEN C-SV-2
(Opens oxygen solenoid valve at the gas tank trailer)
- _____ OPEN C-SV-3-F
(Deliver carbon dioxide through the main injector methane line)
- _____ OPEN C-SV-4-O
(Deliver carbon dioxide through the main injector oxygen line)
- _____ Open C-SV-6-PF
(Deliver carbon dioxide through the igniter methane line)
- _____ Open C-SV-5-IO
(Deliver carbon dioxide through the igniter oxygen line)

* **Manually turn OFF the auto sequence**

► **Section 4: TEST PLAN**



The team is planning to achieve the combustor pressure goal (300 psi) in three different stages. The igniter is currently operating at 150 psi. The first milestone will be to achieve the burner inlet pressure up to 150 psi. It needs to be noted that, the igniter will be turned off after the burner flame is ON. The operation time for the igniter is not more than 3s. At the beginning, the team will conduct the experiment by keeping the end cap open. Once the team achieve experience with the 150 psi burner flame ignition, the combustor end cap will be mounted to achieve the combustor pressure. The chamber pressure will be set by manipulating the exit area. The second milestone will be to achieve combustion chamber pressure up to 200 psi. During this time, the igniter inlet pressure will be 200 psi. And, the final goal will be to achieve combustion chamber pressure 300 bar. The technical approach can be summarized as following:

- Each Test Duration: 10s
- Test Approach:
 - ✓ Scenario 1: End Cap Open
 - ✓ Scenario 2: End Cap Close- Exit Cap -OFF
 - ✓ Scenario 3: End Cap Close- Exit Cap –ON
- Test Repeatability: 3 times (each case)

Detailed operating pressure distribution will be:

Burner		Igniter		Carbon Dioxide
Methane line Pressure (psig)	Oxygen line Pressure (psig)	Methane line Pressure (psig)	Oxygen line Pressure (psig)	Carbon Dioxide line Pressure (psig)
30	30	150	150	150
40	40	150	150	150
50	50	150	150	150
60	60	150	150	150
70	70	150	150	150
80	80	150	150	150
90	90	150	150	150
100	100	150	150	150
110	110	150	150	150

120	120	150	150	150
130	130	150	150	150
140	140	150	150	150
150	150	150	150	150
Milestone 1				
160	160	200	200	200
170	170	200	200	200
180	180	200	200	200
190	190	200	200	200
200	200	200	200	200
Milestone 2				
200	200			200
210	210			210
220	220			220
230	230			230
240	240			240
250	250			250
260	260			260
270	270			270
280	280			280
290	290			290
300	300			300
Milestone 3				

- The operating pressure of the igniter for milestone 3 will be determined after successful completion of milestone 2.
- The power input will be calculated based on the line pressure and volumetric flowrate.
- The team will wait 2 minutes between two tests.
- The system will be purged at the end of the day.

► **Section 5: TEST PROCEDURE**

(*All valves, solenoid and manual valves (refer to schematics in Figures 1) must be in the CLOSED position prior to starting experimental procedures. Solenoid valves are Normally Closed when not powered.)

▪ **Safety Walk Down Prior To Testing**

- _____Secure test area by placing safety barricades in front of the test setup
- _____Verify only Test Personnel are present in the test area prior to experimental procedure
- _____Verify all personnel inside the laboratory are wearing the proper PPE.
 - _____Safety glasses
 - _____Ear muffs (optional)
 - _____Lab coats
 - _____Steel toe boots
- _____Verify all Subsystem Pre-check Procedures have been completed.

▪ **Initial System Inspection**

- _____Visually inspect the test setup to be configured per schematics in Figure 1.
- _____Components are missing and/or misplaced or disconnected. (Stop procedure, check components and troubleshoot if necessary, then start from Step 1)
- _____Ask all personnel that will not be part of the test to leave the test area while experiments are being conducted.
- _____Verify attachment and anchoring of line components and interfaces (interface bolts and tube/pipe fittings) by using a wrench to tighten any loose fittings/connections.
- _____Verify that all gas cylinders are properly strapped to the cylinder rack
- _____Inspection of ignition spark plug wiring to verify the wiring is accurate
- _____Inspection of combustor quartz windows (Check for cracks and or fractures in windows – Visual inspection)
- _____Verify LabVIEW computer functionality by checking that it is powered and the LabVIEW software starts and can open 'HPC_LabVIEW_Control_Acquisition.vi'.
- _____Verify LabVIEW program functionality by opening the test VI and attempting to run to verify that it does.

▪ **Gas Tank Pressurization**

- _____OPEN IO-GC
(Opens igniter oxygen gas cylinder)
- _____Set IO-GC to 105 ± 5 psi
(Set igniter oxygen gas cylinder to 105 ± 5 psi)
- _____OPEN PF-GC to
(Opens igniter methane gas cylinder)
- _____Set PF-GC to 80 ± 5 psi
(Set igniter methane gas cylinder to 150 ± 5 psi)
- _____OPEN C-GC to
(Opens carbon dioxide gas cylinder)
- _____Set C-GC to $___ \pm 5$ psi
(Set carbon dioxide gas cylinder to $___ \pm 5$ psi)
- _____OPEN O-GC to
(Opens carbon dioxide gas cylinder)
- _____Set O-GC to $___ \pm 5$ psi
(Set carbon dioxide gas cylinder to $___ \pm 5$ psi)
- _____OPEN F-GC to
(Opens carbon dioxide gas cylinder)
- _____Set F-GC to $___ \pm 5$ psi
(Set carbon dioxide gas cylinder to $___ \pm 5$ psi)

▪ **Test Sequence**

		Status	Time Step	Run Time
Priming Sequence (Manual)				
Step 1	_____Open IO-SV-2			5s
Step 2	_____Close IO-SV-2			
Step 3	_____Open PF-SV-2			5s
Step 4	_____Close PF-SV-2			
Step 5	_____Open F-SV-1			5s
Step 6	_____Open F-SV-2			5s
Step 7	_____Close F-SV-2			
Step 8	_____Open O-SV-1			5s
Step 9	_____Open O-SV-2			5s
Step 10	_____Close O-SV-2			
Step 11	_____Open C-SV-1			
Step 12	_____Open C-SV-2			
Step 13	_____Open C-SV-3			5s
Step 14	_____Close C-SV-3			
Step 15	_____Turn ON Spark Plug			
Step 16	_____Turn OFF Spark Plug			
Step 17	_____Open O-SV-2			
Step 18	_____Open O-SV-3			5s
Step 19	_____Close O-SV-3			
Step 20	_____Turn ON Spark Plug			
Step 21	_____Turn OFF Spark Plug			
Test Sequence (Auto)			(0s-36s)	
Step 22	All Close (Sparker ON)			0s
Step 23	OPEN IO-SV-2, PF-SV-2, F-SV-2, O-SV-2, C-SV-2			1s
Step 24	OPEN IO-SV-3-R			2s
Step 25	OPEN PF-SV-3-R	Ignition Flame ON		3-4s
Step 26	OPEN O-SV-3, F-SV-3 (Burner Flame ON)	Ignition Flame ON, Burner Flame ON		5-6s
Step 27	CLOSE (PF-SV-3-R, IO-SV-3-R)	Ignition Flame OFF, Burner Flame ON		5-35s
Step 28	CLOSE (O-SV-3, F-SV-3)	Burner Flame OFF		36s
Step 29	CLOSE (O-SV-1, F-SV-1, O-SV-2, F-SV-2)	Test End		

► **Section 6: POST-TEST PROCEDURE**

▪ **Purging Sequence (Automatic Sequence)**

- _____ Close PF-SV-2
(Closes methane solenoid valve at the gas tank trailer)
- _____ Close IO-SV-2
(Closes oxygen solenoid valve at the gas tank trailer)
- _____ Close F-SV-1
(Closes methane solenoid valve at the feed system trailer)
- _____ Close O-SV-1
(Closes oxygen solenoid valve at the feed system trailer)
- _____ Close F-SV-2
(Closes methane solenoid valve at the feed system trailer)
- _____ Close O-SV-2
(Closes oxygen solenoid valve at the feed system trailer)
- _____ OPEN F-SV-3
(Opens main injector methane solenoid valve at the feed system trailer)
- _____ OPEN O-SV-3
(Opens main injector oxygen solenoid valve at the feed system trailer)
- _____ OPEN C-SV-1
(Opens oxygen solenoid valve at the gas tank trailer)
- _____ OPEN C-SV-2
(Opens oxygen solenoid valve at the gas tank trailer)
- _____ OPEN C-SV-3-F
(Deliver carbon dioxide through the main injector methane line)
- _____ OPEN C-SV-4-O
(Deliver carbon dioxide through the main injector oxygen line)
- _____ Open C-SV-6-PF
(Deliver carbon dioxide through the igniter methane line)
- _____ Open C-SV-5-IO
(Deliver carbon dioxide through the igniter oxygen line)

* Manually turn OFF the auto sequence

_____ 0 _____

❖ **Comparison Among Different Real Gas Model:**

An analysis is conducted to make a comparison among ideal gas model, Peng Robinson EOS and Lee Kesler EOS. This section provides the details of the CFD analysis.

Table 21 Boundary Conditions (Comparison of EOS)

Section	Input
General	
Type	Pressure Based
Time	Steady State
Models	
Energy	On
Viscous Model	k-ε Model
Wall Function	Standard Wall Function
Turbulence Chemistry Interaction	Eddy Dissipation
Radiation	Off
Species	Species Transport (One Step Chemistry- $\text{CH}_4 + 2\text{O}_2 = 2\text{H}_2\text{O} + \text{CO}_2$)
Materials	
Materials	CH_4 , O_2 , H_2O , CO_2
Density	<ul style="list-style-type: none"> - Lee Kesler Plocker EOS - Peng Robinson EOS - Ideal Gas Law
Boundary Conditions	
Method	Symmetry Boundary
Inlets	<ul style="list-style-type: none"> - Fuel Inlet Mass Flow Inlet: 0.0025 kg/s Temperature: 400 K - Oxidizer Inlet Mass Flow Inlet: 0.01 kg/s Temperature: 300 K - Diluent Inlet Mass Flow Inlet: 0.1586 kg/s (Total) Temperature: 935 K
Outlet	Pressure Outlet: 300 bar
Wall	Adiabatic Wall
Solution	
Method	<ul style="list-style-type: none"> - Scheme-Simple - High Order Term Relaxation
Initialization	Hybrid

The proposed geometry for a 1 MW supercritical combustor is presented in Figure 36. The firing input is equally distributed among the 8 injectors, Figure 60(a). Therefore, each injector provides 125 kW of power input into the combustor. Since the combustor is symmetrically divided,

for computational simplicity one-eighth of the combustor is simulated in a 3D domain, Fig. 60(b). A shear co-axial injector will deliver methane and oxygen into the combustor. The injector is designed such a way that the methane will be injected from the center port where oxygen will be injected from the outer port. The fuel and oxidizer will mix via shear force and combust. The carbon dioxide will be delivered into the combustion chamber to reduce the oxy-flame temperature. There are two carbon dioxide inlets, the center inlet and the circumferential inlet. The circumferential carbon dioxide will protect the wall from experiencing high temperature. This particular paper focuses on the comparison of combustion and the mixing of the diluents inside the combustion chamber. The fluid domain dimensions for the simulation can be seen in Figure 61. Figure 61(a) demonstrates the complete fluid domain where Figure 61(c) shows the cross-section view of that domain. Figure 61(b) shows the inlet section of the combustor. The dimensions for the domain geometry is provided with respect to the methane inlet. The diameter of the methane inlet is assumed to be '1 d'. The extended lengths of the inlet ports are chosen to achieve a developed flow at the combustion chamber inlets, Figure 61(d). The combustion chamber length is determined to be '300 d'. Even though it is expected that the actual flame length is significantly smaller than the combustion chamber, the extended chamber length will provide enough span for the carbon dioxide mixing and the temperature reduction. The dimensions for the carbon dioxide inlets are determined in such a way that the CO₂ mass flowrate can be divided to 50-50 % into two inlet ports for the same CO₂ velocity.

The mesh that has been used for this study is shown in Figure 62. The mesh possesses an average orthogonal quality of 0.989. Only the 1/8 of the combustor is being meshed. The symmetry boundary condition is utilized for conducting the simulation.

Table 22 Inlet flowrates

Primary CO ₂ (%)	Secondary CO ₂ (%)	\dot{m}_{CH_4} kg/s	\dot{m}_{O_2} kg/s	$\dot{m}_{CO_2(total)}$ kg/s	Primary CO ₂ kg/s	Secondary CO ₂ kg/s
50%	50%	0.0025	0.0100	0.1586	0.0793	0.0793

The combustion simulation is conducted at a 30 MPa (300 bar) pressure between oxygen and methane with carbon dioxide dilution. At the beginning a comparison has been made among the ideal gas, Peng Robinson EOS and Lee-Kesler Plocker EOS. Since the Peng-Robinson EOS utilizes cubic root assumption for calculating density of the fluids, it is presumable that there will be a distinction between Lee-Kesler Plocker and Peng-Robinson density values. As mentioned earlier, the study is conducted by analyzing one injector operating at a 125-kW firing input using a symmetry boundary condition. Due to high carbon dioxide recirculation, the combustion will occur in a carbon dioxide filled environment. For this particular case carbon dioxide inlet flow is divided into half (50%-50%) and delivered through two inlet ports. The detailed mass flowrates are stated in Table 22. The inlet temperature for methane, oxygen and carbon dioxide are 400 K, 300 K and 935 K, respectively. The combustion simulation is performed in the 3D domain. However, 2D cross-sectional views at the injection and combustion zone are shown in this paper for the comparison purposes. Figure 63, shows that density of the mixture fluids at the inlet of the combustor. Density impacts on the local velocity field can be seen. This is because for a constant mass flowrate and area, the velocity is directly proportional to the density. These will eventually dominate the local combustion behavior. However, from the contours, it is hard to distinguish the differences in densities among the models. Therefore, the compressibility factor is presented. Figure 64 shows the compressibility factor at the inlet of the combustor. For Ideal gas the compressibility factor is constant at 1. It can be seen that the combustion chamber is primarily filled with carbon dioxide near the injector and then throughout the combustor. The PR EOS and LKP EOS demonstrate a compressibility factor of 1.07 and 1.09, respectively. In the model a comparison between the PR EOS and LKP show that there are significance differences in the flow behaviors near and away from the injector. Other combustion properties help to provide more insight, such as temperature.

Figure 65 shows the temperature distribution inside the combustor for the ideal gas and the real gas models. Since combustion kinetics at a 30MPa (300 bar) supercritical stage are still unknown, a one-step combustion reaction is employed for the combustion modeling. For this

study, the radiation model is not employed. The radiation model is not implemented for a few reasons, 1) it is not clear that the radiation model in Fluent is equipped to predict the behavior of oxy-combustion radiation products at this elevated pressure condition and 2) Since the radiation model is not used, the temperatures presented represent a comparison between the different models and may not be entirely accurate when compared to experimental data. For example, since the radiation model is not employed and since a one-step combustion chemistry model is used the peak flame temperatures are very high. However, results presented in this paper are thought to be immediately relevant to industry and other researchers since no such data is available for a similar system. Regardless, it is observed that the maximum chamber temperature during the Peng Robinson equation of state simulation exhibits almost 700K lower temperature than Lee-Kesler Plocker model. Furthermore, the exhaust temperature is relatively lower when using the Peng Robinson EOS compared to Lee Kesler EOS. The maximum exhaust temperature while using the Peng Robinson EOS is 1600 K, whereas the Lee Kesler EOS evaluated maximum temperature almost 1900 K. This is due the fact that the density calculation and mixing evaluation process is different between these two models. Oh et al. [21] recommended using the Lee Kesler equation and it is known that the constants used in the model derive from experiments whereas the Peng Robinson EOS relies on a cubic root equation. In Ref. [21] The authors use similar real gas models to analyze the supercritical carbon dioxide application in a very high temperature nuclear reactor. This paper agrees with the findings of Oh et al. [21]; however more detailed experimental data and radiative models should be developed to further corroborate the findings from these papers.

The primary purpose of this study is to compare flow characteristics, mixing profile, temperature distribution and compressibility factors using the Peng Robinson, Ideal Gas, and Lee-Kesler Plocker equation of states. The study shows that the maximum chamber temperature using the Peng Robinson equation of state is almost 700 K lower than when using the Lee-Kesler Plocker model. This is due to the assumptions and methodology made in each model for the thermodynamic properties of the fluid. It is believed that the Lee-Kesleer Plocker EOS represents a more accurate temperature since the equations used are based on experimental data and prior

literature suggests use of this model [21]. Thus, to avoid the over prediction of the temperature accurate equation of state must be used. However, Lee-Kesler Plocker requires significantly longer computational time than Peng Robinson EOS. The Lee Kesler EOS must be optimize to reduce the computational time. Peng Robinson may provide better estimation of supercritical combustion than ideal gas assumption. Peng Robinson can be used for analysis purposes.

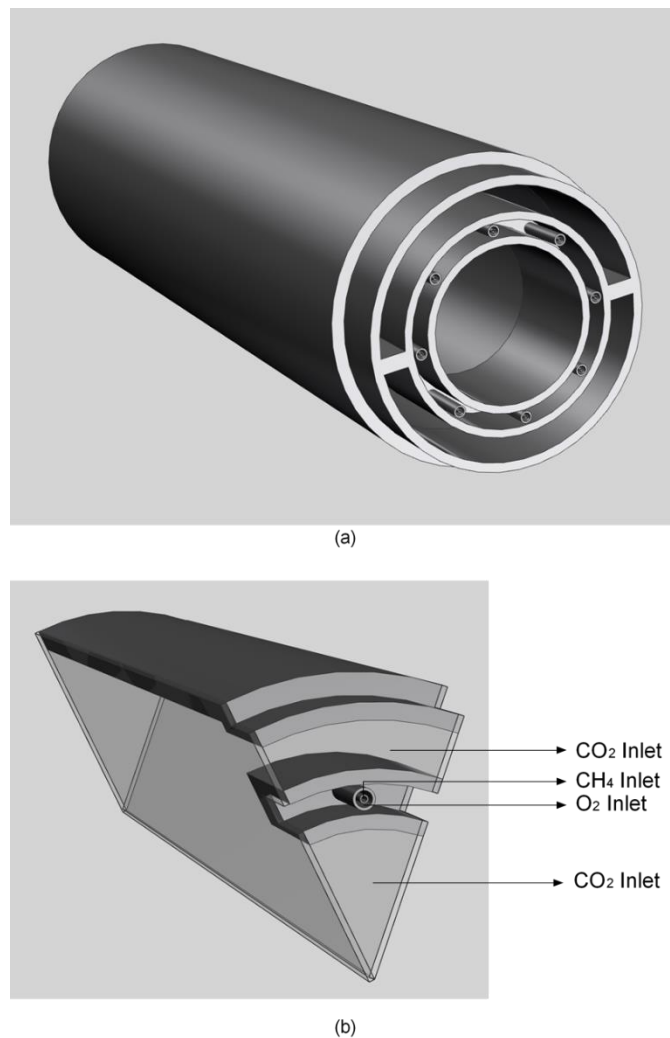


Figure 60 (a) Proposed oxy-methane supercritical combustor, (b) One-eighth of the proposed combustor

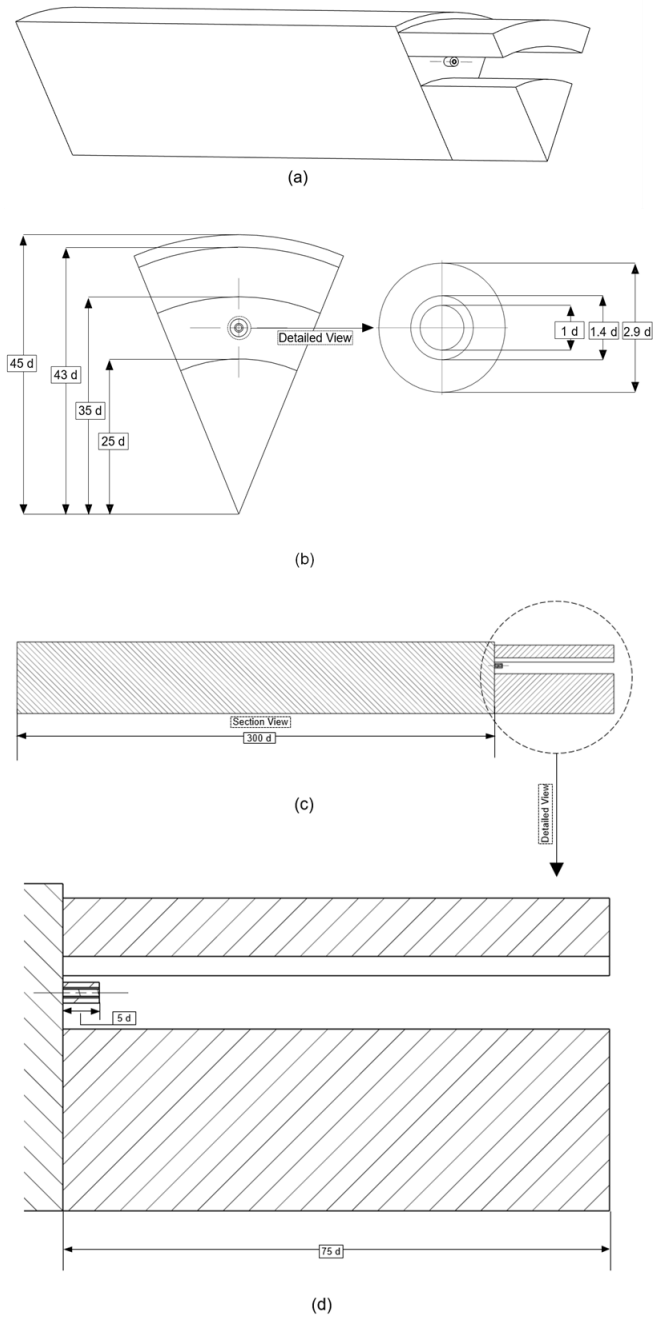


Figure 61 (a) CFD simulation fluid domain, (b) Inlet of the combustion chamber, (c) Cross-section view of the fluid domain, (d) Detailed view of the inlet cross-section

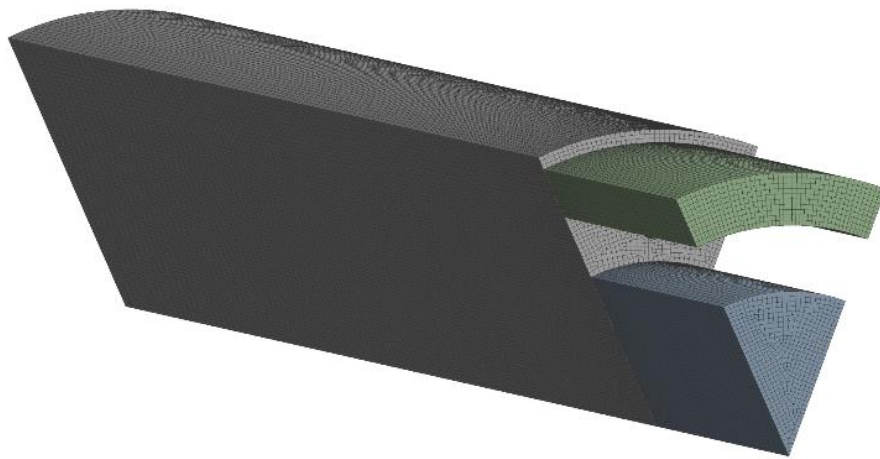


Figure 62 Mesh (Fluid domain)

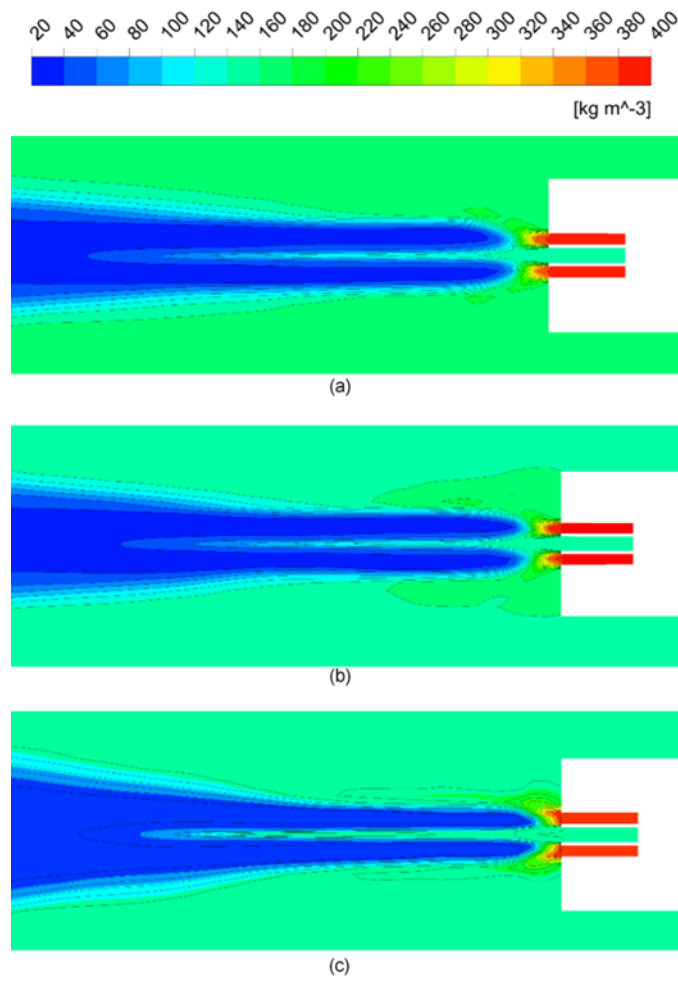


Figure 63 Density distribution at the inlet of the combustion chamber (a) Ideal gas, (b) Peng Robinson, (c) Lee Kesler

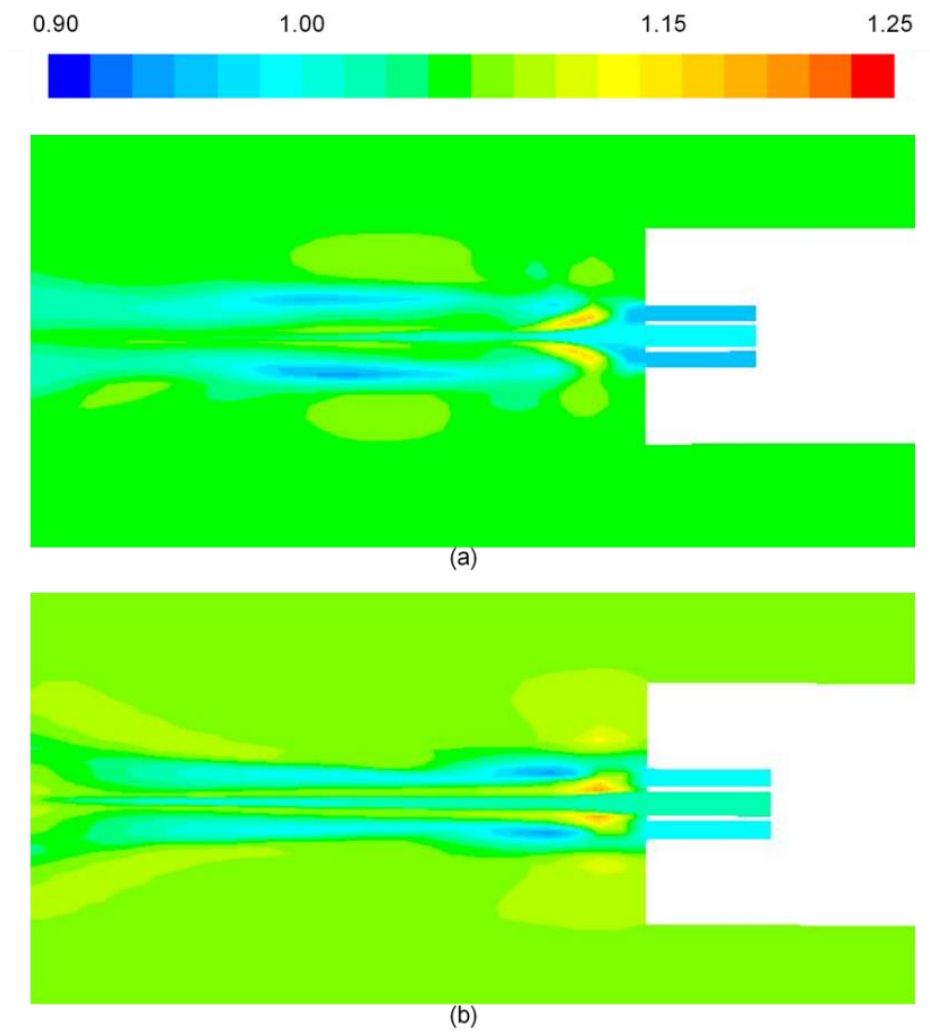


Figure 64 Compressibility factor at the inlet of the combustor (a) Peng Robinson EOS (b) Lee Kesler EOS

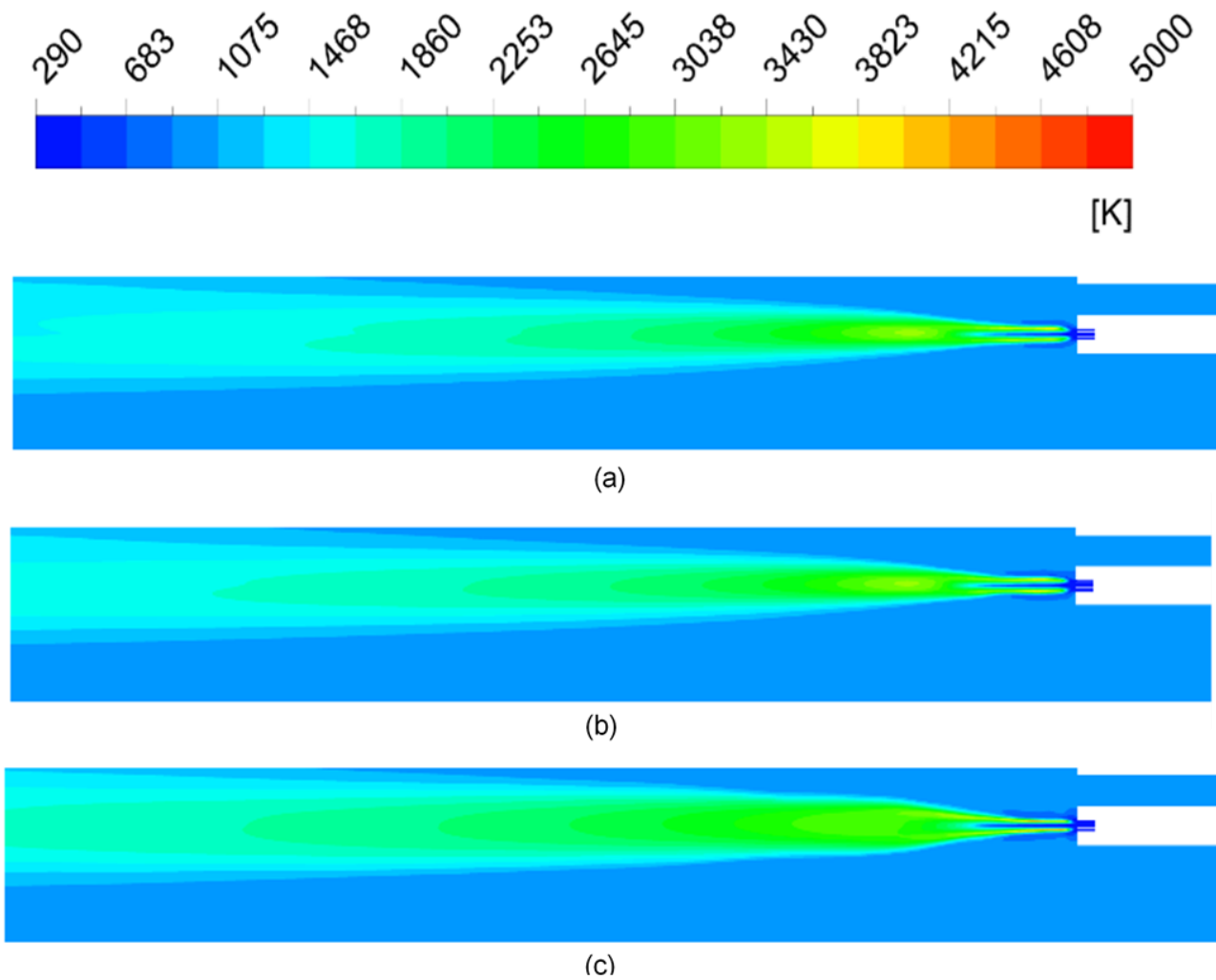


Figure 65 Temperature distribution inside the combustor (a) Ideal gas, (b) Peng Robinson, and (c) Lee Kesler

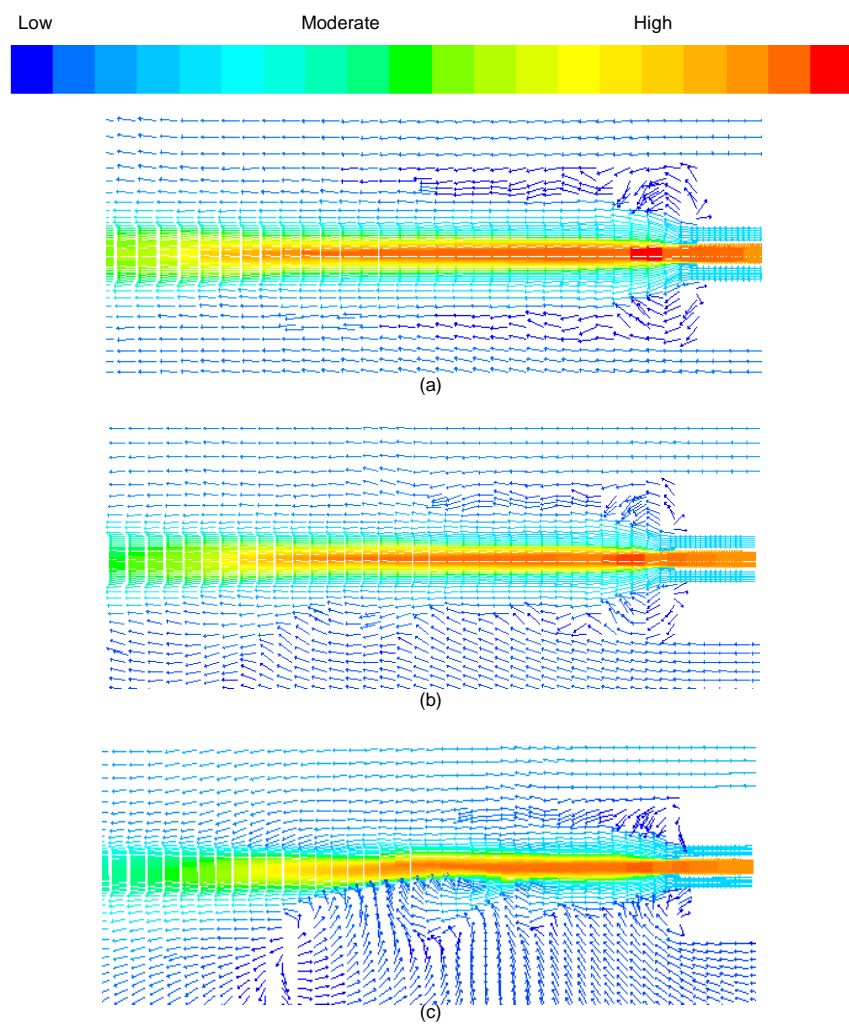


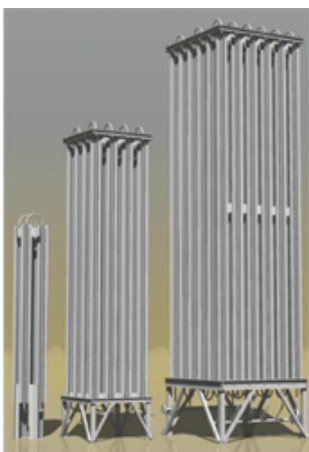
Figure 66 Flow path at the inlet of the combustor (a) 50%-50% split, (b) 30%-70% split, and (c) 10%-90% split

❖ Carbon Dioxide Vaporizer

For steady state operation a carbon dioxide vaporizer must be installed. This section provide a specification of such vaporizer.

<http://www.rmiororder.com/product/SE/FG01631/Model-HBSG50HF-Ambient-Vap->

[Supergap-Single-Circuit-5300-SCFH-8hr-600-PSIG](#)



Model HBSG50HF Ambient Vap Supergap, Single Circuit 5300 SCFH (8hr) 600 PSIG

Part #	FG01631
Weight	275.00000 lbs
Length	158.00
Width	38.00
Height	28.00



Print Page

Product Information

FG01631 - Model HBSG50HF Ambient Vap Supergap, Single Circuit 5300 SCFH (8hr) 600 PSIG

Vaporizers

ThermafinTM SupergapTM Ambient Vaporizer

Zero Energy, Zero Maintenance

SupergapTM Ambient Vaporizers have become the industry standard for ambient air vaporization. SupergapTM Vaporizers use natural convection of air to vaporize liquefied gases. Finned aluminum tubes absorb heat from the air and transfer that heat to the product gas. The huge 4 inch gap between fin tips provides room for ice growth and allows for more than 500 hours of continuous operation without defrost, making Supergaps ideal for severe climates and long duration operation. Extended operation requires a system of switching vaporizers designed by Thermax. In addition to our standard aluminum construction, units are available with stainless steel and other alloy liners for high pressure and corrosive applications.

STANDARD FEATURES

- 12 inch fin tube center to center spacing
- 4 inch gap between fins
- Standard models rated up to 200 MSCFH
- Aluminum corrosion resistant construction
- High strength welded base frame
- Withstands 100 mph winds and Zone 4 seismic forces
- 600 psig standard design pressure on all aluminum units
- Severe thermal cycling design
- Enhanced internal 16 fin heat transfer area, highest in industry
- No-crate shipping design for larger models
- Perimeter frame and legs for unrestricted airflow
- ASME B31.3, CRN (all provinces), & PED module D compliant

OPTIONS

- Stainless steel, monel and other alloy liners
- Design pressures exceeding 15,000 PSIG
- Gale Force™ design for 150 MPH wind loads per ASCE 7-05
- Flanged, tongue and groove, buttweld end connections
- Tank, wall, or truck mounting
- Continuous operation with switching system
- Electropolished 316LSS internals for ultra-pure applications

❖ Gas Tank Regulator CGA Selection Chart



Reference Tables

CGA Selection Charts

Pure Gases CGA Selection Chart for Fittings

CGA Fittings Required	Pure Gases
510/300	Acetylene
590/348/347/702	Air
240/660/705	Ammonia
580/680/677	Argon
350	Arsine*
320	Carbon dioxide
350	Carbon monoxide
660	Chlorine
510	Cyclopropane
350	Deuterium
350	Ethane
350	Ethylene
510	Ethylene oxide
580/680/677	Helium
350/695/703	Hydrogen
330	Hydrogen chloride
330	Hydrogen sulfide
580	Krypton, kr-85
350/695/703	Methane
510	Methyl chloride
580/680/677	Neon
580/680/677	Nitrogen
326	Nitrous oxide
540/577/701	Oxygen*
350	Phosphine
510	Propane
350	Silane*
668/660	Sulfur dioxide
590	Sulfur hexafluoride
580/680/677	Xenon

Mixed Gases CGA Selection Chart for Fittings

CGA Fittings Required	Mixed Gases	
	Minor Component	Major Component
240/660/705	Ammonia	Nitrogen
350	Butane	Nitrogen
296	Carbon Dioxide	Oxygen
580	Carbon Dioxide	Helium or nitrogen
580	Carbon Dioxide and/or Nitrogen	Helium
330	Chlorine	Nitrogen
350	Diborane	Argon, helium, Hydrogen, nitrogen
580	Freon-12	Nitrogen
296	Helium	Oxygen
350	Hexane	Nitrogen
350	Isobutane	Nitrogen
350	Krypton-85	Carbon monoxide, Hydrogen or methane
330	Krypton-85	Chlorine
540	Krypton-85	Oxygen
580	Moisture	Argon, helium or Nitrogen
660	Nitric Oxide	Nitrogen
660	Nitrogen Dioxide	Air or nitrogen
590	Nitrous Oxide	Nitrogen
590	Oxygen	Nitrogen or helium
350	Propane*	Nitrogen or helium
660	Sulfur Dioxide	Air or nitrogen
590	Sulfur Hexafluoride	Argon, helium or Nitrogen
350	Sulfur Hexafluoride	Hydrogen
350	Tritium	Argon, carbon dioxide, hydrogen, methane, neon, nitrogen, krypton, or xenon

It is recommended that the user thoroughly familiarize himself with the specific properties of these gases.

The Compressed Gas Association (CGA) has selected and standardized the valve outlet to be used on each gas cylinder. These standards, contained in the document "CGA STANDARD V-1, Compressed Gas Cylinder Valve Outlet Connections", have been adopted to prevent the inadvertent mixing of gases which could be reactive and to avoid other possible misuse hazards.

The above chart may be used for guide purposes only. Consult your gas supplier to determine the actual CGA connection required when ordering a regulator.

*Exceptions: Flammables in Air or Oxidizers

*Propane in air, methane in air, carbon monoxide in air: CGA 590

Since the combined characteristics of a mixture of gases often differ from the properties of the separate components, different CGA connections are often required. The chart above can be used as a reference for the CGA connections.

Mixtures which use the same CGA connection as if the minor component were in its pure gas form have not been included for the sake of brevity. The proper fitting for these mixtures can be determined by looking up the minor component on the chart for pure gases.

❖ Heavy Duty Gas Tank Regulator Specifications

SR 600

Heavy Duty

Single stage regulator designed for pressure testing and ideal where 350 or 550 PSIG (maximum) delivery pressures are needed, such as dead-end testing

DESIGN/CONSTRUCTION

- Forged brass body & housing cap
- 2.5" (63.5 mm) gauges – brass (6000 lb. high pressure, 600 lb. and 1000 lb. low pressure)
- Cartridge type seat assembly with PCTFE seat
- Diaphragm – stainless steel
- External self-reseating relief valve
- CGA 540, 580, 346 have a maximum inlet pressure of 3000 PSIG

DIMENSIONS

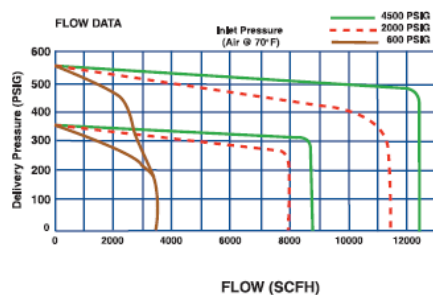
7.5" W x 6" H x 5" D
(190.5 mm x 152.4 mm x 127.0 mm)

WEIGHT

5 lb. 7 oz. (2.47 kg)

PERFORMANCE

Maximum inlet – 5500 PSIG
Outlet pressure ranges – 350 and 550 PSIG
Inlet port – 5/8"-20 UNF(M)
Outlet fitting – 1/4" Swagelok-brass
Temperature operating range – 0-140°F



Gas Service	Part No.	Model No.	Delivery Range (PSIG)
Inert Gas	0781-1601	SR 600-350-580	5-350
High Pressure Inert Gas	0781-1604	SR 600-350-680	5-350
High Pressure Air	0781-1605	SR 600-350-347	5-350
Oxygen	0781-1610	SR 600-550-540	5-550
Inert Gas	0781-1611	SR 600-550-580	5-550

Vita

Arifur Chowdhury graduated Summa Cum Laude with his Bachelor's in Mechanical Engineering from the University of Texas El Paso (UTEP) in 2014. He graduated his master's and started his PhD at UTEP in 2015. His research work focuses on the development of combustors intended for high pressure/ supercritical phase oxy-combustion. During his time as a graduate research assistant, he has led two Department of Energy projects and one industry sponsored project. As a part of his professional development, he did a summer internship at Air Liquide R&D and attended combustion summer school at Princeton University. He has authored two journal publications and numerous conference papers. Due to his contribution as a combustion researcher he received the ASME Young Engineer Turbo Expo Participation Award in 2017.

Permanent address: Sohel Monzil, Kasaripara, Satkhira
Satkhira Sadar, Bangladesh

This thesis/dissertation was typed by A S M Arifur Rahim Chowdhury